Impact of the plasma geometry on the divertor power exhaust in a magnetic fusion reactor

Alberto Gallo

Aix*Marseille université

cea irfm

Doctoral thesis

Aix-Marseille University

Doctoral School: *Physique et Sciences de la Matière*

Speciality : **Énergie, Rayonnement, Plasma**

Impact of the plasma geometry on the divertor power exhaust in a magnetic fusion reactor

---

Presented by:

Alberto Gallo

Board of examiners for the public PhD defense on the 9th of January 2018 :

Ambrogio Fasoli	Referee	Laboratory director, SPC, EPFL
Elisabeth Wolfrum	Referee	Research director, IPP, MPG
Alain Becoulet	Examiner	Laboratory director, IRFM, CEA
Pascale Hennequin	Examiner	Research director, LPP, CNRS
Yannick Marandet	Examiner	Research fellow, PIIM, CNRS
Matteo Passoni	Examiner	Research director, CeSNEF, PoliMi
Nicolas Fedorczak	PhD supervisor	Research fellow, IRFM, CEA
Philippe Ghendrih	PhD director	Research director, IRFM, CEA

Laboratory :

Institut de **R**echerche sur la **F**usion par confinement **M**agnétique

CEA – Cadarache, 13108 Saint-Paul-lez-Durance, France

October 2014 – January 2018

Thèse de doctorat

Université d'Aix-Marseille

École doctorale: *Physique et Sciences de la Matière*

Spécialité : **Énergie, Rayonnement, Plasma**

Impact de la géométrie du plasma sur l'extraction de puissance au divertor d'un réacteur à fusion magnétique

---

Presentée par:

Alberto Gallo

Thèse soutenue publiquement le 9 Janvier 2018 devant le jury composé de :

Ambrogio Fasoli	Rapporteur	Directeur de laboratoire, SPC, EPFL
Elisabeth Wolfrum	Rapporteur	Directeur de recherche, IPP, MPG
Alain Becoulet	Examinateur	Directeur de laboratoire, IRFM, CEA
Pascale Hennequin	Examinateur	Directeur de recherche, LPP, CNRS
Yannick Marandet	Examinateur	Chargé de recherche, PIIM, CNRS
Matteo Passoni	Examinateur	Directeur de recherche, CeSNEF, PoliMi
Nicolas Fedorczak	Encadrant de thèse	Chargé de recherche, IRFM, CEA
Philippe Ghendrih	Directeur de thèse	Directeur de recherche, IRFM, CEA

Laboratoire :

Institut de **R**echerche sur la **F**usion par confinement **M**agnétique

CEA – Cadarache, 13108 Saint-Paul-lez-Durance, France

Octobre 2014 – Janvier 2018

Dedicated to Julien Denis

Contents

Acknowledgements

Despite these are without a doubt the most important pages of the whole thesis, here I am the very last day, writing them in a rush and sincerely hoping not to forget anyone. The risk is high since, with time, the list of people who helped you becoming who you are can only get longer and this booklet, believe it or not, is just the last tile of a vast and diverse mosaic that took nearly twenty five years to complete: my career as a student.

In science, as in all the beautiful things in life, there is no "I". This is the reason why most of the sentences in this manuscript start with a "We": not for some form of *superbia*, but rather for the awareness that I wouldn't have been able to complete a single page alone.

I want and have to commence this list by thanking Nicolas Fedorczak, my supervisor. He deserves more than anyone else to be considered as a co-author of this manuscript: he shares with me the goods and the bads of this piece of work and I will never be able to repay him enough for his inextinguishable kindness and patience, for the enormous amount of hours he dedicated to me during these three years, for his being so contagiously passionate about science and yet at the same time so genuinely curious about everything else. What an adventure this was for both of us, Nico: me dealing for the first time with tokamaks and plasma physics, you supervising your first and not so easy PhD student. We might have had to catch up a bit with respect to other more experienced teams but I don't think they had as much fun as we had while doing this: *merci beaucoup, vraiment!*

My very second thanks goes sincerely to Philippe Ghendrih, who directed this PhD thesis. He decided to bet on me and take me on-board despite the fact that I was approaching magnetic fusion on a pretty diagonal trajectory and with basically no background, on the sole basis of my naive and storming motivation. He believed in me more than I did believe in myself and it's probably still the case now. He's always been rigorous with me but never rigid, always severe but never authoritarian, always demanding but never insensitive. Thank you for reminding me that *l'audace* is what makes a journey worth it.

I would like to continue by thanking the whole *Groupe Divertor et Interaction Plasma-Paroi* and in particular the group leader Guido Ciraolo, Pascale Monier-Garbet, Stephane Vartanian, Bernard Pegourie, Patrick Tamain, Hugo Bufferand, Giorgio Giorgiani, Jamie Gunn, Jean-Yves Pascal, Olivier Meyer and Pascal Devynck for the always friendly and almost familiar atmosphere in our corridor. I thank the two attentive service leaders Philippe Magaud and Frédéric Imbeaux as well as Laurence Azcona, Nathalie Bihan, Valerie Icard and Nathalie Borio for making the bureaucratic hell a walk in the park for me. With all of you I also thank the entire Institut de Recherche sur la Fusion par confinement Magnétique, the CEA-Cadarache and the École Doctorale 352 of the Aix-Marseille University for giving me the opportunity to undertake this PhD thesis.

Throughout these three years I had the pleasure to spend four very exciting and fruitful months at the Swiss Plasma Center of the EPFL. A special thank you to all the people I met working on TCV for the intense time in and out of the lab: Christian Theiler, Roberto Maurizio, Holger Reimerdes, Stefano Coda, Benoit Labit, Sarah Elmore, Michael Faitsch, Matteo Fontana, Umar Sheikh, Paola Paruta, Hamish Patten, Kevin Verhaegh, Cedric Tsui, Julien Dominski, Antoine Merle, Michael Komm, Claudio Marini, Fabio Avino and the whole TCV and MST1 teams for welcoming me and helping me during the experiments as well as the EUROfusion task force leaders for supporting my visits.

I'm also profoundly grateful to Elisabeth Wolfrum and Ambrogio Fasoli for accepting the duty of reading and reviewing this manuscript, as well as to the each and every other member of the examining jury: Alain Becoulet, Pascale Hennequin, Yannick Marandet and Matteo Passoni. Your interest in this work and your commitment in coming, in some cases from far away, to join the discussion makes me feel proud and honoured at the same time, while it indubitably enriches the scientific value of this thesis.

I say *grazie* to all those people who went through these three years with me shoulder to shoulder, supporting and tolerating me during many long days in Cadarache and some even longer nights in Aix: Julien Denis, Davide Galassi, Matteo Valentinuzzi, Claudia Norscini, Emelie Nilsson, Camille Baudoin, Nicolas Nace, Karol Jesko, Adrien Autrique, Axel Jardin, Serafina Baschetti, Giacomo Dose, Federico Nespoli, Jorge Morales, Farah Hariri, Peter Donnel, Etienne Hodille, Olivier Fevrier, Francois Orain, Cristian Sommariva, Elisabetta Caschera, Gerardo Giruzzi, Gloria Falchetto, Flavio De Magistris, Anastasia Dvornova, Didier Vezinet and Sara Breton.

Many are also those who, despite living outside of the scientific world, contributed to this work by keeping me in a great mood during these (first?) three French years and filling my life with beauty and energy even in the most difficult moments: thank you to Enrica Epifano, Valentin Lacroix and Vivia Liang, Lucas Evrard, Alice Michel, Marine Fioravasti, Andréa Ducruet and all the other *colocs* for two unforgettable years spent in a truly unforgettable house in the *campagne aixoise*.

Thank you from the bottom of my heart to a truly remarkable group of friends who adopted me and made me discover this blessed piece of Europe that we have the chance to live in: Benjamin, Sandra, Florian, Tess, Romain, Franzie, Jean-Yves, Aladin, Zsofia, Antoine, Clemence, Bastien, Yann, Laurie, Emilien, Pauline, Bebert, Fanny, Leandra, Thomas, Julie, Karina and Laurine.

Thank you to Dr. Philippe Lemaire for saving my left leg after that motorcycle accident and to my physiotherapist Jay Farber for getting me first walking, then running again.

Grazie mille to my best friends, cheering for me from wherever they are in the world at the moment: Michele Herbstritt, Maurizio Ghione, Gabriele Vargiu, Matteo Zulian, Tudor Porosnicu, Laura Simonini, Nicole Morasco, Margherita Isella, Elia Contitni, Lorenzo Granato, Giuseppe Gregu, Giuseppe Giudice, Viola Melis, Romina Elias, Anna Bernasconi, Carlotta Carboni, Francesco Basciu, Mattia Porcu, Giulio Giorgio, Giulia Ronzio, Angelo Bassi, Nicoló Minetti and Anna Sguazzini Viscontini. Our reunions and your visits filled my heart with joy, your warm welcomes made each trip back Home worth every minute of the five-hours-drive, your messages and phone calls kept me going whenever I was homesick. If I could achieve anything it is because you inspired me.

Finally I thank my Family, for always standing by me, even if I couldn't be with them.

Abstract

A deep understanding of plasma transport at the edge of a magnetically confined fusion device is mandatory for a sustainable and controlled handling of the power exhaust at the first wall of the machine. In the next-generation fusion device ITER, technological limits due to materials selection and engineering design constrain the peak heat flux on the divertor plasma facing components to 10 $\mathrm{MW\,m^{-2}}$ during steady state operations. For a given exhaust power, set by performance requirements, the peak heat flux is determined by the extent of the plasma footprint on the wall that is related to the width of heat flux profiles at the divertor targets. Experimental observations collected on a number of tokamaks over the last three decades taught us that heat flux profiles at the divertor targets of X-point configurations can be parametrized by using two length scales for the transport of heat in the scrape-off layer (SOL), separately characterizing the main SOL (λ_q) and the divertor SOL (S_q).

In this work, we challenge the current interpretation of these two length scales as well as their dependence on plasma parameters by studying the impact of divertor geometry modifications on the heat exhaust with dedicated experimental investigations in the *Tokamak à Configuration Variable* (TCV). In particular, a significant broadening of the heat flux profiles at the outer divertor target is diagnosed with both infrared thermography and Langmuir probes while increasing the length of the outer divertor leg L_{div} in lower single null (LSN), Ohmic, low density, L-mode, attached discharges: λ_q increases by a factor of $\simeq 2$ over the explored range, while no strong variation in S_q is observed.

Modelling efforts showed that diffusive simulations well reproduce the experimental heat flux profiles for short-legged plasmas, regardless the assumption of constant or radius-dependent perpendicular transport coefficients. This is the case for both a simple Monte Carlo particle tracer (MONALISA) and a more complex fluid code simulating ions, electrons and neutrals (SolEdge2D-EIRENE). Adding a poloidal dependence (*ballooning*) of perpendicular transport coefficients to account for localized enhanced transport at the outer midplane, changes the symmetry of target profiles which exhibit a lower S_q/λ_q ratio, close to what is observed experimentally. However, diffusive simulations yield a

constant λ_q and an increasing S_q with a longer divertor leg. Conversely, the increase in λ_q with L_{div} measured in the experiment is in qualitative agreement with the results of a first principle turbulent model (TOKAM3X) highlighting the importance of turbulent transport not only in the main SOL but also in the divertor SOL as a possible cause of stronger broadening of the target heat flux profiles in the case of a longer divertor leg. These results question the current interpretation of λ_q as a purely main SOL heat transport length scale with $B_{\mathrm{P}}^{\mathrm{omp}}$ as the main, or even only, control parameter. In fact, long divertor leg magnetic configurations as the TCV ones presented in this work highlighted the importance of asymmetric divertor transport that cannot be captured under the simplified assumption of symmetric diffusion that stands behind S_q. We therefore conclude that main SOL and divertor SOL transport cannot be arbitrarily disentangled and we underline the importance of the divertor magnetic geometry in enhancing asymmetric turbulent transport with the potential benefit of an unexpected power spreading.

Résumé en langue française

Une compréhension profonde du transport du plasma au bord d'un réacteur à fusion par confinement magnétique est obligatoire pour une gestion durable et controllée de l'extraction de puissance au niveau de la première paroi de la machine. Dans les dispositifs de fusion de nouvelle génération comme ITER, des limites technologiques dues au choix des matériaux et à la conception technique contraignent le flux de chaleur maximal sur les composants face au plasma du divertor à 10 $\mathrm{MW\,m^{-2}}$ pendant les opérations à l'état stationnaire. Pour une puissance d'échappement donnée, fixée par les exigences de performance du réacteur, le flux de chaleur maximal est déterminé par l'amplitude de l'empreinte du plasma sur le mur qui est liée à la largeur des profils de flux de chaleur sur les plaques du divertor. Les observations expérimentales recueillies sur plusieurs tokamaks au cours des trois dernières décennies nous ont appris que les profils de flux de chaleur au niveau des plaques du divertor en configurations point X peuvent être paramétrés en utilisant deux échelles de longueur du transport de chaleur dans la couche limite (SOL, de l'anglais Scrape-Off Layer), caractérisant séparément la SOL entourant le plasma confiné (λ_q) et la SOL dans le divertor (S_q).
Dans ce travail, nous remettons en question l'interprétation actuelle de ces deux échelles de longueur ainsi que leur dépendance aux paramètres du plasma en étudiant l'impact de la modification de la géométrie du divertor sur l'échappement thermique grâce à des expériences dédiées dans le *Tokamak à Configuration Variable* (TCV). En particulier, un élargissement significatif des profils de flux de chaleur avec la longueur de la jambe du divertor externe L_{div} est diagnostiqué à la fois par la thermographie infrarouge et les sondes de Langmuir au niveau de la plaque du divertor externe pendant des décharges lower single null (LSN), en mode L, à faible densité et chauffage Ohmique : λ_q augmente d'un facteur 2 sur la gamme explorée, alors qu'aucune forte variation de S_q est observée. Des efforts de modélisation ont montré que les simulations diffusives reproduisent correctement les profils expérimentaux de flux de chaleur pour les plasmas à jambes courtes, quelle que soit l'hypothèse sur les coefficients de transport perpendiculaires, constants ou dépendants du petit rayon de la machine. Ainsi, on retrouve ce résultat à la fois dans

les simulations à l'aide d'un simple traceur de particules Monte Carlo (MONALISA) et d'un code fluide plus complexe traitant ions, électrons et neutres (SolEdge2D-EIRENE). L'implementation d'une dépendance poloïdale (*ballonement*) des coefficients de transport perpendiculaires, afin de tenir compte de l'augmentation du transport localisé au niveau du plan médian externe, modifie la symétrie des profils qui présentent un plus petit rapport S_q/λ_q, proche de celui observé expérimentalement. Cependant, les simulations diffusives donnent un λ_q constant et un S_q croissant avec la longeur de la jambe du divertor. Inversement, l'augmentation du λ_q expérimental avec L_{div} est en accord qualitatif avec les résultats d'un modèle turbulent auto-cohérent (TOKAM3X), soulignant l'importance du transport turbulent non seulement dans le SOL entourant le plasma confiné, mais aussi dans la SOL du divertor. La presence d'un transport turbulent non négligable dans le divertor est une cause possible d'un plus important élargissement des profils de flux de chaleur dans le cas d'une jambe de divertor plus longue.

Ces résultats remettent en question l'interprétation actuelle du λ_q comme principale échelle de longueur du transport de chaleur dans la SOL entourant le plasma confiné, avec $B_{\mathrm{P}}^{\mathrm{omp}}$ comme principal, voire unique, paramètre de contrôle. En effet, les configurations magnétiques avec une longe jambe du divertor, comme celle obtenues sur TCV et présentées dans ce travail, mettent en évidence l'importance du transport asymétrique dans le divertor. Cette asymétrie ne peut pas être capturé par hypothèse de diffusion symétrique qui se tient derrière la définition de S_q. Par conséquent, nous concluons que le transport dans la SOL entourant le plasma confiné et celui dans le divertor ne peuvent pas être arbitrairement découplés et nous soulignons l'importance de la géométrie magnétique du divertor dans l'augmentation du transport turbulent asymétrique avec comme avantage potentiel un inattendu étalement du dépôt de puissance.

Chapter 1

Power exhaust in diverted tokamaks

Contents

1.1 Motivation

In future fusion machines as much as 20% of the power that is produced through nuclear reactions will have to be exhausted onto the vessel wall. In ITER present material and design choices for plasma-facing components and the associated cooling system set a technological limit of 10 MW m^{-2} as maximum heat flux (power density) onto Tungsten divertor targets that can be tolerated during steady state operations. For a given exhaust power, which is constrained by the performance of the reactor, the peak heat flux depends on the portion of the wall surface that is wetted by the plasma. In a tokamak, a device with toroidal symmetry, the extent of this footprint depends on its location along the major radius as well as by its width in the poloidal plane, which we call the *heat flux width*. This quantity is understood to be the result of the competition between the very effective heat transport along open magnetic field lines and heat transport across flux surface in the scrape-off layer. Despite a remarkable effort on this subject across the whole tokamak community over the last few decades, that allowed us to identify turbulent transport and vertical drifts as major players in setting the heat flux width, at present we lack a self-consistent theoretical model for the prediction of this quantity in future devices. Experimental estimates of the heat flux width at the divertor targets of existing devices allowed the construction of empirical scaling laws based on engineering parameters as machine size, plasma current, input power, density, magnetic field, etc. These studies were carried out with the goal of understanding how to control the heat flux width, at least phenomenologically, and through which "knobs". The most established of these empirical scaling laws, based on a database including machines of different sizes and shapes, suggests that that the heat flux width can be governed mainly through the poloidal magnetic field, with no or weak dependence on the machine size, nor on the specific divertor geometry. Extrapolation to the reference 15MA scenario for ITER based on this scaling law returns a value for the heat flux width that is small enough to rise concerns about our capabilities of respecting the above-mentioned divertor material limits. A great interest has recently grown around the possibility of exploiting new and exotic divertor geometries to induce an unprecedented spreading of the heat flux at divertor targets by increasing the heat flux width. It is in such framework, and in view of future fusion machines like DEMO and its successors, that this PhD thesis aims to give an original and helpful contribution to the field: in particular, with the aim of testing up to which point the magnetic geometry of the plasma can be used to control the power exhaust in a tokamak, we propose to study the effect of an extraordinarily long, vertical, outer divertor leg on the heat flux width.

1.2 Nuclear fusion

Our relentlessly growing energetic needs, together with severe climate change issues, urge us to explore new, effective and environmentally sustainable strategies to produce power. Nuclear fusion is the energy source of our sun and the other stars, incessantly converting part of their masses in energy that is then shared with the surrounding universe, making life possible on earth. The energy produced or consumed in a generic nuclear reaction can be defined as follows:

$$E = \Delta M_{\text{tot}} c^2 \tag{1.1}$$

where $\Delta M_{\text{tot}} = M_{\text{R}} - M_{\text{P}}$ is the difference between the masses of reactants and products and c is the speed of light in vacuum. Since the ultimate goal is to provide electrical power supply, we focus on exothermic reactions in which, in order to obtain positive values of E, ΔM_{tot} has to be positive and therefore the energy release happens at the expense of mass. Not all the elements present in nature are suitable for fusion reactions: light nuclei with low average binding energy per nucleon are the best candidates. Among these, the most promising are hydrogen isotopes and the reaction of choice is:

$$^{2}_{1}\text{D} + ^{3}_{1}\text{T} \longrightarrow ^{4}_{2}\text{He} + 3.5\,\text{MeV} + ^{1}_{0}\text{n} + 14.1\,\text{MeV} \tag{1.2}$$

With an energy release of 17.6 MeV per reaction, 1 kg of fuel would produce 10^8 kWh. A fusion reaction consists in overcoming the Coulomb repulsion of the two nuclei due to their positive electric charge and therefore cross sections σ are negligible at room temperature. To induce a D + T reaction one has to bring the colliding nuclei to energies of around 10 keV (100 million °C) and reaction rates of $\langle \sigma v \rangle = 10^{-22} - 10^{-21}$ $\text{m}^3\,\text{s}^{-1}$, where $\sigma = 10^{-29} - 10^{-28}$ m^2. At such extreme temperatures the fuel is completely ionized, resulting in a globally neutral gas of positive ions and electrons called *thermonuclear plasma*. Confining the system with material walls is not compatible with the extreme temperatures, particle and heat fluxes reaching its boundary. Therefore, an alternative strategy has to be found, as discussed in section 1.2.1. The amount of energy produced in a fusion reaction (17.6 MeV) is big and non-trivial to harvest since it is released in the form of kinetic energy of the reaction products. Fast (14.1 MeV) neutrons quickly leave the reaction environment and can be intercepted with a Lithium blanket to convert their kinetic energy in heat through the reaction $^{6}_{3}\text{Li} + ^{1}_{0}\text{n} \longrightarrow ^{3}_{1}\text{T} + ^{4}_{2}\text{He} + 4.8\,\text{MeV}$. This reaction is also useful for breeding Tritium, which has extremely scarce availability in nature. On the other hand, Helium as well as other impurities have to be exhausted from the system not to dilute the fuel mixture. How to achieve an efficient particle and heat exhaust within the limits set by existing materials are the topic of section 1.4.

1.2.1 Magnetic confinement

In order to achieve fusion reactions with a positive energy balance, heating a D + T mixture up to 10 keV is not sufficient. Particles have to remain in the reaction environment long enough to interact without losing their energy before a reaction occurs. The required values of temperature T, electron density n_e and energy confinement time τ_E (the inverse of the rate at which a system loses energy to its environment) are related through the following inequality, also known as *triple product* [1]:

$$n_\mathrm{e} T \tau_E \geq \frac{12 k_\mathrm{B}}{E_\mathrm{ch}} \frac{T^2}{\langle \sigma v \rangle} \tag{1.3}$$

where $k_\mathrm{B} \simeq 1.38 \times 10^{-23}\ \mathrm{J\,K^{-1}}$ is the Boltzmann constant and E_ch is the energy of the charged reaction products. This criterion defines the requirements for a fusion reactor to reach *ignition*, a self-sustaining condition in which the heating of the plasma due to the reaction products keeps the temperature high enough to counterbalance energy losses without the need of an external power input. For the D + T reaction, this corresponds approximatively to $n_\mathrm{e} T \tau_E > 5 \times 10^{21}\ \mathrm{m^{-3}\,keV\,s}$, which is yet to be achieved in an existing device. Two main mechanisms for the confinement of a thermonuclear plasma exist: inertial confinement and magnetic confinement. In this work we consider exclusively the latter, which is based on a simple but powerful physical principle. Charged particles in a magnetic field travel along the magnetic field lines (parallel direction, $\parallel$) while gyrating in the plane transversal to them (perpendicular direction, $\perp$). For a particle of mass m and charge q, the radius of this cyclotron motion, also-called Larmor radius, has the following expression:

$$\rho_L = \frac{m v_\perp}{qB} \tag{1.4}$$

where B is the magnetic field strength and $v_\perp$ is the average particle velocity in the $\perp$ direction, which can be approximated with the thermal velocity $v_\perp \simeq v_\mathrm{th} = \sqrt{k_\mathrm{B} T / m}$. Assuming $T = 10^8$ K and $B = 3$ T, one finds $\rho_{\mathrm{L,e}} = 7.38 \times 10^{-5}$ m and $\rho_{\mathrm{L,D^+}} = 3.2 \times 10^{-3}$ m for electrons and $\mathrm{D^+}$ ions respectively. These values are several orders of magnitude smaller than the size foreseen for future fusion reactors (meters) suggesting that an homogeneous magnetic field can efficiently confine the plasma in the $\perp$ direction. But how to confine it also in the $\parallel$ one? One among the possible strategies consists in bending field lines so that they become closed trajectories. This is the idea behind the *tokamak*, described in section 1.2.2.

1.2.2 The tokamak

The most widespread typology of fusion device based on magnetic confinement is the tokamak, Russian acronym of "**to**roidal'naya **ka**mera s **ma**gnitnymi **k**atushkami" (toroidal chamber with magnetic coils). As suggested by its name, the tokamak consists in an ideally axysimmetric machine with toroidal geometry and is therefore conveniently described in terms of major radius R, minor radius a, toroidal angle ϕ and poloidal angle θ. The vacuum vessel is surrounded by poloidal coils generating a magnetic field in the toroidal direction B_T (figure 1.1, blue line), confining the plasma in the $\perp$ direction. However, when bending field lines in order to create periodicity and therefore confinement in the $\parallel$ direction, one introduces an inherent asymmetry in the strength of B_T which is stronger in the vicinity of the axis of revolution of the torus (high field side, HFS) than away from it (low field side, LFS), with a $1/R$ dependence. Since $\rho_\mathrm{L} \propto B^{-1}$, the further the particle is from the axis of the machine the bigger will be its gyration. This inhomogeneity leads to a vertical drift, which has opposite sign for particles with positive and negative charge with the consequent onset of a vertical electrostatic field and an associated $E \times B$ force that pushes the plasma radially outwards.

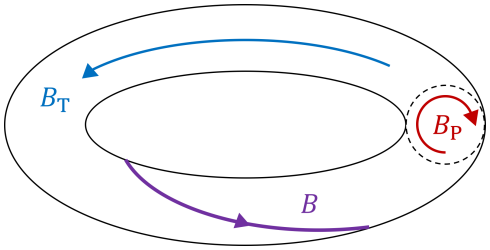

Figure 1.1: sketch of the axisymmetric geometry of a tokamak with the direction of toroidal (B_T, blue), poloidal (B_P, red) and total (B, purple) magnetic field lines.

Charges are re-mixed and the electrostatic field reduced by adding another magnetic field in the poloidal direction B_P (figure 1.1, red line) which is generated by running a current through the plasma, most commonly driven by the transformer action of a solenoid placed in the central column of the torus. This current is usually referred to as I_P (the reader should remember that "P" here stands for plasma and not for poloidal since it flows in the toroidal direction: even though we think it should rather be labelled I_T, or simply I, we stick to I_P for the sake of consistency with the literature). The resulting total magnetic field B (figure 1.1, purple line) has helical field lines that wrap nested surfaces of constant poloidal magnetic flux ψ. The helicity of B is described by the safety factor q (not to be confused with the heat flux, labelled with the same letter), defined as the number of toroidal turns that field lines have to accomplish in order to complete a poloidal turn. In the approximation of a cylindrical plasma, the safety factor can be

expressed as $q_{\mathrm{cyl}} = \frac{a}{R}\frac{B_{\mathrm{T}}}{B_{\mathrm{P}}}\sqrt{\frac{(k+1)^2}{2}}$, where k is the plasma elongation. A key role is played by the last closed flux surface (LCFS) that inevitably has at least one contact point with the vessel wall. In the vicinity of this (these) contact point(s) the so-called plasma-wall interaction takes place, as discussed in section 1.4.1. The LCFS, also called *separatrix*, divides the confined plasma region, the core, from the unconfined one, the scrape-off layer (SOL) where particles and heat flow along open magnetic field lines and reach material surfaces. The SOL is a region of particular interest and complexity since it constitutes the interface between the plasma and the device itself, and acts as the main channel for particle and heat exhaust, as developed throughout section 1.4. The more courious and motivated readers can find a broader and more detailed introduction on nuclear fusion and tokamaks in [2].

1.2.3 ITER

The biggest and most revolutionary tokamak ever designed is currently under construction in Cadarache, in the south of France. Its name is ITER, which is both an acronym (International Thermonuclear Experimental Reactor) and a reminiscence of the Latin word *iter* literally meaning path, journey. The biggest goal of ITER is, in fact, to reduce the gap between existing tokamaks (or any other fusion-oriented experiments) and future commercial nuclear fusion reactors and to show the feasibility of fusion-based energy production. The ITER project was funded in 2006 and is run by a consortium consisting of seven members: the European Union, India, Japan, China, Russia, South Korea and the United States. With the estimated start of the operations in 2025 and a cost of nearly 20 billion euros, ITER represents a titanic project and is among the biggest technological challenges that human kind has ever accepted. ITER is designed to produce approximately 500 MW of fusion power sustained for up to 1000 s by the fusion of 0.5 g of D + T mixture. By comparison the Joint European Torus (JET), nowadays the largest magnetic confinement fusion experiment, has reached a peak fusion power of 16 MW maintained for less than a second. Moreover ITER is designed to produce 10 times more heat than the amount needed to heat up its plasma. ITER is going to be a massive machine: the vacuum vessel is going to weight more than 5000 tons and will be more than 11 m high, with internal and external diameters of 6.5 m and 19.4 m respectively. The generation of magnetic fields up to 13.5 T is entrusted to superconducting niobium-tin coils able to carry tens of kA and tens of GJ of power. Concerning materials, ITER's first wall will be mainly made out of Beryllium and Tungsten.

1.3 Plasma transport

The whole tokamak concept is based on the fact that the confinement obtained through magnetic fields ensures a much faster and more efficient plasma transport in the $\parallel$ direction than in the $\perp$ one. Nevertheless, because of the extreme temperature, density and pressure gradients between the center of the plasma and its periphery, thermodynamic forces trigger strong radial heat and particle fluxes directed outwards, reducing confinement and increasing losses in the system. The understanding, experimental assessment and modelling of these gradients is one of the big challenges of magnetic fusion research. We recall here some historically established attempts to give a description of the transport phenomena in a tokamak plasma.

1.3.1 Classical transport

A particle in the plasma orbiting along a magnetic field line can interact with another through Coulombian collisions. In the case of collisions among identical particles the center of mass is not affected and therefore no transport occurs. If instead the colliding particles have different mass and/or velocity the interaction can determine a displacement of their guiding centres in the $\perp$ direction leading to a change of flux surface and therefore to the transport of mass and energy. Since the guiding centres of ions and electrons are scattered by these collisions in an aleatory fashion, their trajectories perform a random walk and can therefore be modelled in terms of *diffusion*. The resulting particle flux in the $\perp$ direction depends on the product of the diffusion coefficient $D_\perp^c$ with the density gradient, and is directed against the latter:

$$\Gamma_\perp = -D_\perp^{\mathrm{c}} \nabla_\perp n \tag{1.5}$$

In this collisional approach the diffusion coefficient can be expressed in terms of the collision frequency ν_{coll} and the gyration radius ρ_{L} which are the characteristic time and length scales of the process:

$$D_\perp^{\mathrm{c}} = \nu_{\mathrm{coll}} \rho_{\mathrm{L}}^2 \tag{1.6}$$

Considering typical values of ν_{coll} between 1 kHz in the plasma core and tens of kHz at the edge ($\nu_{\mathrm{coll}} \propto nT^{-3/2}$), for Deuterium ions $D_\perp^{\mathrm{c}}$ is in the order of $10^{-4} - 10^{-2}$ $\mathrm{m^2 s^{-1}}$. This description, called *classical*, was found to fall short when inferring the value of $D_\perp^{\mathrm{c}}$ from experimental measurements on existing tokamaks, where much bigger diffusion coefficients need to be invoked to reconcile density gradients with unexpectedly strong particle fluxes.

1.3.2 Neoclassical transport

Since, as anticipated in section 1.2.2, the magnetic field inside a tokamak is not homogeneous, additional forces due to toroidicity and finite aspect ratio R/a act on charged particles determining additional components of the velocity referred to as *drifts*. In particular, the above-mentioned $B_\mathrm{T} \propto 1/R$ dependence leads to a gradient of B in the plane $\perp$ to field lines: during a single gyration, charged particles will reach further from their guiding center when experiencing a lower B because of the $\rho_\mathrm{L} \propto 1/B$ dependence. Overall this leads to a vertical drift of the guiding center motion, the so-called grad$B$ drift:

$$v_{\mathrm{grad}B} = \frac{m v_\perp^2}{2} \frac{B \times \nabla B}{q B^3} \tag{1.7}$$

Moreover, when the guiding center of a particle moves along a field line which is curved in the $\parallel$ direction it undergoes an additional drift perpendicular to the curvature plane. Such drift, which is also vertical, is called curvature drift, often shortened in curv$B$ drift:

$$v_{\mathrm{curv}B} = m v_\parallel^2 \frac{B \times \nabla B}{q B^3} \tag{1.8}$$

Therefore the combined expression for the vertical magnetic drifts can be written as:

$$v_\mathrm{drifts} = v_{\mathrm{grad}B} + v_{\mathrm{curv}B} = \left(\frac{v_\perp^2}{2} + v_\parallel^2 \right) \frac{m B \times \nabla B}{q B^3} = \left(\frac{v_\perp^2}{2} + v_\parallel^2 \right) \frac{B \times \nabla B}{\omega_\mathrm{C} B^2} \tag{1.9}$$

where $\omega_\mathrm{C} = Bq/m$ is the cyclotron frequency. Both drifts depend on q and therefore have opposite direction for ions and electrons. This leads to charge separation with the consequent onset of an electric field E, as described in section 1.3.3. Moreover particles with a small $\parallel$ velocity are subject to magnetic mirroring effects that can trap them into the so-called banana orbits in the LFS region [2]. Combining these magnetic drifts with collisions, already present in the classical approach (section 1.3.1), leads to a plasma transport picture called *neoclassical*. In this framework, the typical length scale of collisions corresponds to the orbit shift $q_\mathrm{cyl}\rho_\mathrm{L}$ and therefore the diffusion coefficient can be written as

$$D_\perp^\mathrm{nc} = \nu_\mathrm{coll} \left(q_\mathrm{cyl} \rho_\mathrm{L} \right)^2 \tag{1.10}$$

This implies that, for a typical edge plasma value of $q_\mathrm{cyl} = 3$, neoclassical transport would predict $D_\perp^\mathrm{nc} = 9 D_\perp^\mathrm{c}$, which is basically one order of magnitude larger than what one would find applying classical theory. Neoclassical values of the order of $D_\perp^\mathrm{nc} \simeq 10^{-1}$ m^{2}s^{-1} are still too small to match radial fluxes measured in experiments.

1.3.3 Turbulent transport

Experimental measurements showed that transport coefficients can be orders of magnitude bigger than the ones predicted from classical and neoclassical transport theories [3]. For this reason radial transport in tokamaks was historically given the adjective of *anomalous*. Over the last three decades, big steps forward in both experiments and theory shade light on the *turbulent* nature of cross-field transport [4]. In fact, strong and rapid fluctuations of n, T, B and electrostatic potential U generate fluxes in the $\perp$ direction. Such potential is associated to the inherent presence of an electrostatic field E due to the charge separation caused by grad$B$ and curv$B$ drifts, discussed in section 1.3.2. The joint effect of E and B fields leads to the onset of a radial component of the velocity known as electrostatic drift or simply $E \times B$ drift:

$$v_{E\times B} = \frac{E \times B}{B^2} \tag{1.11}$$

which, unlike magnetic drifts, is independent of q and m and therefore causes a collective outward movement which has the same direction and magnitude for all the particles. At the edge of a tokamak plasma most of the outward flux can be attributed to the fluctuations $\tilde{n}$ and $\tilde{v}_{E\times B}$ [5] and therefore we refer to this type of transport as *electrostatic turbulence*, assuming that $\tilde{B}$ is negligible by comparison. In particular, fluctuations of the electrostatic potential $\tilde{U}$ trigger a radial convective turbulent flux of the form:

$$\Gamma_{\perp}^{\text{turb}} \propto \langle \tilde{n}\tilde{v}_{E\times B} \rangle_{t,\phi} \tag{1.12}$$

which is maximum when the two fluctuations are in phase, null when they're in quadrature. Although it represents a conceptual oversimplification of the problem, turbulent transport has often been modelled as diffusive by assuming anomalously higher transport coefficients compared to both classical and neoclassical estimates in order to match experimental observations, allowing at least a qualitative description of perpendicular fluxes, as performed in sections 4.4.1 to 4.4.3. Alternatively, one can attempt to derive an expression for a turbulent diffusion coefficient based on the characteristic quantities of the small-scale turbulent structures. These structures can be thought of as vortexes described by a wave vector k and a turnover time τ. The corresponding turbulent diffusion coefficient can therefore be expressed as

$$D_{\perp}^{\text{turb}} = k^{-2}\tau^{-1} \tag{1.13}$$

By rewriting the turnover time in terms of the fluctuating electrostatic drift velocity as

$$\tau = (k|\tilde{v}_{E\times B}|)^{-1} = \left(k\frac{|\tilde{E}|}{B}\right)^{-1} = \left(k^2\frac{|\tilde{U}|}{B}\right)^{-1} \tag{1.14}$$

one finds a simple expression for the turbulent diffusion coefficient in terms of the fluctuations of the electrostatic potential and the total magnetic field:

$$D_{\perp}^{\mathrm{turb}} = \frac{|\tilde{U}|}{B} \tag{1.15}$$

Since the electrostatic potential is related to the thermal energy of the vortex, it is natural to renormalise it in terms of temperature as $|\tilde{U}| = \alpha|T_{\mathrm{e}}|$, where α is a dimensionless constant. This leads to:

$$D_{\perp}^{\mathrm{turb}} = \alpha\frac{|T_{\mathrm{e}}|}{B} \tag{1.16}$$

Assuming $\alpha = 1$ in equation 1.16, one finds the so-called Bohm diffusion coefficient $D_{\perp}^{\mathrm{B}}$

$$D_{\perp}^{\mathrm{turb}} = \frac{|T_{\mathrm{e}}|}{B} \simeq \rho_{\mathrm{L}}^2\omega_{\mathrm{C}} \simeq \rho_{\mathrm{L}}c_{\mathrm{s}} = D_{\perp}^{\mathrm{B}} \tag{1.17}$$

which, for ρ_{L} of the order of fractions of mm and c_{s} of the order of tens of kms^{-1}, predicts $D_{\perp}^{\mathrm{turb}} \simeq 1 - 10\ \mathrm{m}^2\mathrm{s}^{-1}$. If one instead assumes $\alpha = \rho^* = \rho_{\mathrm{L}}/a$ the gyro-Bohm diffusion coefficient $D_{\perp}^{\mathrm{GB}}$ appears

$$D_{\perp}^{\mathrm{turb}} = \rho^*\frac{|T_{\mathrm{e}}|}{B} = \rho^* D_{\perp}^{\mathrm{B}} = D_{\perp}^{\mathrm{GB}} \tag{1.18}$$

which corresponds to $D_{\perp}^{\mathrm{B}}$ corrected by ρ^* and therefore multiplied by a factor of 10^{-3}.

1.4 Particle and heat exhaust

1.4.1 Plasma-wall interaction

One of the key issues of magnetic confinement experiments is the inevitable exchange of particles and heat between the plasma and the surrounding vacuum vessel, called plasma-wall interaction (PWI). In magnetic fusion devices, part of the power supplied to the confined plasma by the heating systems enters the SOL due to cross-field transport. Here unconfined plasma flows both along and transversely to open magnetic field lines until it reaches a material surface. In the SOL the separatrix acts mainly as a source of particles and heat, while the plasma facing components (PFCs) of the wall play the role of

sink for the plasma. On the one hand a small but non-negligible fraction of the incoming particle flux is implanted and trapped in the PFCs with important consequences on both fuelling and radiotoxicity due to Tritium: we call this PWI process *retention*. On the other hand fractions as high as 99% of the ions impinging on the PFCs are re-emitted as neutral atoms that are free to travel back towards the hot confined plasma where they get ionized: this PWI process is referred to as *recycling*. The PFCs of ITER, for example, will have to withstand a temperature of thousands of K and a particle flux of $\Gamma = 10^{24}\ \mathrm{m^{-2}\,s^{-1}}$. Under these extreme conditions another kind of PWI takes place: *sputtering*, which consists in impinging ions knocking off atoms from the PFCs. This interaction can be either purely ballistic (*physical* sputtering) or enhanced by the affinity between fuel and wall (*chemical* sputtering). Sputtered neutral impurities can readily enter the plasma where they will be ionized transforming part of the energy of the system in radiation as well as polluting the fuel mixture. All these phenomena have to be taken into account when it comes to the material selection for the PFCs. Traditionally Carbon was the material of choice because of its refractory nature and its low atomic number Z, meaning a limited number of electrons to be stripped off and therefore reduced energy loss through radiation. Where Carbon falls short is retention: its porosity allows it to store an intolerable amount of Tritium. Moreover its affinity with Hydrogen isotopes makes it prone to severe chemical sputtering. In recent machines, as well as in ITER, Tungsten was chosen because of its excellent thermomechanical properties, its low permeability and affinity with Hydrogen isotopes, although the high Z represents a potential strong source of core radiation. The geometrical features of the magnetic equilibrium play a crucial role in handling the PWI, as discussed in section 1.4.2.

1.4.2 Magnetic geometry

The magnetic geometry has fundamental consequences on plasma transport and PWI since it sets the shape and size of the SOL, the volume available for power dissipation, the flaring between flux surfaces, the number of contact points, the size of the footprint and the angle of incidence of plasma on the PFCs. For instance, if the separatrix has one point tangent to the vacuum vessel one has a *limited configuration* (figure 1.2, left). In a limited configuration, heat and particle fluxes are concentrated in the vicinity of the contact point on a single PFC called, therefore, *limiter*. Material sputtered from the limiter can easily enter in the core, since the two are in direct contact. Here neutral atoms and molecules are ionized and cool down the plasma by radiation. As developed in section 1.4.1, this is particularly harmful in the presence of high-Z materials. If, on the other hand, B_P presents a null point, also called X-point, one has a diverted configuration

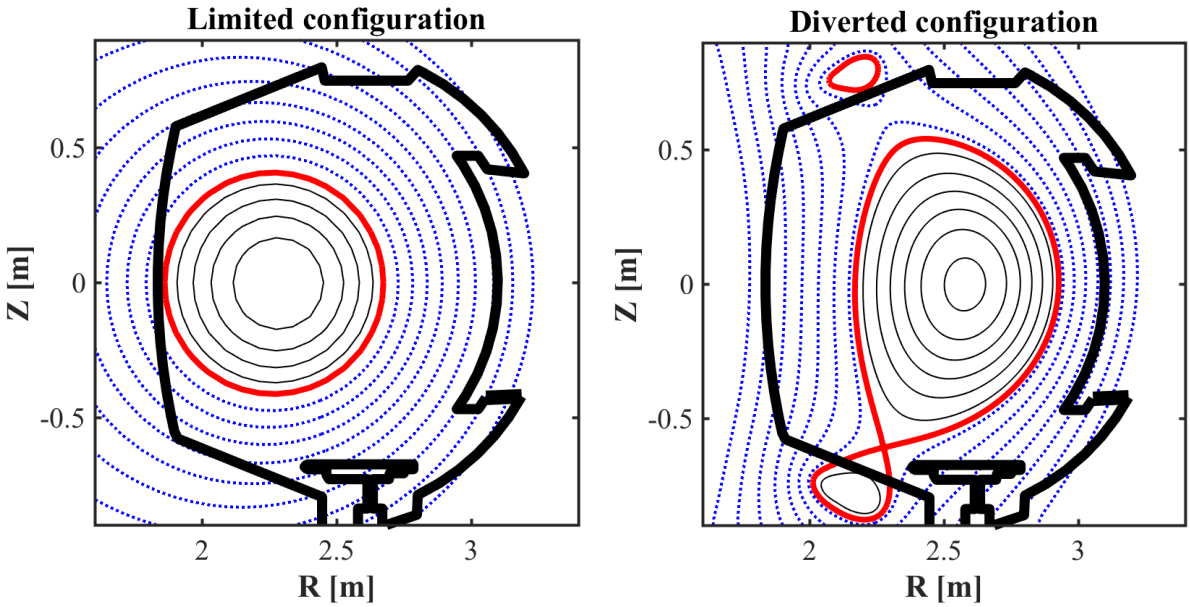

Figure 1.2: close (black lines) and open (blue dotted lines) magnetic flux surfaces, separatrix (red line), vessel wall (black thick line) for limited and diverted configurations. Viewgraphs obtained from MONALISA simulations in realistic WEST [6] geometry.

instead (figure 1.2, right). In diverted plasmas the presence of an X-point sets a distance between the core and the two strike points, where the separatrix intercepts dedicated PFCs called divertor targets: here most of the PWI occurs. Neutrals released from material surfaces can therefore be ionized in the divertor volume before reaching and polluting the core and are pushed back by the plasma flow towards the targets where they can be exhausted by the pumping system together with the Helium nuclei produced in the fusion reaction, which represent an intrinsic impurity. Of importance for this work is the fact that the divertor configuration also allows for some peak target heat flux reduction by cross-field transport along the path between the X-point and the target, the so-called divertor leg. Even though this manuscript is mainly focused on diverted configurations, limited ones can be thought of as a geometrical simplification that helps the understanding of the PWI and power exhaust problem. In particular we will focus on diverted configurations with a lower single null (LSN), in which the X-point and the strike points lie below the magnetic axis.

1.4.3 Heat transfer in the scrape-off layer

Let us now consider the transfer of heat in the SOL of a tokamak: the simplest way to model it is to imagine that heat coming from the confined plasma core driven by cross-field transport through the magnetic separatrix enters the SOL at a given rate P_{SOL}

and at a generic *upstream* location corresponding, for instance, to the outer midplane. Assuming the absence of losses or other heating sources along the SOL, such heat will flow in a narrow channel made of open magnetic field lines and will then be exhausted at the divertor targets. Two are the main heat transfer mechanisms at play: convection and conduction, that correspond to the propagation of heat with or without transfer of matter respectively. Convection dominates the heat transfer in a weakly collisional plasma in which the particle flux is sufficiently uniform along the length of the SOL: this is the case when the main plasma source, where neutrals are preferentially ionised, is located in the plasma core. In this regime, referred to as *flux-limited*, heat is efficiently conveyed from the upstream location to the target by the particle flux. The heat flux convected by electrons and ions respectively in the direction parallel to magnetic field lines can be written as [7, 8]:

$$q_{\parallel,\mathrm{e}}^{\mathrm{conv}} = \left(\frac{5}{2}k_{\mathrm{B}}T_{\mathrm{e}} + \frac{1}{2}m_{\mathrm{e}}v_{\parallel,\mathrm{e}}^2\right) n_{\mathrm{e}}v_{\parallel,\mathrm{e}} \tag{1.19}$$

$$q_{\parallel,\mathrm{i}}^{\mathrm{conv}} = \left(\frac{5}{2}k_{\mathrm{B}}T_{\mathrm{i}} + \frac{1}{2}m_{\mathrm{i}}v_{\parallel,\mathrm{i}}^2\right) n_{\mathrm{i}}v_{\parallel,\mathrm{i}} \tag{1.20}$$

The two can be added, assuming quasi-neutrality ($n_{\mathrm{e}} = n_{\mathrm{i}} = n$), thermal coupling ($T_{\mathrm{e}} = T_{\mathrm{i}} = T$), ambipolarity ($v_{\parallel,\mathrm{e}} = v_{\parallel,\mathrm{i}} = v_{\parallel}$) and neglecting the electron inertia, to obtain the total convective parallel heat flux:

$$q_{\parallel}^{\mathrm{conv}} = q_{\parallel,\mathrm{e}}^{\mathrm{conv}} + q_{\parallel,\mathrm{i}}^{\mathrm{conv}} = \left(5k_{\mathrm{B}}T + \frac{1}{2}m_{\mathrm{i}}v_{\parallel}^2\right) nv_{\parallel} \tag{1.21}$$

On the other hand in a highly collisional plasma, when the ionisation mean free path is small compared to the plasma volume, the heat transfer in the SOL is dominated by conduction. In this case the neutrals, released mainly at the divertor targets, are ionized preferentially in the SOL. In the presence of such a spatial separation between the upstream heat source and the downstream particle source, heat cannot be exhausted by convection. This leads to the onset of a temperature gradient along field lines that allows heat to be extracted via conduction: we therefore define this regime *conduction-limited*. The parallel heat flux conducted by electrons and ions respectively can be written as [7, 8]:

$$q_{\parallel,\mathrm{e}}^{\mathrm{cond}} = -\kappa_{\parallel,\mathrm{e}}\nabla_{\parallel}T_{\mathrm{e}} = -\kappa_{0,\mathrm{e}}T_{\mathrm{e}}^{5/2}\nabla_{\parallel}T_{\mathrm{e}} \tag{1.22}$$

$$q_{\parallel,\mathrm{i}}^{\mathrm{cond}} = -\kappa_{\parallel,\mathrm{i}}\nabla_{\parallel}T_{\mathrm{i}} = -\kappa_{0,\mathrm{i}}T_{\mathrm{i}}^{5/2}\nabla_{\parallel}T_{\mathrm{i}} \tag{1.23}$$

where $\kappa_{\parallel} = \kappa_0 T^{5/2}$ is the Spitzer-Härm expression for the heat conductivity and $\nabla_{\parallel}$ is the gradient along magnetic field lines. For a hydrogen plasma $\kappa_{0,\mathrm{e}} \sim 2000$ while $\kappa_{0,\mathrm{i}} \sim 60$, meaning that the conductive heat flux is largely dominated by electrons if the two species are thermally well coupled:

$$q_{\parallel}^{\mathrm{cond}} = q_{\parallel,\mathrm{e}}^{\mathrm{cond}} + q_{\parallel,\mathrm{i}}^{\mathrm{cond}} \simeq q_{\parallel,\mathrm{e}}^{\mathrm{cond}} = -\kappa_{0,\mathrm{e}} T^{5/2} \nabla_{\parallel} T \tag{1.24}$$

When talking about the heat flux in the following of this manuscript the reader will alternatively encounter two different notations, depending on the adopted reference system: $q_{\parallel}$, as it was just introduced, is the heat flux parallel to magnetic field lines, while q_{surf} or simply q is the heat flux normal to a material surface, as it is usually estimated via diagnostic systems. Once the incidence angle of the field lines at the target in the toroidal direction, α, is given from an equilibrium reconstruction code, the two can be easily related through the geometrical projection:

$$q_{\parallel} = \frac{q}{\sin \alpha} \tag{1.25}$$

Since in tokamaks $B_{\mathrm{T}} \gg B_{\mathrm{P}}$, the total field B usually reaches the targets with very shallow angles: for example, for $\alpha = 3°$ then $q_{\parallel} \simeq 20q$. Of particular interest for this work are the width and the shape of the profiles of the heat flux along the divertor targets, setting the area wetted by the heat flux on the wall. It is in fact possible to show that for a given power P_{div} flowing, for instance, towards the outer divertor target, the maximum heat flux perpendicular to the surface $q_{\mathrm{surf}}^{\mathrm{max}}$ is determined by the wetted area:

$$q_{\mathrm{surf}}^{\mathrm{max}} = \frac{P_{\mathrm{div}}}{A_{\mathrm{wet}}} \simeq \frac{P_{\mathrm{div}}}{2\pi R_{\mathrm{t}} \lambda_{\mathrm{wet}}} \tag{1.26}$$

where R_{t} is the position of the target along the tokamak major radius and λ_{wet} is the wetted width, equivalent of the wetted area A_{wet} once toroidal symmetry is assumed. Such quantity, that we like to call the *heat flux width*, represents the width of the channel in which heat flows along the SOL and is therefore determined by plasma transport in this complex boundary region. Chapter 2 will be devoted to the definition and parametrisation of the SOL width, that represents one of the main subjects of this thesis.

1.4.4 Divertor material constraints in ITER

The successful and safe operation of future magnetic confinement nuclear fusion reactors like ITER strongly depends on an efficient and controlled handling of the power exhaust. ITER divertor targets are expected to tolerate a heat flux normal to the material surface

up to $q_{\mathrm{surf}} = 10\ \mathrm{MW\,m^{-2}}$ in steady state and of $20\ \mathrm{MW\,m^{-2}}$ during slow transients [9]. Two are the main reasons for these constraints: i) the surface temperature of the Tungsten mono-blocks that will constitute the divertor PFCs has to be lower than the Tungsten recrystallisation temperature which is of about 1300 - 1500 °C not to alter its thermo-mechanical properties; ii) the coolant flowing through the mono-blocks has to remain in its liquid phase to keep the prescribed heat conductivity and ensure efficient heat extraction. It has to be rememberd that these limits refer to pristine, undamaged, tungsten and might have to be corrected when taking into account the effect of plasma fluence and modifications of the divertor design, as recently shown in [10, 11, 12]. Going back to equation 1.26, if one considers the nominal values for ITER ($P_{\mathrm{div}} \simeq 70\mathrm{MW}$, $R_{\mathrm{t}} = 6\mathrm{m}$) one find that, in order to comply with the engineering limit on $q_{\mathrm{surf}}^{\mathrm{max}}$, a λ_{wet} of few cm is required. Present estimates on λ_{wet} based on empirical scaling laws obtained from existing machines, discussed in section 2.4, suggest that this requirement might not be fulfilled. Therefore, in order to limit q_{surf}, ITER will have to be operated in partially detached conditions [13, 14, 15]. *Detachment* consists in a simultaneous decrease of density and temperature at the strike point due to a reduction of pressure along magnetic field lines connecting the divertor target to the upstream plasma. In this regime momentum exchange via cross-field transport or collisional exchange can not be neglected. This phenomenon favours power dissipation through isotropic radiation reducing the particle and heat flux reaching the divertor target. Detached plasmas are beyond the scope of this work, which focuses entirely on attached conditions. A detailed study of the effect of plasma geometry on detachment can be found in [16].

Chapter 2

The width of the scrape-off layer

Contents

2.1 Definition of scrape-off layer width

When talking about the *width* of the SOL we refer here to the perpendicular distance from the magnetic separatrix over which plasma quantities such as n, T and q are spread onto open magnetic field lines. The SOL width, can be understood as a result of the competition between the transport of that quantity in the $\parallel$ and in the $\perp$ directions [8]. In a particle description, when plasma coming from the core reaches a limiter or a divertor target, it has spent as much time travelling through the SOL in the $\parallel$ as in the $\perp$ direction:

$$\tau_{\parallel} = \tau_{\perp} \tag{2.1}$$

For ballistic transport this can be rephrased, in terms of travelled distances and velocities, as follows:

$$\frac{L_{\parallel}}{v_{\parallel}} = \frac{\lambda_{\mathrm{SOL}}}{v_{\perp}} \tag{2.2}$$

where $L_{\parallel}$ is the parallel connection length (length of field lines between the two sides of a limiter, or divertor targets), λ_{SOL} is the SOL width, $v_{\parallel}$ and $v_{\perp}$ are the velocities in the $\parallel$ and $\perp$ direction respectively. This naive, but in some instances effective, description of the problem is conveniently represented by unfolding the poloidal projection of the SOL, as done in figure 2.1. From this sketch (in which the scale of $\parallel$ and $\perp$ directions are different) it is clear how λ_{SOL} is not simply the distance between the separatrix (white dashed line) and the wall (grey box), but rather the distance over which the value of a given SOL quantity is non negligible.

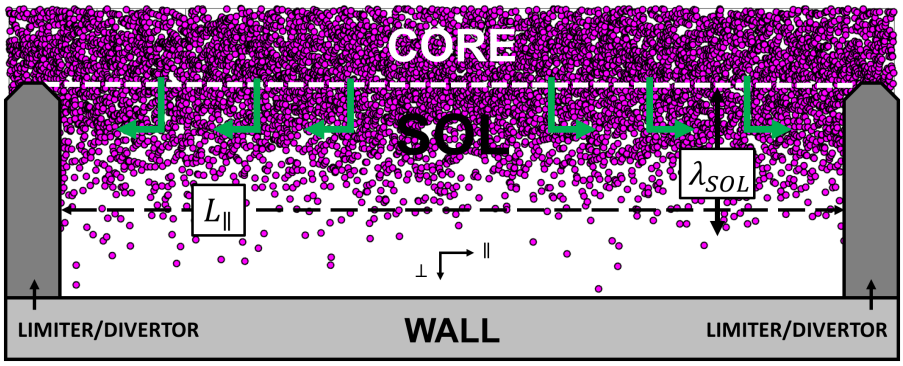

Figure 2.1: unfolded SOL with plasma particles (purple circles), plasma trajectory (green arrows), separatrix (white dashed line), connection length (dashed black arrow), SOL width (solid black arrow), wall (grey box), limiters/divertor targets (dark grey boxes).

If this proportionality of scale lengths and velocities holds, given that plasma transport is much quicker along field lines than transversely, λ_{SOL} is expected to be orders of magnitude smaller than $L_{\parallel}$.

2.1.1 The diffusive SOL width

A simple model of SOL transport can be obtained assuming that plasma travels at sound speed c_s in the $\parallel$ direction while undergoing a *diffusive* random walk in the $\perp$ one. Under these hypotheses, equation 2.2 can be rewritten in the following form:

$$\frac{L_\parallel}{c_s} = \frac{\lambda_{SOL}^2}{D_\perp} \tag{2.3}$$

$$\lambda_{SOL} = \sqrt{\frac{D_\perp L_\parallel}{c_s}} \tag{2.4}$$

This diffusive ansatz is the foundation of MONALISA, a simple transport code used in this work and described in detail in section 4.1.1. By substituting into equation 2.4 the expression for the diffusion coefficient $D_\perp$ associated to one of the transport descriptions presented in section 1.3, we obtain the corresponding formulation of λ_{SOL}. For example, if one considers the classical diffusion coefficient $D_\perp^c = \nu_{coll}\rho_L^2$, one obtains:

$$\lambda_{SOL}^c = \sqrt{\frac{D_\perp^c L_\parallel}{c_s}} = \rho_L \sqrt{\frac{\nu_{coll} L_\parallel}{c_s}} \tag{2.5}$$

where we recognise the definition of collisionality: $\nu^* = \nu_{coll}\tau_\parallel \simeq \nu_{coll} L_\parallel c_s^{-1}$. We can therefore rewrite:

$$\lambda_{SOL}^c = \rho_L \sqrt{\nu^*} \propto \frac{1}{B}\sqrt{\nu^*} \tag{2.6}$$

which predicts a dependence of the SOL width on the square root of the collisionality and on the inverse of the total magnetic field. If one uses the neoclassical diffusion coefficient $D_\perp^{nc} = \nu_{coll}\left(q_{cyl}\rho_L\right)^2$ instead, one obtains the expression:

$$\lambda_{SOL}^{nc} = \sqrt{\frac{D_\perp^{nc} L_\parallel}{c_s}} \simeq q_{cyl}\rho_L\sqrt{\nu^*} \propto \frac{a}{R}\frac{1}{B_P}\sqrt{\nu^*} \tag{2.7}$$

In this approximation the SOL width exhibits a inverse dependence on both the machine aspect ratio R/a and the poloidal component of the magnetic field B_P. In the case of a turbulent description, approximated through Bohm diffusion ($D_\perp^B = \rho_L c_s$), one finds:

$$\lambda_{SOL}^B = \sqrt{\frac{D_\perp^B L_\parallel}{c_s}} = \sqrt{\rho_L L_\parallel} \tag{2.8}$$

By approximating $L_{\parallel} \simeq \pi R q_{\mathrm{cyl}}$, it is possible to derive the following expression:

$$\lambda_{\mathrm{SOL}}^{\mathrm{B}} \simeq \sqrt{\rho_{\mathrm{L}} \pi R q_{\mathrm{cyl}}} \propto \sqrt{\frac{a}{B_{\mathrm{P}}}} \tag{2.9}$$

where the SOL width depends on the square root of the minor radius and the inverse of the square root of the poloidal field.
From this series of examples it emerges clearly how the dependences of λ_{SOL} on engineering parameters of the machine, like its geometry or the strength of the magnetic fields, are extremely sensitive to the assumptions on the dominant mechanism at play one makes when modelling the transport of the plasma. The importance of B_{P} in setting, for instance, the heat flux width has been observed also experimentally on a large number of machines, as discussed in section 2.4, while the role of machine size and aspect ratio are non-trivial to capture. The notation used so far was intentionally generic since different SOL quantities (n, T and q) might be transported at different effective velocities and therefore their profiles could be characterized by different widths. Although the main focus of this work will be on the heat flux width λ_q, its link with the density and temperature widths, λ_n and λ_T respectively, are important matter for discussion.

2.1.2 The drift-based SOL width

Another interpretation of the SOL width problem can be given by considering magnetic vertical drifts as the main convection mechanism. In this case equation 2.2 would read:

$$\frac{L_{\parallel}}{c_{\mathrm{s}}} = \frac{\lambda_{\mathrm{SOL}}^{\mathrm{db}}}{v_{\mathrm{drift}}} \tag{2.10}$$

where, substituting $v_{\mathrm{drift}} = T/BR$ and $L_{\parallel} = \pi R q_{\mathrm{cyl}}$, we obtain the drift-based SOL width:

$$\lambda_{\mathrm{SOL}}^{\mathrm{db}} = \frac{\pi R q_{\mathrm{cyl}}}{c_{\mathrm{s}}} \frac{T}{RB} = \frac{\pi R q_{\mathrm{cyl}}}{c_{\mathrm{s}}} \frac{\rho_{\mathrm{L}} c_{\mathrm{s}}}{R} \simeq q_{\mathrm{cyl}} \rho_{\mathrm{L}} \tag{2.11}$$

This expression basically coincides with the the neoclassical SOL width derived in equation 2.7 in the limit of $\nu^* = 1$. SOL models based on these hypotheses are present in the literature since several decades [17]. However, a recent revisiting quickly reached a considerable popularity due its experimental-friendly approach: the *heuristic drift-based* (HD) model proposed by R.J. Goldston in 2012 [18]. The main assumption of this meta-model, whose validity is explicitly said to be limited to low (or null) gas puff H-mode diverted plasmas, is that the effect of turbulence can be neglected and that the SOL width is determined by the radial displacement of ions and electrons due to neoclassical

grad$B$ and curv$B$ drifts integrated over the parallel path from the outer midplane to the X-point. The plasma pushed across the separatrix by such drifts is then transported in the SOL by two types of flows: *i*) parallel flows directed to the divertor targets acting as effective sinks for the plasma, assumed to be attached, and *ii*) Pfirsch-Schlüter flows, pushing particles upwards due to the parallel pressure gradient between the X-point and the top of the plasma. Such flows are supposed to be of the same order of magnitude with $|v_{\parallel}| \simeq 0.5 c_{\mathrm{s}}$. This hypothesis might lead to a strong underestimation of parallel transport: in fact, recent numerical simulations carried out by Giorgiani et al. with an isothermal reduced model showed how SOL parallel flows can be supersonic [19]. The resulting density width scales with the following main dependences:

$$\lambda_n^{\mathrm{HD}} \propto \frac{a}{R}\frac{1}{B_{\mathrm{P}}}\sqrt{T_{\mathrm{sep}}} \tag{2.12}$$

where we recognize the same proportionality to a/R and $1/B_{\mathrm{P}}$ already found for $\lambda_{\mathrm{SOL}}^{\mathrm{nc}}$ in section 2.1.1. The second fundamental assumption is that the dominant heat transport across the separatrix is due to anomalous electron thermal diffusion, which can effectively *fill* with heat the channel *opened* by magnetic drifts. The heat flux width is therefore inferred using the expression λ_n^{HD} and the two-point model [8]:

$$\lambda_q^{\mathrm{HD}} \propto \frac{P_{\mathrm{SOL}}^{1/8} a^{17/8} B^{1/4}}{I_{\mathrm{P}}^{9/8} R}\left(1+k^2\right)^{5/8} \tag{2.13}$$

This scaling law, besides the role played by the elongation, predicts a weak impact of the power entering the SOL P_{SOL} and of the total magneti field. On the other hand the important dependencies are, again, $\lambda_q^{\mathrm{HD}} \propto a^2 I_{\mathrm{P}}^{-1} R^{-1} \propto B_{\mathrm{P}}^{-1} a R^{-1}$. The inverse dependence on the poloidal field is a feature that the HD model shares with experimentally obtained scaling laws for λ_q in both L-mode and H-mode discharges, to be detailed in section 2.4. The proportionality to a/R is conversely something that was not straightforwardly highlighted by measurements in H-mode discharges. Such scaling law predicts $\lambda_q \simeq 1$ mm for ITER, which is also in line with experimental extrapolations [20]. Overall, the strength and weakness of the HD model lies in its "Frankenstein" nature: different regions of the plasma are independently described by different bits of physics coming mostly from experimental observations. Since predictions in the range of $\lambda_q \simeq$ "few millimeters" for H-mode discharges in most of the present tokamaks are in line with what is routinely measured, this meta-model received a warm welcome from experimentalists that, in some cases, used it to support their results even in conditions that are beyond the assumptions made by the author. The important contribution of the HD model consists, in our

opinion, in the translation of results know from neoclassical theory in terms of explicit dependencies on engineering parameters allowing for better comparison with empirical scaling laws.

2.1.3 The turbulent SOL width

A turbulent definition of the SOL width can be given by providing an expression for $v_\perp$ based on the properties of plasma fluctuations. These fluctuations are also referred to as *blobs* (or *filaments*) because of their highly local nature (in both time and space) which make them stand out from the background plasma. By following the method of a recent work on the link between blob features and the density SOL width carried out by N. Fedorczak et al. [21], one can characterize density blobs through their amplitude n_b, velocity v_b, duration τ_b and frequency f_b. Since most of the cross-field particle flux in the outer midplane region of a tokamak SOL is carried by blob transport, given equation 1.12, we can write:

$$\Gamma_\perp^\mathrm{turb} = \langle \tilde{n}\tilde{v}_{E\times B}\rangle_{t,\phi} = n v_\perp^\mathrm{turb} = \Gamma_\mathrm{b} d_\mathrm{b} = n_\mathrm{b} v_\mathrm{b} \tau_\mathrm{b} f_\mathrm{b} \tag{2.14}$$

where $\Gamma_\mathrm{b} = n_\mathrm{b} v_\mathrm{b}$ is the flux carried by the average blob and $d_\mathrm{b} = \tau_\mathrm{b} f_\mathrm{b}$ is the duty cycle. This provides an expression for the turbulent time-averaged perpendicular velocity:

$$v_\perp^\mathrm{turb} = \frac{n_\mathrm{b}}{n} d_\mathrm{b} v_\mathrm{b} \tag{2.15}$$

which, when plugged in equation 2.2, returns an expression of the turbulent density width:

$$\lambda_n^\mathrm{turb} = \frac{L_\parallel}{c_\mathrm{s}} \frac{n_\mathrm{b}}{n} d_\mathrm{b} v_\mathrm{b} \tag{2.16}$$

From the last equation it can be concluded that, supposing $L_\parallel$ and c_s to be set by the magnetic configuration and the plasma scenario, measuring or estimating the average blob velocity is not enough to predict λ_n^turb: in fact v_b needs to be weighted by the duty cycle and the blob amplitude with respect to the background. Such approach was found to be in quantitative agreement with experimental data from limited discharges in the Tore Supra tokamak, for which $\lambda_n \simeq 4$ cm, $L_\parallel \simeq 60$ m, $c_\mathrm{s} \simeq 6 \times 10^4$ m s^{-1}, $d_\mathrm{b} \simeq 10\%$, $n_\mathrm{b}/n \simeq 1.3$, $v_\mathrm{b} \simeq 100 - 300$ m s^{-1}. Assuming to be in the flux-limited regime, the model predicts the following expression of the heat flux width in terms of engineering parameters:

$$\lambda_q^\mathrm{turb} = 0.5 R q_\mathrm{cyl}^{0.75} \left(\frac{\rho_\mathrm{L}}{R}\right)^{0.55} \tag{2.17}$$

in which, again, we find a dependence on the poloidal field ($B_{\mathrm{P}}^{-0.75}$) and on the geometry ($a^{0.75}R^{-0.3}$) which, regardless of the way one tries to model the SOL width, seem to be the main players. Validation of the model against data from diverted configuration is ongoing. Besides averaging quantities in order to extract a numerical estimate, one has to remember that, due to the highly fluctuating nature of the SOL, defining a width might become a very abstract exercise.

2.2 Measurement of SOL profiles

2.2.1 SOL diagnostics

The experimental assessment of n, T and q SOL profiles and therefore our capability to estimate the corresponding widths relies on a handful of measurement systems, referred to as diagnostics. The most important, as well as the ones used to acquire the majority of the experimental data presented in this thesis, are *Langmuir probes*, *infrared thermography* and *Thomson scattering*. A Langmuir probe consists in an electrode that can attract or repulse charged particles in a plasma depending on the applied voltage [22]. The current flowing in an electrode measured as a function of the applied voltage, the $I-V$ characteristic, gives information on n_{e} and T_{e} in the vicinity of the probe. According to standard sheath theory [8], the heat flux can be inferred from LP data as $q^{\mathrm{LP}} = e\Gamma_{\mathrm{e}}\left(\gamma T_{\mathrm{e}} + E_{\mathrm{pot}}\right) = en_{\mathrm{e}}c_{\mathrm{s}}\left(\gamma T_{\mathrm{e}} + E_{\mathrm{pot}}\right)$, where $E_{\mathrm{pot}} = 13.6 + 2.2$ eV is the potential energy associated to each ion accounting for hydrogen ionization energy and half of the molecular binding energy. Assumptions also have to be made regarding the value of the *sheath heat transmission coefficient* γ which is know to depend on the ratio $T_{\mathrm{i}}/T_{\mathrm{e}}$. However, measurements of T_{i} are hardly available in most tokamaks. For this reason it is alternatively chosen $\gamma = 8$ if one assumes $T_{\mathrm{e}} = T_{\mathrm{i}}$ (hot ions) or $\gamma = 5$ if one supposes $T_{\mathrm{i}} \simeq 0$ (cold ions). Langmuir probes can be embedded in the PFCs to assess plasma conditions in the vicinity of material surfaces as limiters or divertor targets: in this case the signal from multiple neighbouring probes is necessary to reconstruct n_{e} and T_{e} profiles along the PFC. In the following we will refer to this kind of probes as LP. Langmuir probes can also be mounted on a reciprocating arm that plunges from the vessel wall into the plasma, typically down to the separatrix. If the plunge is quick enough one can assume that along its trajectory the probe tip acquires n_{e} and T_{e} profiles that are instantaneous. We will label this type of probes as RCP. It should be remembered that the one measured by the RCP is a plasma perturbed by the insertion of a solid object: such perturbation has to be modeled and taken into account, as done in [23] and references therein. Infrared thermography (IR), rather than measuring plasma properties, consists

instead in assessing the surface temperature T_{surf} of the PFCs in the field of view of a camera. From the 2D map of T_{surf} thermal calculations based on a diffusive model [24] allow the estimation of the heat flux reaching the material surface q_{surf}. Unlike with LP and RCP, the heat flux measured via IR in the sum of all the contributions reaching the PFC (electrons, ions, radiation, etc.) that cannot be disentangled. Such estimation strongly depends on the value assumed for the emissivity of the PFCs. Thomson scattering (TS) consists in firing a laser through the plasma and collect with a spectrometer the radiation that is elastically scattered by charged particles. This non-intrusive method allows to infer n_{e} from the intensity of the scattered radiation and T_{e} from the broadening of the spectrum [25].

2.2.2 Remapping and comparability

Any investigation of SOL widths that aims at being more general than simply characterize a single discharge has to adopt a reference system that allows one comparing discharges achieved in different magnetic equilibria or even in different devices, regardless of the size and shape of the machines. Also one might want to assess the poloidal variation of the SOL width and try to reconcile profiles measured in the main plasma and at the limiters/divertor targets. A conventionally adopted method consists in "remapping" SOL profiles to a reference location: the outer midplane. This is done under the hypothesis that $\parallel$ transport is strongly predominant over the $\perp$ one. The remapping process, sketched in figure 2.2.a, is performed along magnetic flux surfaces, where the value of ψ is constant. To any array of positions, for instance along the divertor target, an array of points with the same ψ value exists at the outer midplane. With this in mind, in the following we will use the notation y^{tgt} for IR and LP profiles as measured at the target while the corresponding remapping at the outer midplane will be simply labelled as y. The same will be done with the widths that characterize the profiles obtained through the parametrisations to be introduced in section 2.3. Similarly, when referring to RCP and TS profiles acquired anywhere in the main SOL, we consider the outer midplane remap. Such remapping procedure approximately corresponds to dividing the local length scale of the profiles by the poloidal *flux expansion* f_{x} [26]. The latter can be defined as the ratio of the distance between flux surfaces at the measurement location δ^{loc} and at the outer midplane δ. This implicitly assumes that f_{x} does not vary significantly along the considered profile. For this reason, most of the profiles show in the following of this manuscript will be plot as a function of the radial distance from the outer midplane separatrix $(R-R_{\mathrm{sep}})^{\mathrm{omp}} \simeq (R-R_{\mathrm{sep}})^{\mathrm{loc}}/f_{\mathrm{x}}$, simply referred to as $R-R_{\mathrm{sep}}$. As an example, in figure 2.2.b and c, heat flux profiles measured at the outer divertor target of the TCV

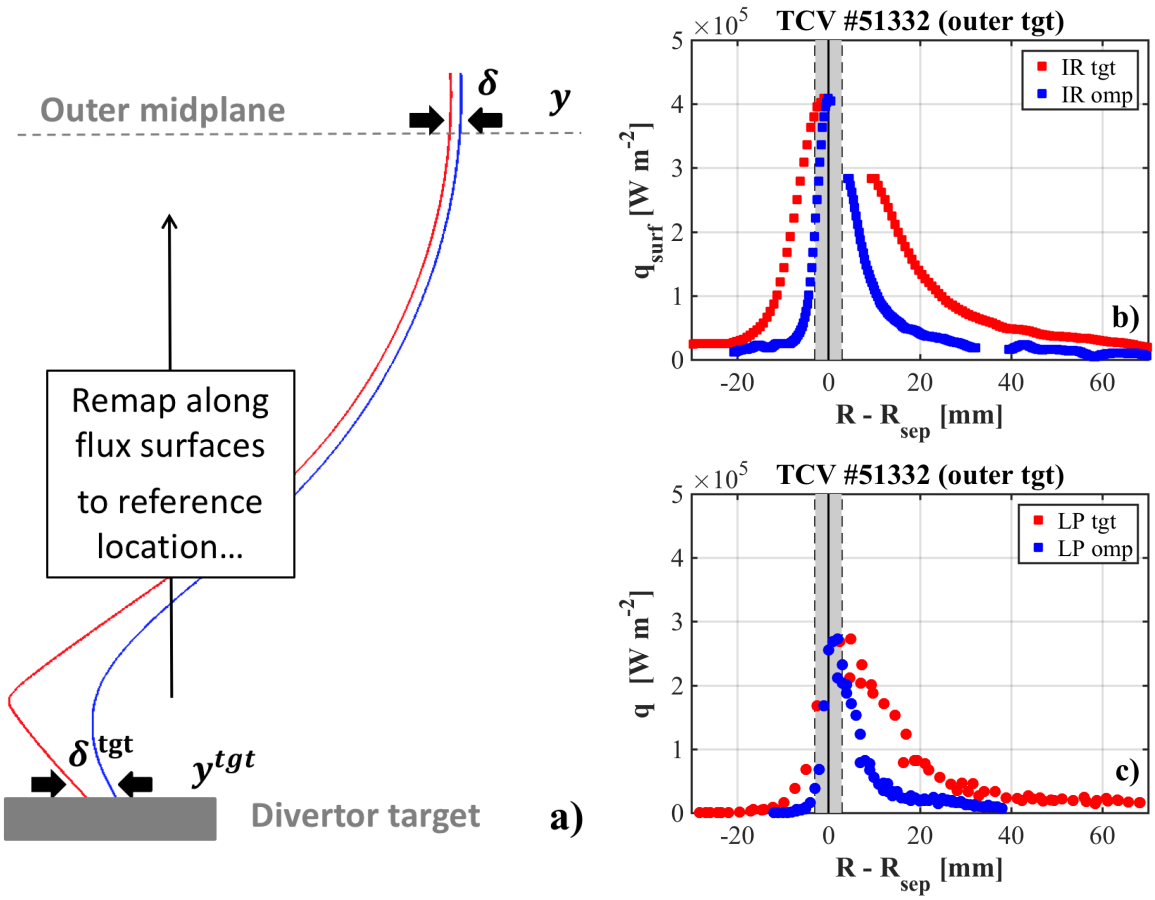

Figure 2.2: a) sketch of the remapping of an outer divertor profile (y^{tgt}) to the outer midplane (y); b) IR and C) LP q profiles at the target (red) and remapped at the outer midplane (blue). In grey is the separatrix position assuming a ± 3 mm uncertainty.

tokamak with IR and LP respectively are superimposed: red markers indicate q profiles along the target coordinate, while blue ones refer to the outer midplane remap. Overall the remapping of the profiles corresponds to a coordinate transformation in which profiles are "squeezed" in the radial direction.

2.3 Parametrization of SOL profiles

2.3.1 SOL width in limited plasmas

In order to assess their widths, one has to efficiently parametrize radial profiles of SOL quantities (n, T, q). Such profiles might have different widths at different poloidal locations because of the flaring of magnetic flux surfaces. In a limited configuration the plasma core represents the source of particles and heat (purple region in figure 2.3). The SOL width is a balance between $\parallel$ transport towards the limiter and $\perp$ transport

towards the vessel wall, both acting simultaneously as sinks of plasma and sources of neutrals because of recycling (see section 1.4.1). This yields, for a generic SOL quantity y, exponentially decaying radial profiles of the form:

$$y\left(r\right) = y_0 \, \exp\left(-\frac{r}{\lambda_y \, f_{\mathrm{x}}}\right) \tag{2.18}$$

where y_0 is the separatrix value, $r = \left(R - R_{\mathrm{sep}}\right)^{\mathrm{loc}} = \left(R - R_{\mathrm{sep}}\right)^{\mathrm{omp}} \cdot f_{\mathrm{x}} \geq 0$ is the local radial distance from the separatrix and the decay length λ_y approximates the SOL width.

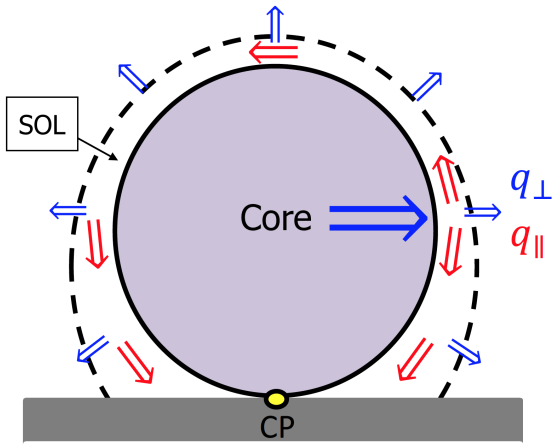

Figure 2.3: sketch of a limited configuration showing core (purple), separatrix (black solid line), a generic SOL ψ surface (black dashed line), SOL (white), limiter (grey), contact point (CP, yellow), heat fluxes parallel and perpendicular to magnetic ψ surfaces (red and blue arrows).

In limited, low-confinement-mode (L-mode), plasma discharges, SOL widths were found to be of the order of centimeters in many devices. In the Tore Supra tokamak [27], for instance, RCP measurements by Gunn et al. [28] showed that $\lambda_{n_{\mathrm{e}}} \simeq 2 - 3$ cm when the plasma is limited on the outer wall (low field side, LFS) while it can go up to $10 - 20$ cm when the contact point lies on the inner column (high field side, HFS). This is a strong evidence that radial turbulent transport is enhanced in the region surrounding the outer midplane (thick blue line in figure 2.3): when the plasma is limited on its outboard side such transport is damped and the SOL width shrunk by an order of magnitude. Widths of ion and electron temperature profiles, assessed in Tore Supra with a retarding field analyser [29], also appeared to be in the same range: $\lambda_{T_{\mathrm{e}}} \simeq 3$ cm and $\lambda_{T_{\mathrm{i}}} \simeq 4$ cm. Finally, in the same machine, an heat flux width of $\lambda_q \simeq 1.5$ cm was estimated from IR data by Corre et al. [30]. The effort in studying L-mode HFS limited plasmas is still considerable as this is the configuration foreseen for start-up phase in ITER. A large database of this

kind of discharges was recently put together by Horacek et al. [31]: RCP measurements from most of the existing devices fall in the range $\lambda_q = 1 - 10$ cm. Heat flux profiles in HFS limited plasmas often exhibit two decay lengths: a near-SOL one (few mm) close to the separatrix and a far-SOL one (few cm) characterizing the remaining of the radial profile have been observed on a number of devices [32]. Limited plasmas and the so-called "narrow feature" are beyond the scope of this work.

2.3.2 SOL width in diverted plasmas

The parametrization of SOL profiles in diverted configuration is more complex: profiles might have different widths and shapes at different poloidal locations not only due to flux expansion but also because diverse are the source and sink terms that are locally at play. As sketched in figure 2.4 for a LSN configuration, the SOL is conventionally divided in 1) the main SOL, above the X-point and surrounding the main plasma, and 2) the divertor SOL, below the X-point and further separated in private (PFR) and common (CFR) flux region.

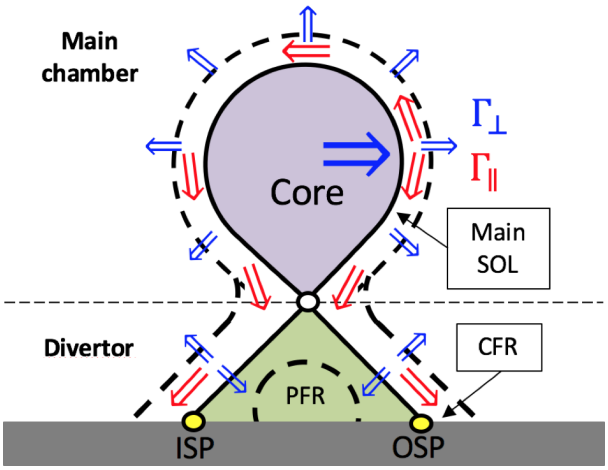

Figure 2.4: sketch of a diverted configuration showing core (purple), separatrix (black solid line), a generic SOL ψ surface (black dashed line), main SOL (white), CFR (white), PFR (green), divertor target (grey), inner and outer strike points (ISP and OSP, yellow), plasma fluxes parallel and perpendicular to magnetic ψ surfaces (red and blue arrows).

In the main SOL, profiles can be parameterized as decaying exponential as for limited configurations (see section 2.3.1). In the divertor SOL, instead, the plasma from the main SOL enters the CFR and is lost perpendicularly on either side, towards the vessel wall and in the PFR. This corresponds to a diffusion of the main SOL profiles in the $\perp$ direction, with two consequences: *i*) profiles get broader, increasing the wetted width at the targets, and *ii*) the peak gets lower and shifts away from the magnetic strike

point in the CFR as a result of the roll-over in the PFR [33]. Under these hypotheses, divertor SOL profiles can be described by the convolution of a decaying exponential with a Gaussian [34]:

$$y(r) = \frac{y_0}{2} \exp\left(\left(\frac{S_y}{2\lambda_y}\right)^2 - \frac{r}{\lambda_y f_x}\right) \operatorname{erfc}\left(\frac{S_y}{2\lambda_y} - \frac{r}{S_y f_x}\right) + y_{bg} \tag{2.19}$$

where S_y is the width of the Gaussian called *spreading factor* and y_{bg} is the background value. Negative values of r refer to the PFR. It is assumed here that λ_y is dependent only on the upstream SOL parameters and on $L_\parallel$ from the outer midplane to the X-point. Therefore λ_y represents the scale lengths of radial transport in the main SOL. On the other hand S_y is the corresponding scale length for the divertor SOL region assuming a purely diffusive, radially and poloidally homogeneous, transport and expected to depend only on local divertor conditions and geometry. This parametrisation is based on the hypothesis that the main transport mechanisms at play in main SOL and divertor SOL are different, sharply dividing the field lines in two regions along the parallel direction at the X-point. As anticipated in section 2.2.2, profiles are parametrized after remapping at the outer midplane by assuming that trivial details of the magnetic geometry (flaring of flux surfaces and their tilting with respect to divertor targets) can be removed through f_x. Concerning the heat flux, for example, both λ_q and S_q, as well as of course f_x, will concur setting the overall λ_{wet} at the target. A good estimate of this quantity can be given through the so-called *integral* width [26]:

$$\lambda_{wet} = f_x \lambda_{int} = f_x \frac{\int (q(r) - q_{bg})\, dr}{q_{max} - q_{bg}} \tag{2.20}$$

which directly links the profile width with q_{max} that has to respect the material constraints discussed in section 1.4.4. In particular, for profiles that are well described by eq. 2.19, one can approximate $\lambda_{int} \simeq \lambda_q + 1.64\, S_q$, as shown in [35]. Besides causing a broadening of SOL profiles in the divertor region, the presence of a null point in the magnetic configurations has important consequences also on the width of main SOL profiles. Close comparison between HFS limited and LSN discharges achieved in the DIII-D tokamak with similar plasma parameters [36] testifies that n_e and T_e profiles from RCP measurements close to the outer midplane are several times narrower in LSN ($\lambda_{n_e}^{lim} = 3.7$ cm vs $\lambda_{n_e}^{LSN} = 1.1$ cm, $\lambda_{T_e}^{lim} = 6$ cm vs $\lambda_{T_e}^{LSN} = 1$ cm). One can imagine that a narrower SOL could be related to the damping of radial turbulent transport caused by the magnetic shear introduced at the creation of an X-point. Despite the fact that a satisfactory explanation of such SOL narrowing still has to be provided, experimental observations of heat

flux widths $\lambda_q \leq 1$ cm in diverted L-mode discharges on different machines have been consistently reported. A good example is constituted by very recent heat load studies in TCV [37, 38, 39] where $\lambda_q = 5 - 10$ mm is estimated with good agreement between LP and IR. This experiment is extensively described in chapter 3. Previous IR studies on the divertor targets of JET (D_2, H_2) and AUG (D_2) report $\lambda_q = 3 - 7$ mm during L-mode discharges [40] and $\lambda_q = 1 - 4$ mm during H-mode discharges [34, 20, 41, 42]. Similar H-mode experiments on DIII-D and C-mod revealed basically the same range of λ_q [35]. TS measurements in the main plasma of AUG during H-mode discharges [43] show that $\lambda_{n_e} = 6 - 11$ mm while $\lambda_{T_e} = 5 - 8$ mm. Both these upstream scale lengths increase when the plasma reaches detachment. Heat flux decay lengths calculated from TS data assuming that the plasma is in the conduction-limited regime ($\lambda_q = 2\lambda_{T_e}/7$) are in good agreement with those from the IR measurements mentioned above. On the other hand, in the literature, the divertor spreading factor is basically investigated only in IR heat flux profiles (S_q): in JET and AUG, it is found to be in the range $S_q = 0.25 - 1.5$ mm regardless of the confinement mode but with a pretty clear dependence on the shape of the divertor [44]. In many devices $S_q \simeq 0.5\lambda_q$ during H-mode discharges [20, 41, 42]. In TCV L-mode discharges $S_q = 2 - 3$ mm [37, 38, 39]. Besides the need for understanding of the physics as well as of the control parameters that determine these widths, discussed in section 2.4, a general observation can already be made: both the use of a diverted magnetic configuration and the H-mode, considered crucial steps towards high performance tokamak operations, come with the price of reducing the SOL width and therefore the volume available for power dissipation as well as the wetted area on the divertor. Such narrowing, which is only partially compensated by the divertor spreading, is the inevitable consequences of improved core confinement, which implies weaker radial transport.

2.3.3 Limitations and uncertainties

Despite establishing itself as a standard and effective tool used in the vast majority of heat load studies in present tokamaks, equation 2.19 has a finite "operational window" as specified in [34]: for profiles in which $S_q > 0.7\lambda_q$, the assumption that the divertor broadening can be modelled as a 1D diffusion can lead to an error $> 6.5\%$ when benchmarked with 2D numerical heat diffusion calculations [45]. Heat load studies on a number of devices show that, for H-mode high-performance dischargers, $S_q \simeq 0.4\lambda_q$ [20], ensuring that such an intrinsic error is on average of a few % over the entire database. Another important point when evaluating uncertainties related to equation 2.19 is the

link between the global fit accuracy, given by least square minimisation

$$\chi = \sqrt{\langle (y_{\text{exp}} - y_{\text{fit}})^2 \rangle / \langle (y_{\text{exp}} - y_{\text{bg}})^2 \rangle} \tag{2.21}$$

and the error associated to the estimation of each free parameter, with focus on the two widths λ_y and S_y. Such link can be estimated by using equation 2.19 to build a synthetic divertor SOL profile $y^* = y(y_0^*, y_{\text{bg}}^*, x_0^*, \lambda_y^*, S_y^*)$ to which we add a multiplicative, experimental-like, random noise $n = \sigma \text{rand}(n) y^*$, where $\text{rand}(n)$ is a random number from a normal distribution between 0 and 1 and σ is the amplitude. First the global error χ is found to coincide with σ. Second, by repeating the process 100 times for each value of $\sigma = [0 : 0.01 : 0.3]$, one can calculate the relative errors $\chi_{\lambda_y} = \text{std}(\lambda_y)/\lambda_y^*$ and $\chi_{S_y} = \text{std}(S_y)/S_y^*$. As displayed in figure 2.5, χ_{λ_y} and χ_{S_y} represent a fraction of σ which is strongly dependent on the assumed ratio S_y^*/λ_y^*. In particular, for a common $S_y^* = 0.4\lambda_y^*$ (blue circles), $\chi_{\lambda_y} < 0.5\chi$ and $\chi_{S_y} < 0.8\chi$.

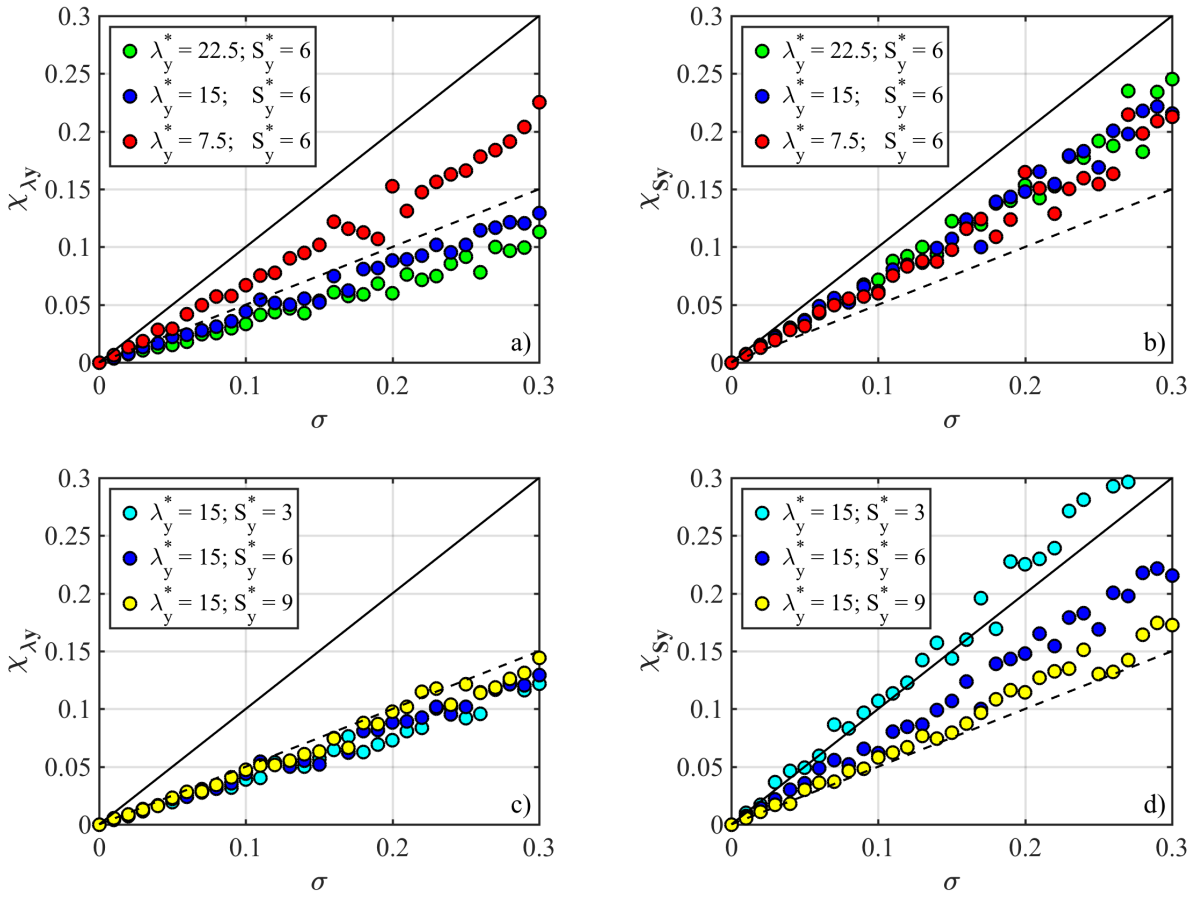

Figure 2.5: relative error on λ_y (χ_{λ_y}) and S_y (χ_{S_y}) of a synthetic profile based on equation 2.19 as a function of a white noise σ. Scans of λ_y^* and S_y^* in a,b) and c,d) respectively.

This ensures that taking χ as errorbar when plotting λ_y and S_y estimates, as routinely done in the following of this work, represents a conservative approach. Interestingly, when scanning λ_y^* (figure 2.5.a-b), χ_{S_y} is not significantly affected while χ_{λ_y} increases as λ_y^* decreases, and therefore χ_{λ_y}/χ tends to unity for $\lambda_y^* \simeq S_y^*$. Similarly, when scanning S_y^* no big variation of χ_{λ_y} is observed (figure 2.5.c-d). On the other hand χ_{S_y} increases with decreasing S_y^* but, even for a small $S_y^*/\lambda_y^* = 0.2$, χ is still a reasonable estimate of the error on S_y. Despite what one might think when looking at figure 2.5, it should be remembered that λ_y and S_y are not decorrelated, although the relative errors might be.

2.4 Scaling laws and extrapolations to ITER

In order to understand the physics governing SOL widths and to make predictions for future devices like ITER, one can look for dependencies on plasma control parameters (B_T, B_P, I_P, q_cyl, a, R, P_SOL, heating power P_h, etc.) in existing devices to create scaling laws. This is usually done by performing regressions on a database of discharges achieved in one or more machines under diverse conditions. Most of the existing scaling laws concern the heat flux width (λ_q, S_q) since the handling of the heat flux is a challenge for ITER operation, as discussed in section 1.4.4.

2.4.1 Multi-machine scaling law for λ_q in H-mode

The most popular scaling law for the inter-ELM λ_q stems from a multi-machine database built using IR $q_\parallel$ profiles measured a the outer divertor target during attached H-mode D_2 discharges in tokamaks with D-shaped section (JET, AUG, DIII-D and C-mod) as well as spherical ones (NSTX and MAST) [20]. A power law regression ($\lambda_q = C \times X^x Y^y Z^z ...$) of control parameters identified that the most significant dependence is the one on B_P at the outer midplane ($B_\mathrm{P,omp}$):

$$\lambda_{q,\mathrm{scaling}}^{\mathrm{H\text{-}mode}} = (0.63 \pm 0.08) B_\mathrm{P,omp}^{-1.19\pm0.08} \tag{2.22}$$

This scaling law predicts a very small value of $\lambda_{q,\mathrm{ITER}}^{\mathrm{H\text{-}mode}} \simeq 1$ mm for the foreseen ITER $I_\mathrm{P} = 15$ MA scenario, narrower than the previous $3-3.5$ mm estimates based mostly on JET ELM-averaged data [9]. The existence of such a common trend among tokamaks with different vessel shape, size and aspect ratio would suggest that, if λ_q depends on any machine-specific feature like, for instance, the magnetic geometry of the divertor, this dependence is weak compared to the one on $B_\mathrm{P,omp}$ (and therefore on I_P, if a and k are constant). This would be consistent with the definition of λ_q as a purely main SOL

quantity [34]. Moreover, the absence of a major radius dependence would imply that we should not expect λ_q to be higher in future larger machines.

2.4.2 JET and AUG scaling law for λ_q in L-mode

A similar analysis, although restricted to AUG (D_2) and JET (D_2 and H_2), was carried out for attached L-mode discharges [40]. The regression with the overall best fit ($R^2 = 0.93$) is obtained by considering H_2 JET discharges only:

$$\lambda_{q,\mathrm{JET,H_2}}^{\text{L-mode}} = (1.86 \pm 0.45) B_{\mathrm{T}}^{-0.66\pm0.19} q_{95}^{0.93\pm0.25} P_{\mathrm{SOL}}^{0.29\pm0.07} \tag{2.23}$$

predicting $\lambda_{q,\mathrm{ITER}}^{\text{L-mode}} \simeq 4.4$ mm. When considering instead both H_2 and D_2 discharges, the fit quality drops down to $R^2 = 0.49$ and the scaling coefficients/exponents change significantly. This indicates an important effect of the fuelling gas on the physics governing λ_q. The best fit to AUG-only D_2 data ($R^2 = 0.79$) comes from the regression:

$$\lambda_{q,\mathrm{AUG,D_2}}^{\text{L-mode}} = (4.37 \pm 2.64) B_{\mathrm{T}}^{-2.41\pm1.04} q_{95}^{1.32\pm0.49} P_{\mathrm{SOL}}^{0.27\pm0.17} \tag{2.24}$$

which is also much different from the previous ones. The regression that best fits ($R^2 = 0.60$) the IR λ_q data from both devices with all fuelling gases is:

$$\lambda_{q,\mathrm{JET+AUG}}^{\text{L-mode}} = (1.58 \pm 0.83) B_{\mathrm{T}}^{-0.40\pm0.31} q_{95}^{0.73\pm0.32} P_{\mathrm{SOL}}^{0.13\pm0.11} R^{0.26\pm0.30} \tag{2.25}$$

where q_{95} is the safety factor at $0.95a$ along the outer midplane, also called *edge* safety factor. Such scaling predicts $\lambda_{q,\mathrm{ITER}}^{\text{L-mode}} \simeq 4.9$ mm. Interestingly this expression highlights a dependence on R, and therefore on the machine size, whose importance is hard to evaluate because of the large error bars in the exponents. Besides the strong dependence on B_{T} in equation 2.24, the leading term in the various regressions is q_{95} to the power $\simeq 1$. If we approximate $q_{95} \simeq q_{\mathrm{cyl}} \propto aR^{-1}B_{\mathrm{T}}B_{\mathrm{P}}^{-1}$ we find the inverse proportionality with respect to B_{P} of the H-mode multi-machine scaling and the dependence on the inverse of the aspect ratio, often recovered in the various definition of SOL width give in section 2.1. However, the author concludes that the major radius dependence is most probably an artefact and rules it out, possibly in search for a better analogy with the H-mode scaling. This allows for a simple "thumb rule" to be proposed for JET and AUG: $\lambda_q^{\text{L-mode}} \simeq 2\,\lambda_q^{\text{H-mode}}$, with similar dependence on control parameters.

2.4.3 Scaling laws for S_q

A scaling law for S_q was built for attached L-mode D_2 and H_2 discharges in AUG with low recycling divertor conditions, highlighting a strong dependence on two upstream parameters as the edge eletron density $n_{e,95}$ and B_P [42]:

$$S_{q,\text{AUG1}}^{\text{L-mode}} = (0.09 \pm 0.01) n_{e,95}^{1.02\pm0.03} B_P^{-1.01\pm0.05} \tag{2.26}$$

Successive studies on H-mode data from JET and AUG, with the latter in the open (divI) divertor configuration [44], showed a weaker dependence on plasma density but highlighted a role played by the major radius, with S_q in JET systematically bigger than in AUG:

$$S_{q,\text{JET+AUG}}^{\text{H-mode}} = (0.12 \pm 0.07) P_{SOL}^{0.21\pm0.11} n_e^{-0.02\pm0.23} B_P^{-0.82\pm0.27} R^{0.71\pm0.50} \tag{2.27}$$

A more recent and complex scaling law for L-mode AUG discharges in low recycling is explicitly based on target conditions n_e^{tgt} and T_e^{tgt}, on the mass number of the main ion species A and corrected by the Larmor radius to account for gyration effects [46]:

$$S_{q,\text{AUG2}}^{\text{L-mode}} = 1.42 \frac{\rho_L}{f_x} + 2.11 T_{e,tgt}^{-1.28} n_{e,tgt}^{0.66} A^{-0.84} B_P^{-1.33} \tag{2.28}$$

The common feature of all these scaling laws is the dependence on B_P (and therefore I_P) to the power $\simeq -1$, already found for λ_q (sections 2.4.1 and 2.4.2). Also, unlike λ_q this time, density is always present in the scaling laws, whether it's the target or the upstream one, suggesting a tighter relation between spreading factor and the operational regime. Moreover S_q was found to increase when switching from the open to the closed divertor in AUG, with higher sensitivity to the divertor closure than λ_q. Conversely, recent L-mode experiments on TCV [39] showed that S_q is basically insensitive to variations of both I_P and $L_\parallel$. Also $S_q \propto 1/f_x$ which means that S_q^{tgt} stays constant when increasing flux flaring at the outer divertor target. These findings concur in suggesting that S_q, as discussed in section 2.3, is a true divertor quantity sensitive to local plasma conditions. Investigations were performed only on a limited number of devices and more work needs to be done to find common trends among different tokamaks, if any, and building a multi-machine scaling that could allow meaningful extrapolations to ITER. The current lack of understanding of the plasma parameters governing the spreading factor is somehow in contrast with the design of future reactors as DEMO [47] that rely sometimes on the assumption that S_q will be as big as several time λ_q: this is not routinely observed in tokamaks and therefore feels more like a feasibility requirement than a motivated design

assumption.

2.4.4 AUG scaling law for λ_{T_e} in H-mode

Upstream measurements of SOL profiles are available in a wide range of divertor conditions, even in partially detached and detached plasmas, which are beyond the capabilities of IR themorgraphy and therefore represent both a benchmark and a complementary tool. A comparison of SOL decay lengths from TS data in H-mode discharges in AUG with the IR λ_q scaling law (section 2.4.1) was recently carried out by Sun et al. [43]. This type of study requires assumptions on the link between λ_{T_e}, λ_{n_e} and λ_q. In the case of an attached divertor, simple relations are provided by two-point models [48]. In a strongly collisional plasma the heat flux is dominated by electron conduction: assuming classical transport and $T_e = T_i$, in the conduction-limited regime one can simply write:

$$\lambda_q = \frac{2}{7}\lambda_{T_e} \tag{2.29}$$

On the other hand, in a weakly collisional plasma, a convective component of the heat flux has to be taken into account. In the flux-limited regime, the link between decay lengths reads:

$$\frac{1}{\lambda_q} = \frac{1}{\lambda_{n_e}} + \frac{3}{2\lambda_{T_e}} \tag{2.30}$$

From the regression of T_e data collected with TS measurements in the main plasma of AUG during H-mode discharges, the following scaling law for λ_{T_e} is proposed:

$$\lambda_{T_e}^{\mathrm{AUG}} = (2.73 \pm 1.37) B_T^{-0.5\pm0.67} q_{cyl}^{0.97\pm0.17} P_h^{0.05\pm0.23} \tag{2.31}$$

highlighting weak dependence on the heating power and a direct dependence on q_{cyl} that hides $aR^{-1}B_T B_P^{-1}$. Comparison between λ_q values inferred from the measured λ_{T_e} using equations 2.29 and 2.30 are compared to λ_q predictions from [41], suggesting that the SOL of AUG is better described by the conduction-limited regime in these discharges. Moreover, the dependences of the presented λ_{T_e} scaling law agree with those of the above-mentioned λ_q scaling laws (both the AUG specific one and the multi-machine one) for what concerns B_P but, once again, a link with the inverse of the aspect ratio is highlighted. This result strengthens the idea that the SOL width might not be as geometry-independent as suggested by the multi-machine scaling law for λ_q.

Chapter 3

The divertor leg experiment in TCV

Contents

3.1 Context of the experiment

3.1.1 Motivation: testing assumptions

To understand whether λ_q is truly insensitive to the divertor magnetic geometry and try to find a scaling parameter for S_q are two separate goals that might be achieved within a single experiment. If it was possible to significantly change the size of the divertor while keeping all core plasma parameters constant, according to the idea that λ_q is a purely main SOL parameter and S_q a purely divertor one (section 2.3), one would expect not to see a variation of the former while the latter could effectively increase due to the bigger divertor volume. In other words such an experiment represents a benchmark for the assumptions of what is currently the most established model describing the heat flux profiles in diverted configurations [34]. Most of the tokamaks have limited flexibility in changing the magnetic equilibrium, being constrained by vessel and plasma shapes designed with the aim of maximising performance rather than exploring new geometries. An exception is represented by the *Tokamak à Configuration Variable* (TCV) [49], located at the Swiss Plasma Center (SPC) of the Ecole Polytechnique Fédérale de Lausanne (EPFL). With its elongated vacuum vessel surrounded by 16 independent poloidal field coils, TCV has unmatched shaping capabilities [16] making it a valuable candidate for this study. The device also benefits from a wide set of edge diagnostics (figure 3.1.a): main plasma conditions (n_e and T_e) in the core, edge and main SOL are monitored with an high resolution Thomson scattering (TS) [50] and a reciprocating Langmuir probe (RCP) plunging at the outer midplane [51]. Plasma conditions at the outer divertor target ($n_\mathrm{e}^\mathrm{tgt}$ and $T_\mathrm{e}^\mathrm{tgt}$) are assessed with wall-embedded Langmuir probes (LP) [52], while profiles of the outer target heat flux $q_\mathrm{surf}^\mathrm{tgt}$ are obtained via the infrared (IR) thermography system [39]. Measurements at the inner target are not discussed in this work for two main technical reasons: i) LP data coming from the inner column of TCV are considered unreliable for the magnetic geometries we investigate because of the grazing angle between field lines and the target which makes the calculation of the collection area of the probes extremely complex. In particular, for incidence angles smaller than 3°, one strongly overestimates n_e and therefore q^LP. ii) IR profiles of q_surf at the inner target are characterized by non-trivial shapes due to the presence of secondary peaks or, in some cases, to the reduced distance between the strike point and the gaps between the tiles. Further analyses are needed in order to interpret the inner target conditions which represent a necessary piece of the puzzle to obtain a global picture of the SOL in these equilibria. The rest of this chapter is organised as follows: section 3.1.2 describes the experimental strategy for scanning the outer divertor leg length in TCV while keeping the same upstream plasma

conditions, with an example of typical discharge for this study in section 3.1.3; results of the assessment of main plasma and outer divertor target conditions are presented in sections 3.2 and 3.3 respectively; findings from other recent and complementary heat load studies in TCV are finally summarized in section 3.4.

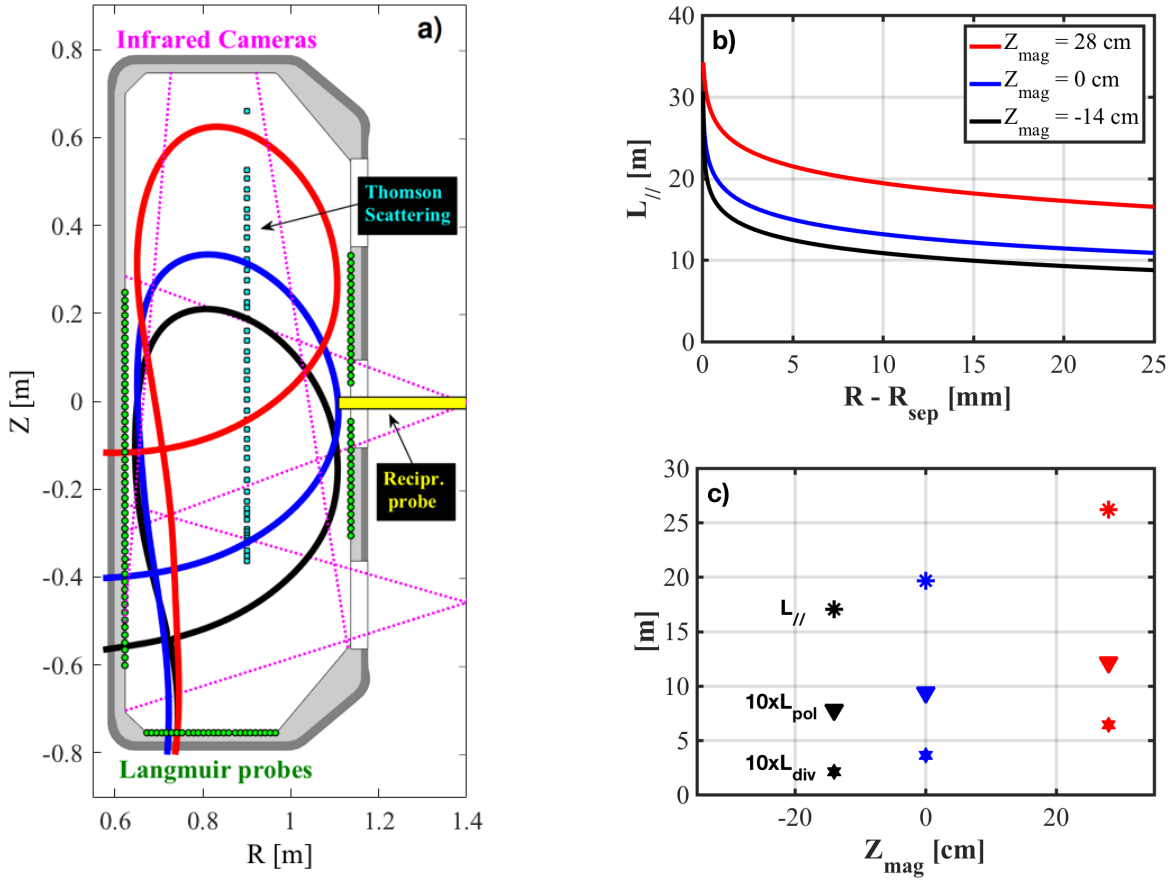

Figure 3.1: a) cross section of the TCV vacuum vessel with main diagnostics. Magnetic separatrix for short, medium and long outer divertor leg configurations in black, blue and red. b) Profiles of the SOL parallel connection length from outer midplane to outer divertor target. c) Parallel connection length (stars), poloidal connection length (triangles) and vertical X-point to target distance (hexagons) as a function of vertical position of magnetic axis.

3.1.2 Experimental strategy

A shot-to-shot scan of the vertical position of the magnetic axis (Z_{mag}) was performed in lower single null (LSN), Ohmic, L-mode, low density ($f_{\mathrm{GW}} = n/n_{\mathrm{GW}} \simeq 25-30\%$, where $n_{\mathrm{GW}} = I_{\mathrm{P}}/\pi a^2$ is the Greenwald density limit [53]), attached plasma discharges with fixed main plasma shape ($R_0 = 89$ cm, $a = 22$ cm, $k = 1.4$). Ohmic H-mode discharges are not considered in this work. Plasmas at vertical position $Z_{\mathrm{mag}} = -14$ cm, 0 cm and

28 cm, pictured in figure 3.1.a, were achieved at constant field at the magnetic axis of $B_0 = 1.4$ T, constant $I_P \simeq 210$ kA and therefore constant $B_P^{omp} \simeq 0.18$ T. Changing Z_{mag} leads to a variation of $L_\parallel$ from the outer midplane to the outer target, whose radial SOL profiles are shown in figure 3.1.b. The values of $L_\parallel$ (17 m, 19.6 m and 26.2 m respectively, averaged over a 5 mm distance from the magnetic separatrix), are displayed in figure 3.1.c, together with those of its projection on the poloidal plane, the poloidal connection length L_{pol} (0.77 m, 0.93 m and 1.21 m respectively). These three vertical plasma positions correspond to a divertor leg length L_{div} (vertical X-point to outer target distance) of 21 cm, 36 cm and 64 cm. In figure 3.1.c L_{div} is multiplied by a factor of 10 for readability reasons. Each of these quantities increases linearly with Z_{mag} and therefore they give an equivalent description. In the following L_{div} will be used and we will refer to these configurations also as *short*, *medium* and *long leg*, identified by the colors black, blue and red respectively. The main deliverable of the experiment is the assessment of the effect of L_{div} on the main plasma profiles and target profiles of n_e, T_e and q. All discharges used in this dataset are characterized by a variation of core line averaged density $n_{e,av}^{core}$ and of q_{95} within 10%.

3.1.3 A typical discharge

The typical discharge of this dataset lasts between 1.5 and 2 s. After the breakdown the plasma is initially limited at the HFS and the desired LSN configuration (figure 3.1.a) is achieved after $\simeq 400$ ms and is maintained for $\simeq 1$ s. During this time interval plasma parameters are kept as constant as possible. Figure 3.2 displays the time traces for a medium-leg discharge (#51333).

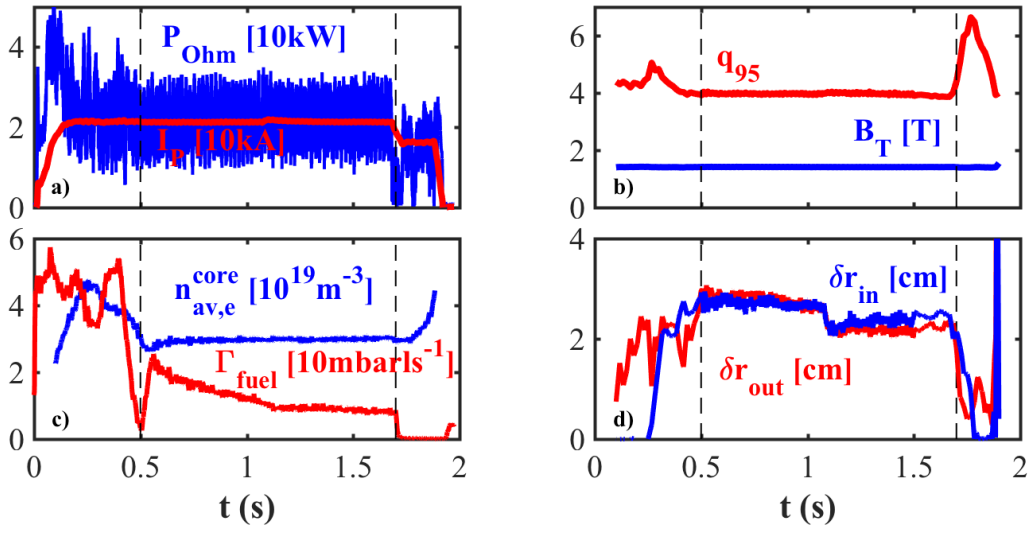

Figure 3.2: time traces of some of the plasma parameters during a typical discharge.

The plasma current ($\langle I_\mathrm{P}\rangle = 213$ kA, $\sigma_{I_\mathrm{P}} = 2.46$ kA) is constant and so is the average value of the Ohmic heating power $\langle P_\mathrm{Ohm}\rangle = 217$ kW (figure 3.2.a) while its fluctuations ($\sigma_{P_\mathrm{Ohm}} = 61.1$ kW) are linked to those of the loop potential which are of the order of 30%. Edge safety factor ($\langle q_{95}\rangle = 3.96$) and toroidal magnetic field ($\langle B_\mathrm{T}\rangle = 1.41$ T) have standard deviations of $\sigma_{q_{95}} = 0.05$ and $\sigma_{B_\mathrm{T}} = 0.002$ respectively (figure 3.2.b). The desired core average density ($n_\mathrm{e,av}^\mathrm{core} = 3 \times 10^{19}$ m^{-3}) is attained through feedback control by initially puffing fuel at a rate of > 20 mbar l s^{-1} which then stabilizes around 10 mbar l s^{-1} (figure 3.2.c). Since the main focus of this work are the SOL profiles, one has to make sure that the plasma volume doesn't fill the vacuum vessel in such way that the walls choke the SOL: a minimum 20 mm gap between the plasma and inner and outer (δr_in and δr_out respectively, evaluated at the midplane) was set as constraint (figure 3.2.d). For the outer divertor leg length (not shown) $\langle L_\mathrm{div}\rangle = 36.53$ cm and $\sigma_{L_\mathrm{div}} = 0.36$ cm. With respect to the position of the OSP, as shown on the left hand side of figure 3.3, the LSN portion of the discharge is divided in two phases. First there is a 500 ms *steady phase* in which the magnetic equilibrium is kept as still as possible and therefore the radial position of the outer strike point R_OSP (blue line) is constant. This helps measurement and statistics of IR thermography which works best with a steady signal. This is followed by a *sweep phase* of few hundreds of ms in which the outer divertor leg is moved across different LP. This procedure is necessary to improve the spatial coverage of time-integrated profiles, otherwise intrinsically limited by the distance between neighbouring probes, whose positions are indicated by the grey dash-dotted lines.

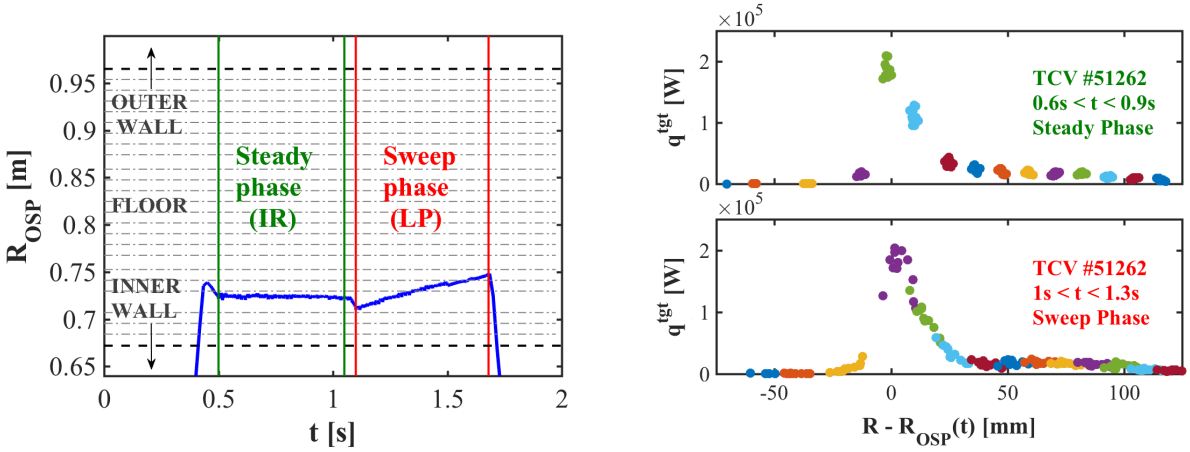

Figure 3.3: left) time trace of the OSP radial position along the TCV floor (blue solid line) with LP locations (grey dot-dashed lines); right) example of time-integrated LP profile without (top) and with (bottom) sweeping.

The reader might note that the line corresponding to one of the first probes close to the

inner wall is missing. Unfortunately this probe, whose location is the one where the OSP usually sits, did not acquire during this experiment. This fact reduces our capabilities of capturing the roll-over in the PFR of outer target profiles, making the evaluation of the spreading factor with the LP system a real challenge. The right hand side of figure 3.3 shows the difference in the LP signal of the outer divertor target heat flux during the steady (top) and sweeping (bottom) phases. The recovering of the points collected by neighbouring probes is essential to ensure that the peak of the profile is captured and doesn't fall in the gap between two probes, which would lead to an underestimation and and a poor quality of the fit to equation 2.19.

3.2 Main plasma conditions

3.2.1 Core and edge profiles

The assessment of plasma conditions in the core and edge region shows that, when changing L_{div} and therefore $L_{\parallel}$, there is no significant impact on n_{e} and T_{e}: radial profiles obtained via TS for short, medium and long divertor leg (black, blue and red triangles in figure 3.4 respectively) overlap nicely. These results suggest that the goal of matching main plasma parameters, while changing the divertor geometry, was achieved. Unfortu-

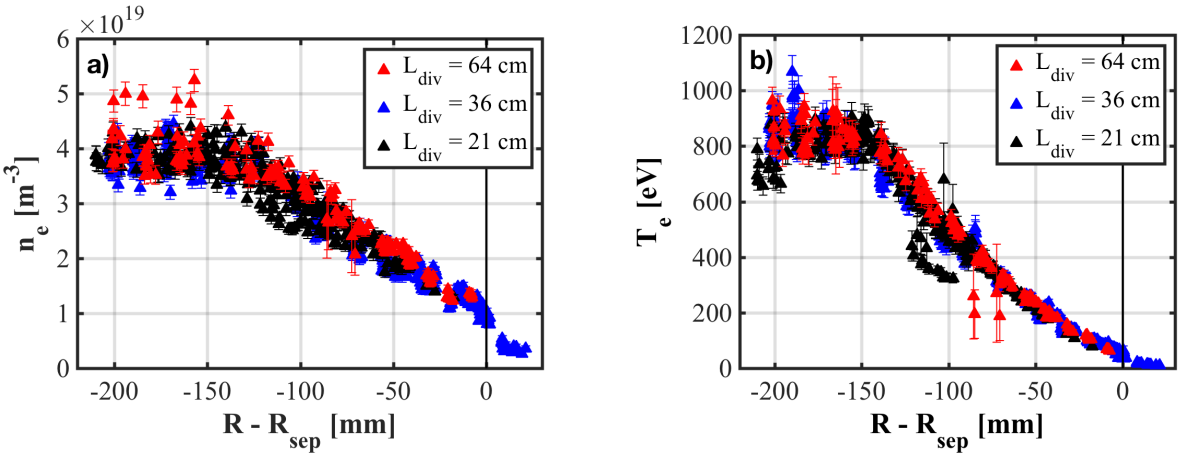

Figure 3.4: Thomson scattering, main plasma, profiles of a) n_{e} and b) T_{e} as a function of the radial distance from the outer midplane separatrix for L_{div} = 21 cm, 36 cm and 64 cm (black, blue and red triangles respectively).

nately, due to the reduced sensitivity of TS channels in the SOL region, experimental data in the main SOL are available only for plasmas with medium divertor leg, as can be seen in figure 3.5 which is a zoom-in of figure 3.4. Therefore, when trying to reconcile target to main SOL profiles for the different values of L_{div}, one has to take as working

assumption that, given the good match in the core and edge, n_e and T_e match also in the main SOL.

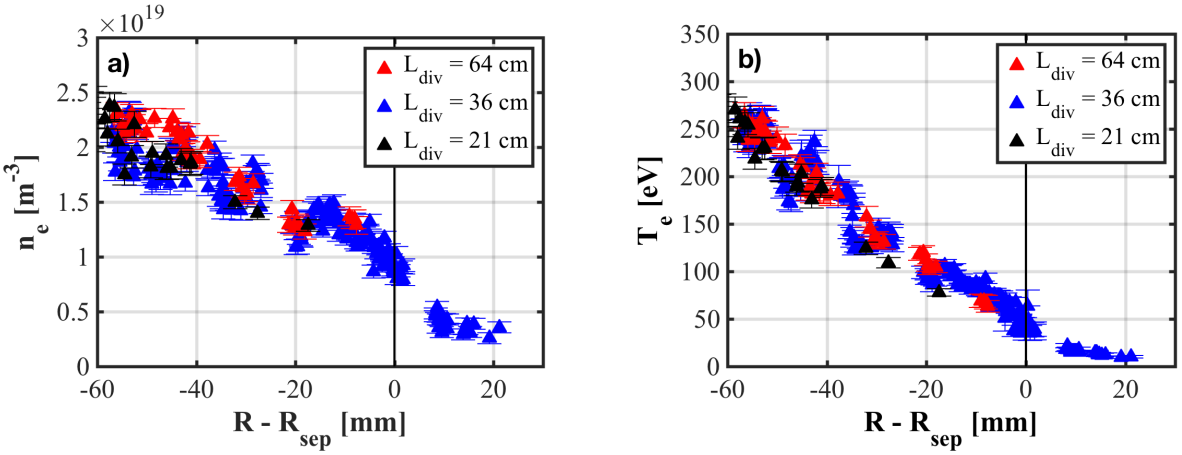

Figure 3.5: zoom-in of profiles shown in figure 3.4 to highlight the edge/SOL region.

3.2.2 Main SOL profiles

In figure 3.6.a and 3.6.b respectively, outer midplane measurements of n_e and T_e performed with a reciprocating double probe system [51] (RCP, green diamonds) are superimposed to target profiles from wall LP (blue dots) for the medium leg configuration. Outer midplane and target density profiles are in good agreement, suggesting no strong variation of n_e in terms of peak value nor of decay length along $L_\parallel$. On the other hand T_e drops on average by a factor of $\simeq 2$, indicating that the static pressure $P_e = n_e T_e$ is not conserved along the outer SOL. If one instead considers the total pressure $P_e^* = n_e T_e (1 + M^2)$ and assumes $M = 1$ ($v_\parallel = c_s$) near the target, according to the Bohm criterion, conservation is fulfilled: $P_e^{*,t} = 2 n_e^t T_e^t \simeq P_e^{*,u} = n_e^u T_e^u$. This result suggests that, at the outer target, the plasma is in attached condition.

3.2.3 Radiation and power balance

When changing the length of the outer divertor leg, the volume available for dissipative processes is modified. The radiated power P_{rad} in TCV can be estimated through bolometers: technical details about this diagnostic can be found in [54] and references therein. In figure 3.7.a we show he total radiated power (full diamonds), averaged over multiple shots in each configuration, as a function of L_{div}: $P_{rad}^{tot} = 7.25 \times 10^4$ W, 6.9×10^4 W and 9.46×10^4 W for $L_{div} = 21$ cm, 36 cm and 64 cm. These values correspond respectively to 34%, 30% and 40% of the total Ohmic power, which is the only source of heating

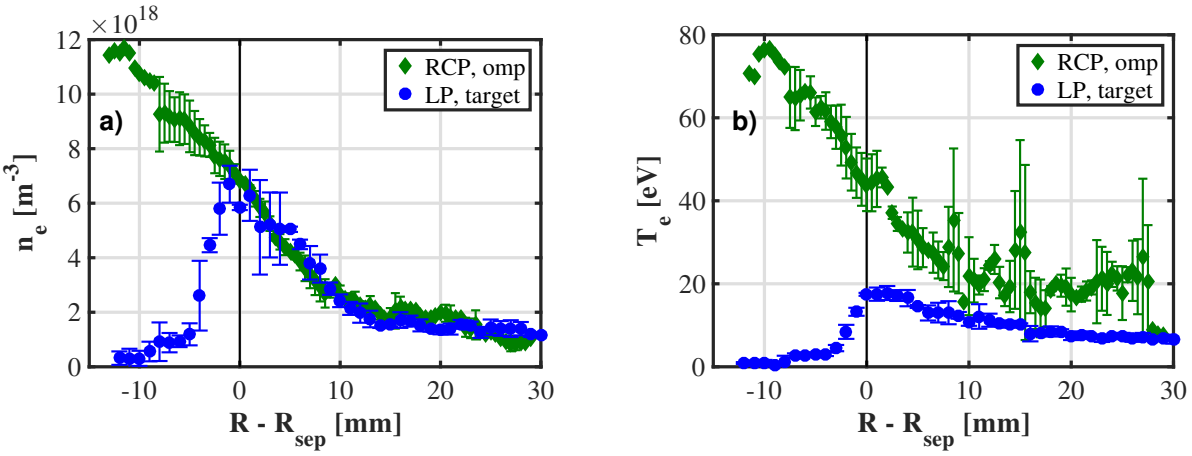

Figure 3.6: outer midplane, reciprocating Langmuir probe (green diamonds) and outer target Langmuir probes (blue circles) profiles of a) n_e and b) T_e as a function of the radial distance from the outer midplane separatrix for the medium divertor leg configuration.

and is matched within 10% in these discharges ($P_{\mathrm{Ohm}} = 2.13 \times 10^5$ W, 2.29×10^5 W, 2.34×10^5 W). Therefore, while short and medium leg plasmas have comparable $P_{\mathrm{rad}}^{\mathrm{tot}}$, in the long divertor leg configuration more power is dissipated through radiation. The average fractions of power radiated in the SOL, core and PFR (empty circles, squares and triangles in figure 3.7.a) suggest that the increase in $P_{\mathrm{rad}}^{\mathrm{tot}}$ is not due to a strong local increase somewhere but rather uniformly distributed over the entire magnetic equilibrium. Visual support to these speculations can be found in figure 3.7.b, where emissivity maps ($\mathrm{W\,m^{-3}}$) for one shot for each configuration are given as example: interestingly, despite the overall increase of $P_{\mathrm{rad}}^{\mathrm{tot}}$, it is possible to observe a reduction of the radiation close to the ISP with increasing L_{div}. Concerning the global power balance, the ratio $(P_{\mathrm{rad}}^{\mathrm{tot}} + P_{\mathrm{OSP}} + P_{\mathrm{ISP}})/P_{\mathrm{Ohm}}$ is equal to 79%, 75% and 69% respectively. These numbers are considered to be satisfactory for TCV, since the missing power is in line with the uncertainty related to the bolometric measurements.

3.3 Outer divertor plasma conditions

The wall Langmuir probes system (LP) for the outer divertor target consists in a single array of 26 cylindrical domed probes protruding by 1 mm, with a diameter of 4 mm and a spatial resolution of 11 mm [52]. The acquisition is sampled at 500 kHz and I-V characteristics are averaged over 50 ms, shorter than the frequency at which the magnetic strike point is swept across two neighbouring probes. A four parameters fit is performed on the I-V characteristics, to account for the sheath expansion in the saturation current branch [55, 56]. LP measurements show an effect of the divertor magnetic geometry on

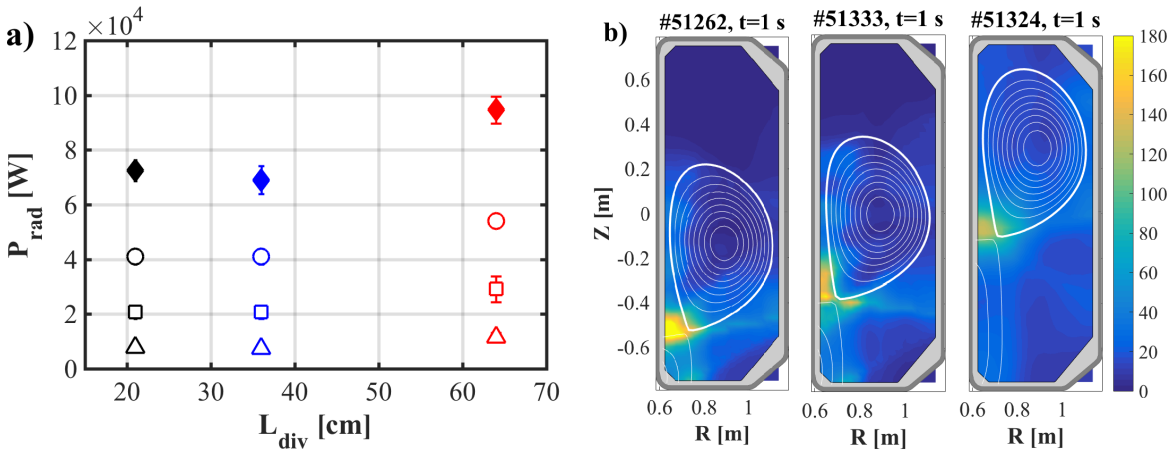

Figure 3.7: a) total radiated power (full diamonds), power radiated in the SOL (empty circles), in the core (empty squares) and in the private flux region (empty triangles), as a function of the length of the outer divertor leg; b) emissivity map ($\mathrm{W\,m^{-3}}$) of one shot for each configuration: short (51262), medium (51333) and long (51324) outer divertor leg. Measurements from bolometers.

n_e, T_e and q^{LP}: width, shape and amplitude of the outer target profiles change with the length of the outer divertor leg. For the sake of readability, profiles shown in figures 3.8.a, 3.9.a and 3.10.a are obtained binding data from three to four discharges repeated for the same value of L_{div} and in similar conditions: markers represent the average value of each dataset, error bars the corresponding standard deviation. Profiles of n_e, T_e and q^{LP} are plotted as a function of the radial distance from the magnetic separatrix ($R-R_{sep}$) at the outer midplane: it should be remembered that LP profiles are measured at the divertor target and then remapped at the outer midplane along magnetic flux (ψ) surfaces in order to allow the comparison of magnetic equilibria with different f_x. A least square fit to equation 2.19, represented by the solid lines, is performed to estimate the transport scale lengths (λ_y, S_y): here markers represent the value obtained by fitting the whole dataset for a given condition, without binding the data, while errorbars correspond to the accuracy of the fit.

3.3.1 Target electron density

Figure 3.8.a shows n_e profiles normalized to their maximum value to help visualizing shape variations. The information about the corresponding peak value is given in figure 3.8.b: $n_{e,max} = 5.2 \times 10^{18}$ $\mathrm{m^{-3}}$, 6.7×10^{18} $\mathrm{m^{-3}}$ and 6.1×10^{18} $\mathrm{m^{-3}}$ correspond to 18%, 23% and 21% of $n_{e,av}^{core}$ respectively, indicating similar core-to-target drop regardless of the divertor leg length. For the medium leg configuration, the value of $n_{e,max}$ is consistent with the one at the separatrix, n_e^{sep}, measured by the RCP at the outer midplane (green

diamond) meaning that no density drop occurs along the outer SOL. These results suggest that there isn't a strong effect of L_{div} on the density peak value. If one instead considers width and shape of the profiles, the impact of changing the divertor geometry is stronger: a monotonic trend of the density decay length λ_{n_e} with L_{div} (figure 3.8.c) is detected, with a factor of $\simeq 3$ increase over the explored range. The value of λ_{n_e} for the medium leg configuration is consistent, within errorbars, with the one measured by the RCP at the outer midplane (green diamond). The density spreading factor S_{n_e} (figure 3.8.d) shows no trend with L_{div}, with values in the range from $\simeq 2.5$ mm to $\simeq 4.5$ mm. Interestingly the main SOL transport scale length λ_{n_e} has a stronger relative variation than the divertor one S_{n_e}, when increasing the outer divertor leg length. It should be noted that n_e profiles for the short and medium leg configurations exhibit an asymmetric background, which is non null in the far CFR. These *shoulders*, unlike the density-dependent ones observed for instance in [57, 58], correspond to positions on the outer divertor target that are not seamlessly connected to the inner divertor target since magnetic field lines intercept the vacuum vessel either at the top of the machine or at the outer wall. For this reason, such locations are not taken into account in the fitting procedure, which was performed up to $R - R_{\mathrm{sep}} = 10$ mm and 15 mm for short and medium leg, respectively.

3.3.2 Target electron temperature

Figure 3.9.a shows the corresponding normalized target T_e profiles. Unlike density, T_e exhibits a clear drop in peak value and a less marked broadening of profiles (at least in the CFR) with increasing L_{div}. In fact, the peak value $T_{\mathrm{e,max}}$ (figure 3.9.b) is reduced by a factor of $\simeq 2$ with L_{div}, from $\simeq 20.3$ eV to $\simeq 11.2$ eV. The value for the medium leg configuration ($\simeq 17.8$ eV) corresponds to 40% of $T_\mathrm{e}^{\mathrm{sep}}$ measured by the RCP at the outer midplane (green diamond) indicating a T_e drop along the SOL. The target temperature decay length λ_{T_e}, whose values are in the range 20 to 35 mm, is not straightforwardly affected by L_{div}, as no trend stands out of the error bars (figure 3.9.c). The value of λ_{T_e} for the medium leg configuration is $\simeq 1.7$ times bigger than the one measured by the RCP at the outer midplane (green diamond), suggesting a broadening of T_e profiles along the outer SOL. Unlike λ_{T_e}, the temperature spreading factor S_{T_e} changes monotonically with L_{div} (figure 3.9.d), with a factor of $\simeq 2$ to $\simeq 5$ increase between short and long leg configurations, within the big error bar of the latter. This would mean that, for temperature, a very long divertor leg has a stronger effect on the divertor transport scale length than on the main SOL one.

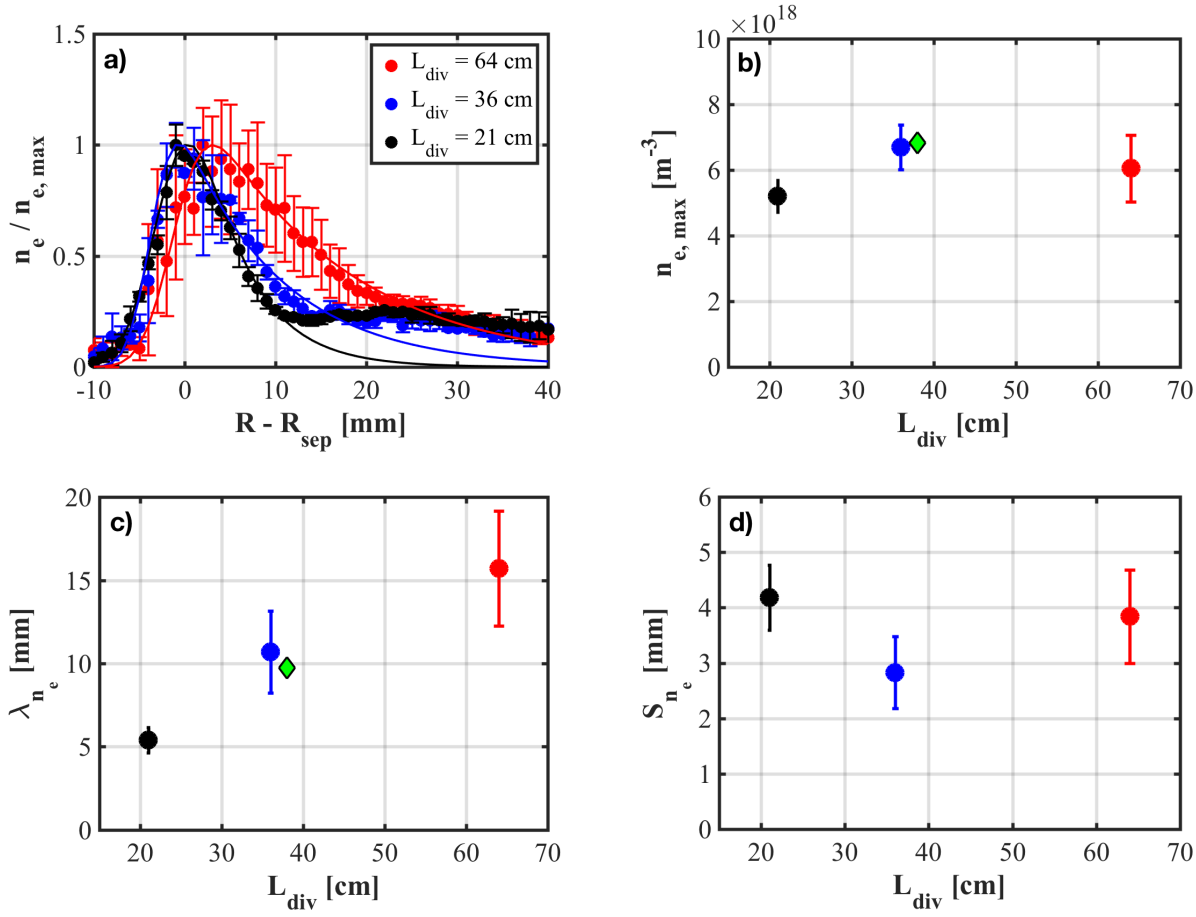

Figure 3.8: a) normalized outer target Langmuir probes profiles of n_e as a function of radial distance from the outer midplane separatrix for short, medium and long outer divertor leg configurations in black, blue and red. Density b) peak value, c) decay length and d) spreading factor as a function of outer divertor leg length. Green diamonds for outer midplane reciprocating Langmuir probe data.

3.3.3 Target heat flux

Finally the corresponding q^{LP} profiles are shown in figure 3.10.a, where a clear broadening with L_{div} can be detected. With $q^{\mathrm{LP}}_{\mathrm{max}} = 184.8\ \mathrm{kW\,m^{-2}}$, $260.4\ \mathrm{kW\,m^{-2}}$ and $87.4\ \mathrm{kW\,m^{-2}}$ respectively, a factor of $\simeq 2$ drop in peak heat flux between short and long leg configurations is measured (figure 3.10.b). These values correspond to $\simeq 60\%$ of $q^{\mathrm{IR}}_{\mathrm{max}}$ (empty squares) [39], which represents the peak of the heat flux absorbed by the target material surface, therefore independent of any assumption regarding $T_{\mathrm{i}}/T_{\mathrm{e}}$. Conversely, as described in section 2.2.1, $q^{\mathrm{LP}} = en_{\mathrm{e}}c_{\mathrm{s}}\left(\gamma T_{\mathrm{e}} + E_{\mathrm{pot}}\right)$ was calculated here assuming cold ions ($\gamma = 5$), which is the usual hypothesis made for TCV [16]. The presence of a systematic $60\% \simeq 5/8$ differences in peak heat flux suggests that assuming hot ions ($\gamma = 8$) gives a better description of these plasmas, reconciling the results from the two diagnostics.

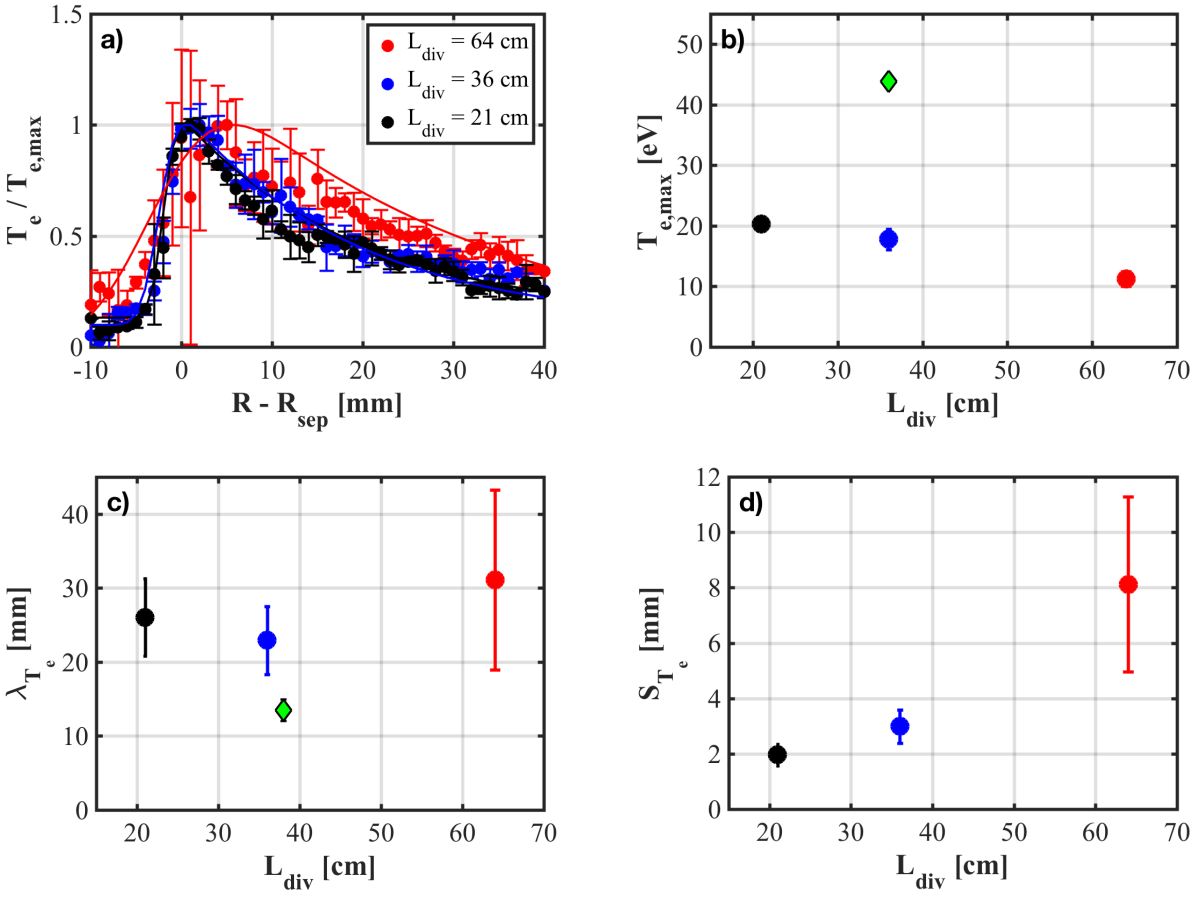

Figure 3.9: a) normalized outer target Langmuir probes profiles of T_e as a function of radial distance from the outer midplane separatrix for short, medium and long outer divertor leg configurations in black, blue and red. Temperature b) peak value, c) decay length and d) spreading factor as a function of outer divertor leg length. Green diamonds for outer midplane reciprocating Langmuir probe data.

The heat flux decay length λ_q^{LP} (figure 3.10.c) undergoes a factor of $\simeq 2$ increase with L_{div} which is consistent with λ_q^{IR} (empty squares). The value of λ_q^{RCP} measured at the outer midplane (green diamond) is in quantitative agreement with λ_q^{IR} and matches, within error bars, with λ_q^{LP}. This result suggests that, if a broadening of the q profile occurs along the outer SOL, it is moderate for this configuration. For the heat flux spreading factor S_q^{LP} instead, as well as for S_q^{IR} (empty squares), no trend can be detected within the sensibility of the diagnostics (figure 3.10.d). Here values are in the range of 2 to 3 mm and, especially for the long leg configuration, error bars are comparatively big. To summarize, according to LP measurement, a longer divertor leg causes the broadening of q^{LP} profiles and the corresponding drop of $q_{\mathrm{max}}^{\mathrm{LP}}$. Both findings are in agreement with IR data. Interestingly, as observed for n_e profiles, both diagnostics highlight a stronger variation of the main SOL transport scale length λ_q compared to the divertor one S_q

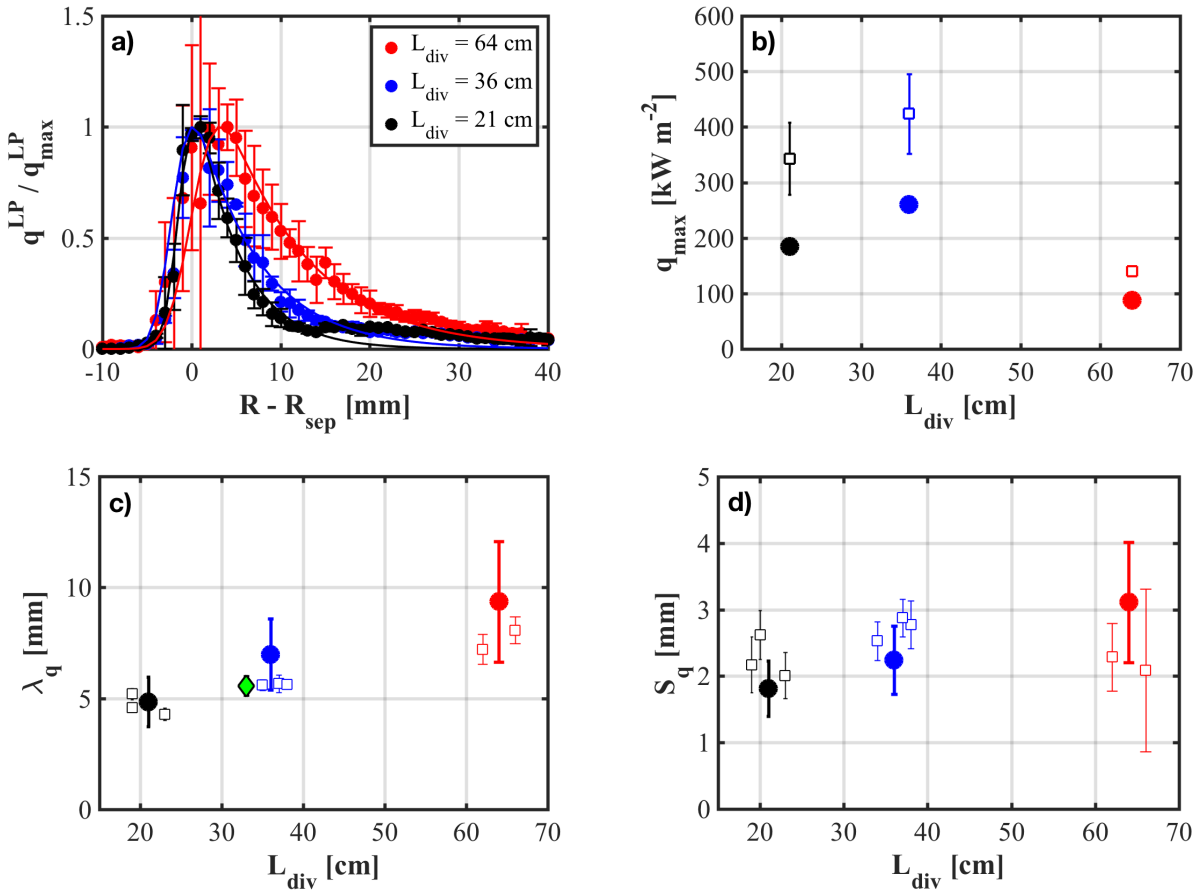

Figure 3.10: a) normalized outer target heat flux profiles (LP) as a function of radial distance from the outer midplane separatrix for short, medium and long outer divertor leg configurations in black, blue and red. Heat flux b) peak value, c) decay length and d) spreading factor as a function of outer divertor leg length. Empty squares for target infrared data and green diamond for outer midplane reciprocating probe data.

when modifying the divertor geometry.

3.4 Other recent TCV findings

3.4.1 Plasma current scan

Since TCV is not included in the multi-machine study in which $B_{\mathrm{P,omp}}$ was found to be the dominant dependence for λ_q, recent experiments aimed at checking whether this trend is followed by TCV as well. As shown by Maurizio et al. [39], an inverse dependence was found for λ_q at the outer divertor target when scanning I_{P} (and therefore $B_{\mathrm{P,omp}}$) during L-mode discharges with constant $k = 1.58$, $a = 22.5$ cm, $L_{\mathrm{div}} = 36$ cm and $f_{\mathrm{x}} = 2.5$. Density is changed in order to keep a constant $f_{\mathrm{GW}} = 0.25$ during the I_{P} scan. Figure

3.11.a shows a power law fit (blue line) to IR data (blue squares) highlighting the trend $\lambda_q^{\mathrm{IR}} \propto I_{\mathrm{P}}^{-0.69}$, which is in qualitative agreement with other devices [41, 35]. A similar trend

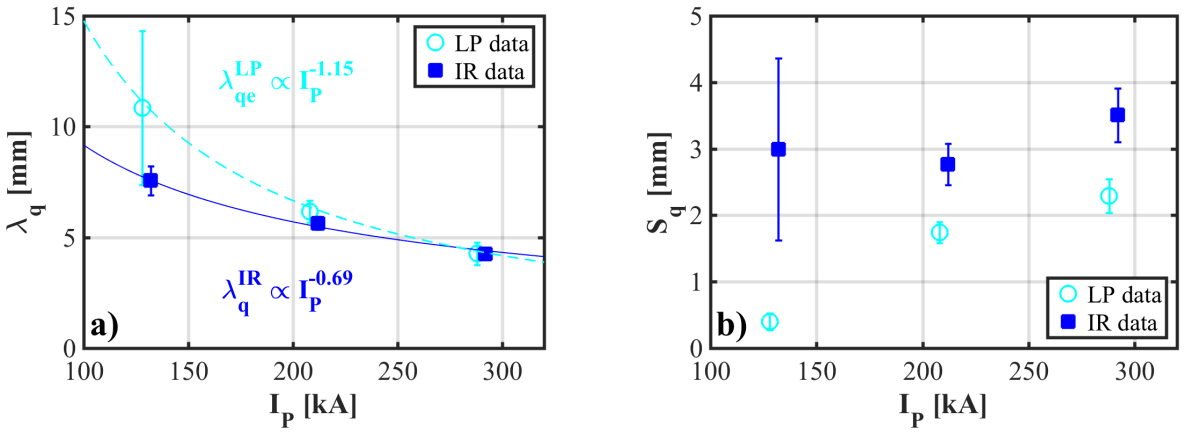

Figure 3.11: heat flux a) decay length and b) spreading factor function of plasma current.

is found by fitting (cyan dashed line) the heat flux decay length from LP measurements (cyan circles): $\lambda_q^{\mathrm{LP}} \propto I_{\mathrm{P}}^{-1.15}$. The difference in the exponent is most probably due to the big uncertainty on λ_q^{LP} at $I_{\mathrm{P}} = 130$ kA for which LP data are available for one sole shot, whose fit has a poor quality, while the agreement between IR and LP is good for $I_{\mathrm{P}} = 210$ kA and 290 kA. As for the outer divertor leg length scan, no clear trend emerges from S_q data, shown in figure 3.11.b with the same color code for IR and and LP: S_q appears to be again a rather insensitive quantity, constantly in the range of $2-4$ mm for IR and slightly lower for LP. As for λ_q^{LP}, at $I_{\mathrm{P}} = 130$ kA measurements are less reliable with an estimated $S_q^{\mathrm{LP}} = 0.4$ mm certainly due to poor fit accuracy. The attentive reader might also notice that the value of S_q^{LP} at 210 kA in figure 3.11.b differs from the one at $L_{\mathrm{div}} = 36$ cm shown in figure 3.10.d: this is because the values come from two datasets corresponding to different shots obtained in similar conditions. This is a further proof of how challenging it is to estimate decay lengths of heat flux profiles from LP measurements: this is particularly true for the spreading factor, not only for the limited resolution of this diagnostic even in the presence of strike point sweeping, but because of the much steeper slope of the profiles around the strike point position where the roll-over in the PRF is to be captured compared to the CFR side where λ_q dominates the profile. Interestingly, these L-mode λ_q values measured in TCV are $\simeq 2$ times bigger than the predictions of the scaling law obtained from JET and AUG L-mode discharges [40]. This result suggests that equation 2.25 is not suitable for describing the heat flux decay lengths in TCV and that, therefore, its validity might be limited to JET and AUG. Predictions from the HD model, discussed in section 2.1.2, give a better description on the TCV

L-mode plasmas with λ_q = 7 mm, 4.3 mm and 3 mm for I_P =130 kA, 210 kA and 290 kA respectively: despite being only qualitative, this agreement is quite impressive if one considers how far we are from the assumtpions of the HD model (H-mode, no turbulence) in these L-mode discharges, in which an important role seems to be played by turbulence, as discussed in section 4.4.4. On the other hand, if one compares the L-mode λ_q in TCV with the multi-machine scaling laws from H-mode discharges [20] presented in section 2.4.1, a good match in terms of both trend and amplitude is found, as shown by the cyan full stars in figure 3.12. This result, for which an explanation is yet to be found, sets TCV apart from most other machines. Moreover, considering that on JET and AUG it was found $\lambda_q^{\text{L-mode}} \simeq 2\,\lambda_q^{\text{H-mode}}$ [40] (section 2.4.2), one might wonder whether such thumb rule is respected on TCV, leading to a H-mode heat flux decay length two times thinner than the one predicted by scaling laws, as represented by the cyan empty stars in figure 3.12. The first heat load studies during H-mode discharges in TCV are one of the topics of this years experimental campaign and are currently being carried out. Preliminary analysis of IR data seem to suggest that the inter-ELM λ_q is a factor of $\simeq 2-3$ times lower than what the H-mode scaling law would predict [59].

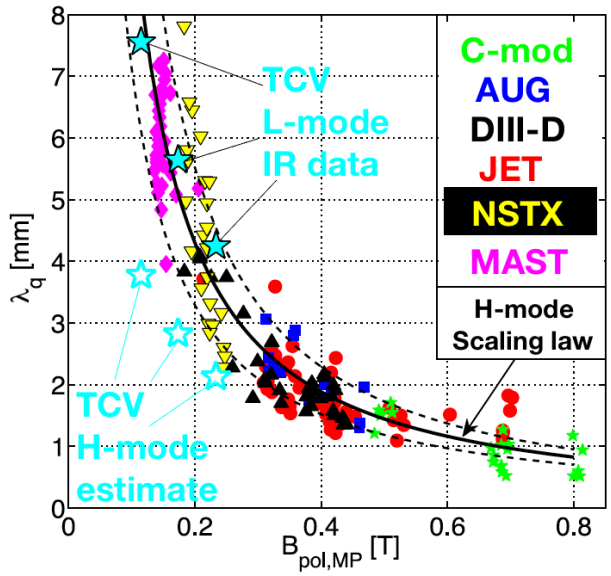

Figure 3.12: TCV L-mode λ_q values from IR (full cyan stars) compared to the H-mode multi-machine scaling law (overplot on figure 3 from reference [20]). Empty cyan stars represent TCV estimated H-mode values according to the thumb rule in [40].

It is important to remember that none of these scaling laws is capable of capturing the strong effect of the divertor magnetic geometry on λ_q highlighted by the divertor leg length scan and discussed in section 3.3: in fact, in such experiment a factor of $\simeq 2$ increase in λ_q was observed without changing any of the engineering parameters governing the existing scaling laws.

3.4.2 Upper triangularity scan

Another recent experimental investigation of the effect of the plasma geometry on the divertor heat load consisted in a scan of the upper triangularity δ_{up} in low-density, attached, Ohmically heated L-mode discharges [60]. The peculiarity of this experiment is that, thanks to the plasma shaping capabilities of TCV, also negative values of δ_{up} were achieved, as shown by the magnetic equilibria depicted in figure 3.13.a. While varying δ_{up} the magnetic equilibrium is modified in such a way that the divertor geometry is unchanged: the connection length between the outer midplane and the outer divertor target is the same for all the equilibria, as shown in figure 3.13.b, and the one between outer midplane and inner target varies within 30% because of the reduced distance between the active (lower) and non-active (upper) X-points at negative triangularities, as can be seen in figure 3.13.c.

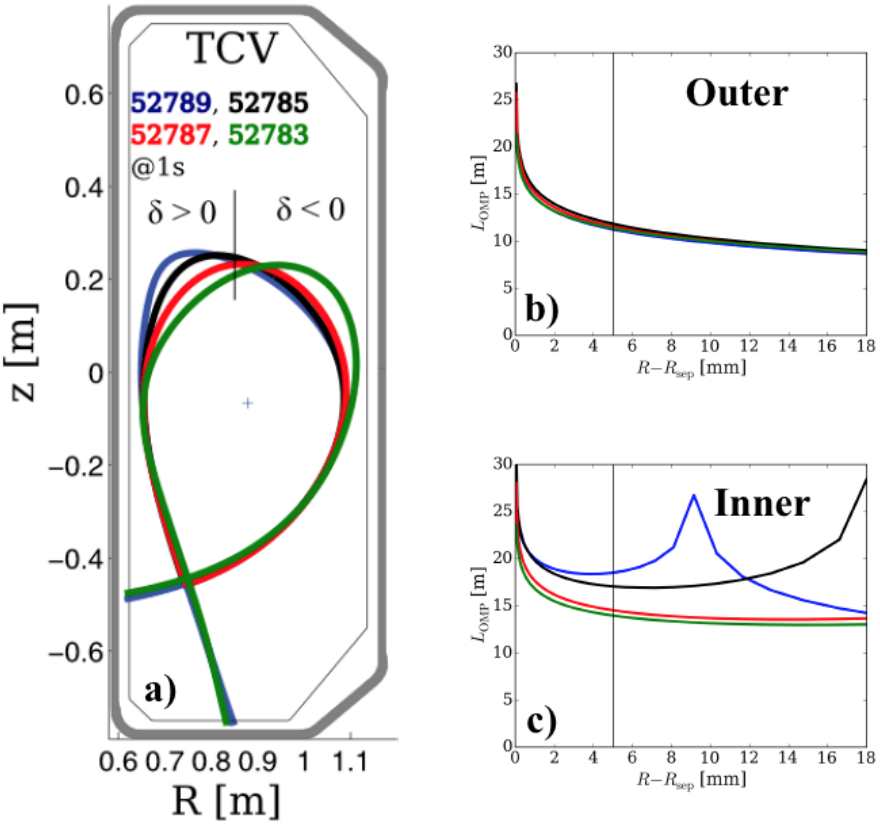

Figure 3.13: a) poloidal cross section and radial profiles of connection length from the outer midplane to d) the outer target and c) to the inner target for different values of the upper triangularity. Taken from figure 1 in [60].

For decreasing values of δ_{up} a smaller λ_q^{out} is estimated from IR measurement at the outer divertor target (figure 3.14.a) together with a higher edge electron temperature $T_{e,edge}$ assessed with TS (figure 3.14.b), symptoms of a narrower heat flux width and of a better

energy confinement. This effect is observed for both toroidal magnetic field directions, labelled in figure 3.14 as *favvorable* (vertical drifts directed towards the X-point) and *non-favorable* (vertical drifts directed away from the X-point), as well as in both Deuterium (black markers) and Helium (red markers) discharges, with higher values of λ_q^{out} in Helium. This variation of the heat flux decay length, which corresponds to a factor of $\simeq 4$ span if one considers the whole database, is observe at constant $B_{\text{P,omp}}$, as for the divertor leg length experiment. The corresponding variation of $T_{\text{e,edge}}$ is of the order of $\simeq 50\%$ over the whole dataset. On the other hand a non-monotonic trend of λ_q^{in} with δ_{up} is observed.

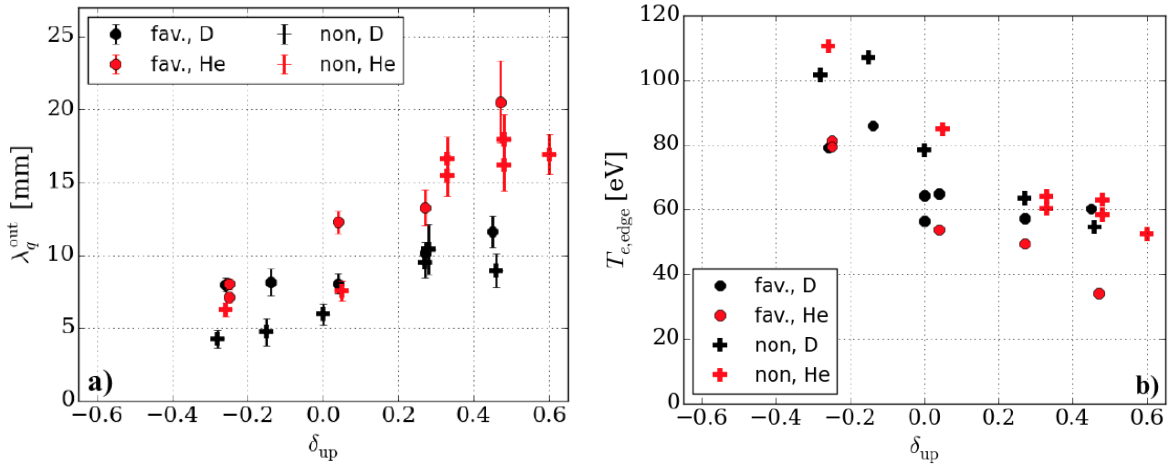

Figure 3.14: a) heat flux decay length at the outer divertor target and b) edge electron temperature as a function of the upper triangularity. Taken from figures 9 and 4 in [60].

As recalled by M. Faitsch et al. [61], the HD model presented in section 2.1.2 predicts the following effect of the triangularity on the ratio of the heat flux decay lengths at the two divertor targets:

$$\frac{\lambda_q^{\text{in}}}{\lambda_q^{\text{out}}} = \frac{1 - d_{\text{up}}}{1 + d_{\text{up}}} \tag{3.1}$$

Figure 3.15 shows the ratio $\lambda_q^{\text{in}}/\lambda_q^{\text{out}}$ as a function of $(1 - d_{\text{up}}) / (1 + d_{\text{up}})$ for our experimental dataset. The TCV measurements are found to follow the theoretical trend, indicated by the black solid line, for positive values of δ_{up} (left hand side of the viewgraph) while the ratio flattens out around $\lambda_q^{\text{in}}/\lambda_q^{\text{out}} \simeq 0.7$ for negative values of δ_{up} (right hand side). This result, together with no clear variation of the absolute values of either λ_q^{out} or λ_q^{in} with the toroidal field direction, suggests that vertical drifts are not the dominant mechanism setting the heat flux decay length in these discharges. Moreover, the increase in $T_{\text{e,edge}}$ and the improved confinement would be consistent with a reduction of radial heat turbulent transport in the core plasma region at negative triangularity, as discussed

in [62, 63, 64]. The results of this study, which is complementary to the divertor leg experiment discussed above, give further proof of the importance of the magnetic geometry as a player of both core and SOL transport, as well as of the primary role of turbulence in setting the heat flux width, at least in L-mode discharges.

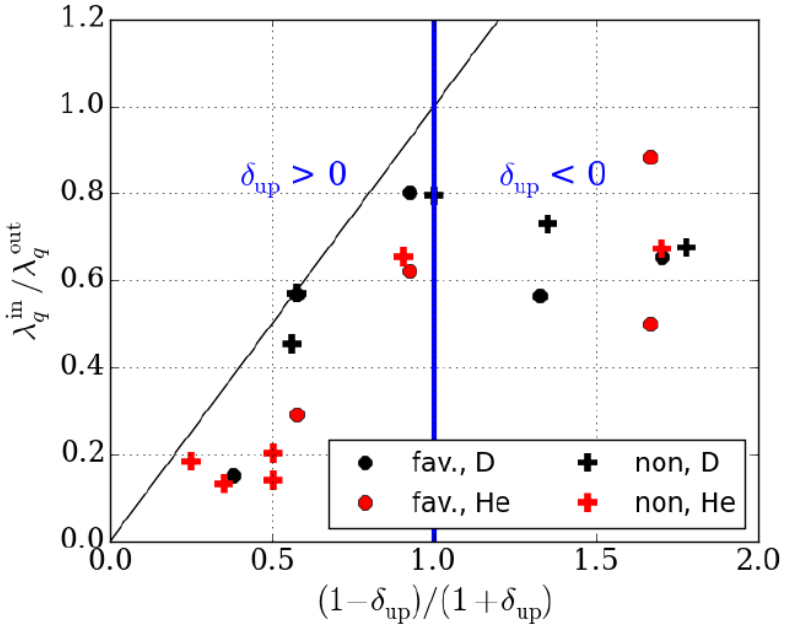

Figure 3.15: ratio of the experimental heat flux decay lengths in TCV compared to the prediction of the HD model on the role of triangularity. Taken from figure 16 in [60].

Chapter 4

Modelling of SOL transport and widths

Contents

4.1 Diffusive Monte Carlo modelling: MONALISA

4.1.1 The MONALISA code

A simple approach to the modelling of SOL transport and widths is to assume that the plasma travels mainly in the parallel direction while undergoing diffusion in the perpendicular one. These are the basic assumptions of MONALISA [37], a Monte Carlo code for the simulation of SOL energy transport and target heat flux profiles in realistic tokamak geometry under simplified physics. MONALISA is based on experimental ψ maps from equilibrium reconstruction codes (e.g. EFIT or LIUQE) and realistic tokamak wall contours. *Energy packets* are generated at a point-like source located in the confined plasma with a temperature T and then freely stream along field lines at constant thermal velocity of either $v_{\parallel} = +c_{\mathrm{s}}$ or $v_{\parallel} = -c_{\mathrm{s}}$. We therefore work with two populations flowing in opposite direction, at the same speed. While doing so, they undergo homogeneous diffusion in the $\perp$ direction (modelled with a transport coefficient $D_{\perp}$, constant over the entire plasma volume), eventually crossing the separatrix and following open field lines until the machine wall. Full curvature (grad$B$ and curv$B$) drifts, as well as $E \times B$ drifts (based on an ad hoc electrostatic potential map [65]), can be added to the system. Packet positions are iterated following both free streaming and drifts velocities on the ψ map using a predictor corrector scheme (order ≥ 2). When a heat packet strikes the wall, its kinetic properties ($E_{\parallel}$, $E_{\perp}$) are locally stored. By repeating the process for a high number of heat packets ($10^4 - 10^6$) in a Monte Carlo fashion and by performing local fluid interpolation on the whole wall contour, it is possible to reproduce target heat flux profiles whose shape is qualitatively consistent with those observed in experiments. It should be noted that the results do not depend on the position of the source, provided that it is far enough inside the separatrix to ensure that heat packets are poloidally uniformly distributed before entering the SOL. The strong points of MONALISA are its flexibility and quickness: since there is no need of a grid aligned to ψ surfaces, the code is ready to simulate any magnetic configuration (limiter, single or double null, snowflake, etc.) for any device once ψ map and wall geometry are given; it is also a fast "particle" tracer and therefore the simulation time ranges from few minutes to few hours, depending on the machine size and on the value of $D_{\perp}$. These features allow fast scans of control parameters such as I_{P}, $T\left(v_{\parallel}, v_{\mathrm{curv}B}\right)$, $D_{\perp}$ and B_{T}, as well as the tuning of drifts. Here is an example of the typical MONALISA output: in figure 4.1 we superimpose $q_{\parallel}$ profiles (empty circles) for three simulations based on the same magnetic equilibrium (TCV #51262, $t = 800$ ms, black curve in figure 3.1). Plasma parameters are the same ($T = 40$ eV, $I_{\mathrm{P}} = 210$ kA, $B_{\mathrm{T}} = 1.4$ T) but transport parameters differ with the following color

code: blue for $D_\perp = 1\ \mathrm{m^2\,s^{-1}}$ and no drifts, red for $D_\perp = 1\ \mathrm{m^2\,s^{-1}}$ and vertical drifts, green for $D_\perp = 4\ \mathrm{m^2\,s^{-1}}$ and no drifts. Solid lines represent the fit to equation 2.19. The fit accuracy for these simulations is $\geq 95\%$.

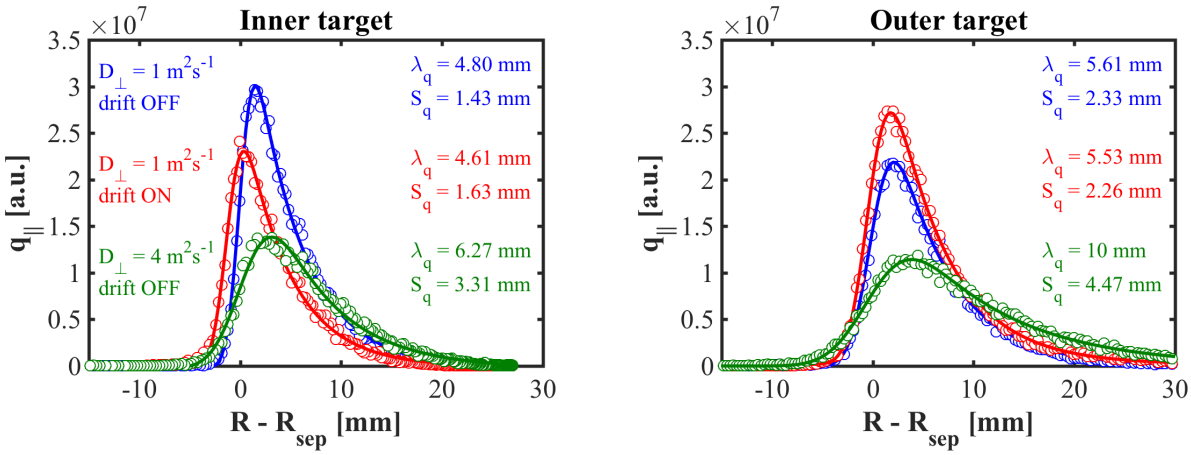

Figure 4.1: MONALISA $q_\parallel$ profiles based on the magnetic equilibrium of TCV #51262 ($t = 800$ ms) with same T, I_P, B_T but different transport (blue for $D_\perp = 1\ \mathrm{m^2\,s^{-1}}$ and no drifts, red for $D_\perp = 1\ \mathrm{m^2\,s^{-1}}$ and vertical drifts, green for $D_\perp = 4\ \mathrm{m^2\,s^{-1}}$ and no drifts).

With respect to the reference case (blue), the addition of vertical magnetic drifts (red) impacts the inboard–outboard asymmetry, transferring power from the inner to the outer target ($P_\mathrm{IN}/P_\mathrm{OUT}$ changes from 0.83 to 0.51) and reversing the position of $q_\parallel^{max}$, while the width of the profiles is basically unchanged. The reader might also notice that vertical drifts cause a noticable shift of the profile at the inner target, where the divertor leg is basically horizontal, while no shift occurs at the outertarget, where the divertor leg is vertical and therefore aligned with the drifts. On the other hand, a stronger diffusion coefficient (green) results in broader profiles, with lower $q_\parallel^\mathrm{max}$ at both strike points and therefore larger λ_q and S_q. MONALSIA profiles fit nicely to equation 2.19, which is not surprising since the underlying model is also based on diffusion [33]. Moreover, $S_q/\lambda_q \simeq 40\%$ as found in the multi-machine database [20]: even though, in general, this ratio is not fixed due to the different scaling laws followed by λ_q and S_q , the agreement with a wide experimental database suggests that the asymmetry of numerical profiles is reasonable. It has to be clarified that MONALISA should not be considered as an alternative to more complex edge codes but rather as a faster and lighter complementary tool to check simple assumptions, disentangle the effect of transport mechanisms and explore different (or new) configurations. Even though the physics included in the code is fairly simple compared to the complexity of experimental reality, making any attempt of quantitative estimate of $q_\parallel^\mathrm{max}$ fruitless, it is worth taking advantage of the wide variety of devices and magnetic geometries that MONALISA can tackle in order to address the

effect of plasma geometry on λ_q and S_q .

4.1.2 Multi-machine numerical database and comparison with the approximation of a purely diffusive cylindrical plasma

Taking full advantage of the speed and flexibility of MONALISA in handling different plasma geometries, a database of magnetic equilibria from AUG, TCV, WEST, JET and COMPASS was explored, covering a wide range of plasma shapes and sizes ($k = 1.46 - 1.78$, $q_{\mathrm{cyl}} = 1 - 10$, $\delta_{\mathrm{up}} = 0.08 - 0.37$, $\delta_{\mathrm{down}} = 0.28 - 0.79$). This includes also the three equilibria of the TCV divertor leg experiment. Several simulations were run for each equilibrium making a semi-random scan of the main control parameters (T, I_{P}, B_{T}, $D_{\perp}$) around their reference values in order to mimic the scatter of conditions typical of a real experimental database. It should be noted that ψ maps were linearly scanned when changing I_{P}, neglecting variations of the Shafranov shift. For the sake of simplicity, drifts were turned off in this study. Numerical OSP heat flux profiles were then fitted with equation 2.19 in order to extract λ_q and S_q. With the aim of checking whether, under the assumptions of the model, λ_q is truly a divertor-insensitive quantity once profiles are remapped at the outer midplane, it is worth comparing MONALISA values with those theoretically predicted for a *purely diffusive cylindrical plasma*. As discussed in section 2.1.1, by equating the time needed to diffuse across a width λ_q with the time needed to flow along a field line at speed $v_{\parallel} = c_{\mathrm{s}}$, the following expression is obtained:

$$\lambda_q^{\mathrm{Theo}} = \sqrt{D_{\perp}\frac{L_{\mathrm{cyl}}}{c_{\mathrm{s}}}} = \sqrt{D_{\perp}\frac{\pi R q_{\mathrm{cyl}}}{c_{\mathrm{s}}}} \tag{4.1}$$

where $L_{\mathrm{cyl}} = \pi R q_{\mathrm{cyl}}$ is the cylindrical connection length, is used a proxy for $L_{\parallel}$. We recall that $q_{\mathrm{cyl}} = \frac{a}{R}\frac{B_{\mathrm{T}}}{B_{\mathrm{P}}}\sqrt{\frac{(k+1)^2}{2}}$ is the cylindrical safety factor (which nothing has to do with q in the sense of the heat flux), accounting for different sections and shape of the cylinder through a and k. Comparison is made in figure 4.2, where numerical values ($\lambda_q^{\mathrm{MONA}}$) are plotted against $\lambda_q^{\mathrm{Theo}}$ calculated for the corresponding magnetic equilibria, $D_{\perp}$ and c_{s} values of the simulations. For the entire database points fall on the same straight line meaning that, regardless the device and the magnetic equilibrium, $\lambda_q^{\mathrm{MONA}}$ is always a constant fraction ($85\% \pm 10\%$) of $\lambda_q^{\mathrm{Theo}}$, within Monte Carlo fluctuations. This result proves that, when it comes to λ_q, the rough approximation of a cylindrical plasma shape (no X-point) is a good proxy for MONALISA (full magnetic geometry): once $q_{\parallel}$ profiles are remapped at the outer midplane, all equilibria behave in the same way, leading to the conclusion that $\lambda_q^{\mathrm{MONA}}$ depends on transport and general geometrical parameters (a, R, k) but it is independent of the divertor geometry.

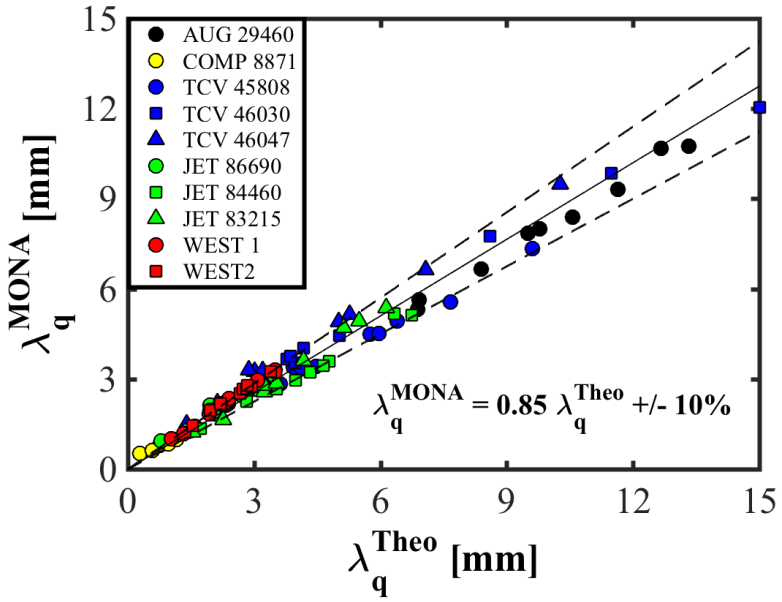

Figure 4.2: multi-machine database of the decay length of MONALISA numerical profiles ($\lambda_q^{\mathrm{MONA}}$) as a function of the prediction for a purely diffusive cylindrical plasma ($\lambda_q^{\mathrm{Theo}}$).

4.1.3 The role of flux expansion and "effective" connection length

The results discussed in section 4.1.2 are in clear contradiction with the TCV experimental findings presented in chapter 3, suggesting that a crude model based on parallel free streaming and perpendicular diffusion fails in representing the physics at play in the divertor leg length scan. In order to find an explanation to the insensitivity of $\lambda_q^{\mathrm{MONA}}$ to the divertor geometry, one might want to consider two TCV equilibria with different outer divertor leg length (figure 4.3.a) and a factor of ~ 2 difference in $L_{\parallel}$ (midplane-to-target connection length), despite having the same L_{cyl} (cylindrical plasma without legs). Assuming the above-mentioned dependence $\lambda_q \propto \sqrt{L_{\parallel}}$, a factor of ~ 2 increase ($\Delta L_{\parallel} \sim 100\%$) should lead to a 40% increase in λ_q. Conversely, MONALISA simulations based on these two equilibria show a difference in λ_q which is within the Monte Carlo noise. This can be understood by detailing the build-up of λ_q along the path from the outer midplane to the outer target. Regardless of the position in the plasma, diffusion across flux surfaces during a time step dt leads to a local radial displacement $dr_{\mathrm{loc}}^2 = D_{\perp} dt$. Once such displacement is remapped to the outer midplane, it becomes by definition:

$$dr^2 \equiv \frac{1}{f_{\mathrm{x}}^2} dr_{\mathrm{loc}}^2 = \frac{1}{f_{\mathrm{x}}^2} D_{\perp} \frac{dL_{\parallel}}{c_{\mathrm{s}}} \tag{4.2}$$

where $dL_{\parallel}$ is the the parallel distance travelled at speed c_{s} during dt. Then λ_q can be calculated by cumulating all the radial displacements performed along the whole outer

midplane-to-target parallel path:

$$\lambda_q^2 = \int_{\text{omp}}^{\text{tgt}} dr^2 = \frac{D_\perp}{c_\text{s}} \int_{\text{omp}}^{\text{tgt}} \frac{dL_\parallel}{f_\text{x}^2} \equiv \frac{D_\perp}{c_\text{s}} L_\parallel^{\text{eff}} \tag{4.3}$$

where we introduce the *effective* parallel connection length as:

$$L_\parallel^{\text{eff}} = \frac{L_\parallel}{\langle f_\text{x}^2 \rangle} \tag{4.4}$$

in which $\langle f_\text{x} \rangle$ is the average of f_x over the whole $L_\parallel$. In other words, diffusion steps in the radial direction taking place in the region below the X-point are less effective in broadening $q_\parallel$ profiles because of the higher flux expansion, as can be seen in the 2D map shown in figure 4.3.b. When weighted by $\langle f_\text{x}^2 \rangle$, different portions of $L_\parallel$ do not matter equivalently:

$$L_\parallel^{\text{eff}} = \frac{L_\parallel^{\text{ups}}}{\langle f_\text{x}^{\text{ups}\ 2} \rangle} + \frac{L_\parallel^{\text{div}}}{\langle f_\text{x}^{\text{div}\ 2} \rangle} \simeq \frac{10\text{ m}}{1} + \frac{10\text{ m}}{3^2} \simeq 11\text{ m} \tag{4.5}$$

Therefore a factor of ~ 2 difference in $L_\parallel$, as for the two cases in figure 4.3.a ($\Delta L_\parallel \simeq 100\%$), corresponds to a $\Delta L_\parallel^{\text{eff}} = 10\%$ only, coherent with the $\Delta\lambda_q < 5\%$ found by MONALISA. This reasoning, valid for a purely diffusive system, supports the idea that λ_q, set by control parameters where f_x is small (upstream), is therefore basically independent of the details of the geometry of the divertor, where f_x is usually bigger.

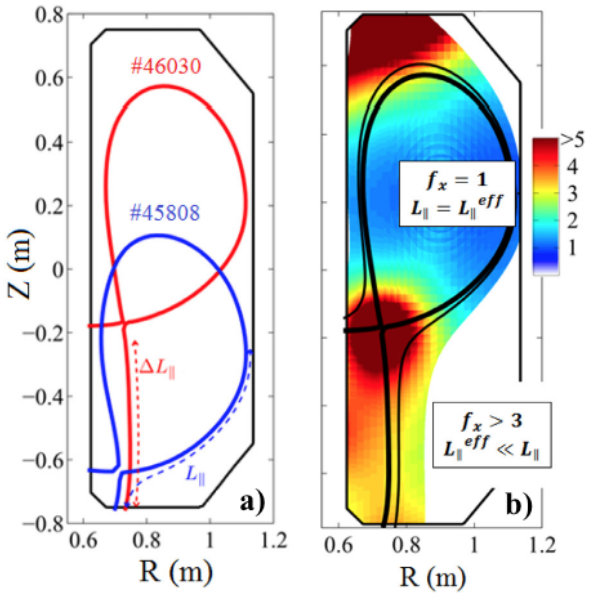

Figure 4.3: a) magnetic separatrix of two TCV equilibria with different parallel connection length $L_\parallel$; b) 2D map of the local flux expansion f_x for a long legged TCV plasma.

4.2 Diffusive fluid modelling: SolEdge2D-EIRENE

4.2.1 The SolEdge2D-EIRENE code package

A more sophisticated tool for the diffusive modelling of a plasma is the SolEdge2D-EIRENE code package [66, 67]. The fluid transport code SolEdge2D–EIRENE was developed with the goal of simulating the edge and SOL of a quasi-neutral plasma including interactions between the plasma and the tokamak wall. The code is capable of treating a variety of magnetic configurations (limited, diverted single and double nulls, snowflake [68], etc.), by using an explicit domain decomposition technique in which the different sub-domains are solved in parallel, saving computational time. The numerical specificity of the plasma module SolEdge2D is to use an immersed boundary condition technique, referred to as "penalization", which allows simulations of the plasma up to the first wall in a flexible manner. SolEdge2D solves for a two-species plasma (singly charged ions and electrons) the equations for n, $v_\parallel$, T_i and T_e assuming quasi-neutrality ($n_\mathrm{e} = n_\mathrm{i}$) and ambipolarity ($v_{\parallel\mathrm{i}} = v_{\parallel\mathrm{e}}$, which can be relaxed by including an equation for the electric potential). The transport of mass, parallel momentum and energy is described by equations 1 to 4 in [67], which are solved using a finite volume numerical scheme and assuming toroidal axisymmetry. While parallel transport is modelled following a collisional approach, the cross-field $\perp$ turbulent transport is reproduced through an ad hoc diffusive–convective model, such that the perpendicular particle flux is expressed as follows:

$$\Gamma_\perp = nv_\perp = -D_\perp \nabla_\perp n + nv_\mathrm{pinch} \tag{4.6}$$

with the addition of a term for magnetic drifts, when activated. The perpendicular anomalous diffusivities $D_\perp$, $\nu_\perp$ and $\chi_\perp$ and the pinch velocity v_pinch can be either chosen arbitrarily or inferred from experimental evidences as well as self consistent turbulent simulations (section 4.3). On the other hand the particle, momentum and energy source terms due to interactions with neutrals (atoms, molecules) are computed by the EIRENE Monte Carlo module. In the parallel direction, Bohm boundary conditions (BC) are ensured at the magnetic pre-sheath entrance by the penalization mask, which adds sink terms to the conservation equations that are active only in the wall region. The corresponding expressions of the parallel velocity and parallel heat flux at the boundary read as follows:

$$|v_{\parallel\mathrm{BC}}| \geq c_\mathrm{s} = \sqrt{\frac{T_\mathrm{e} + T_\mathrm{i}}{m_\mathrm{i}}} \tag{4.7}$$

$$q_{\parallel\mathrm{BC}} = \left(\frac{5}{2} n v_\parallel T - k \nabla_\parallel T\right)_\mathrm{BC} = \left(\gamma n v_\parallel T\right)_\mathrm{BC} \tag{4.8}$$

with default values of $\gamma_e = 4.5$ and $\gamma_i = 2.5$, as in [8]. The SolEdge2D code uses a mesh (grid) that is aligned to ψ surfaces, which are in most cases not aligned with the wall. Unlike other similar codes, that have to reshape the grid in the vicinity of the wall [69, 70], SolEdge2D relies on a different strategy, inspired from CFD methods [71, 72] and referred to as "penalization technique". With this approach there is no need for the grid to be aligned with the wall. The mesh is simply extended beyond the wall location and then a mask function is used to determine whether mesh cells belong to the plasma region or to the wall region. In this framework, changing the wall geometry requires only the tailoring of the "penalization" mask without the need of manufacturing a new grid. Figure 4.4 showcases the output of a SolEdge2D-EIRENE simulation based on the ψ map

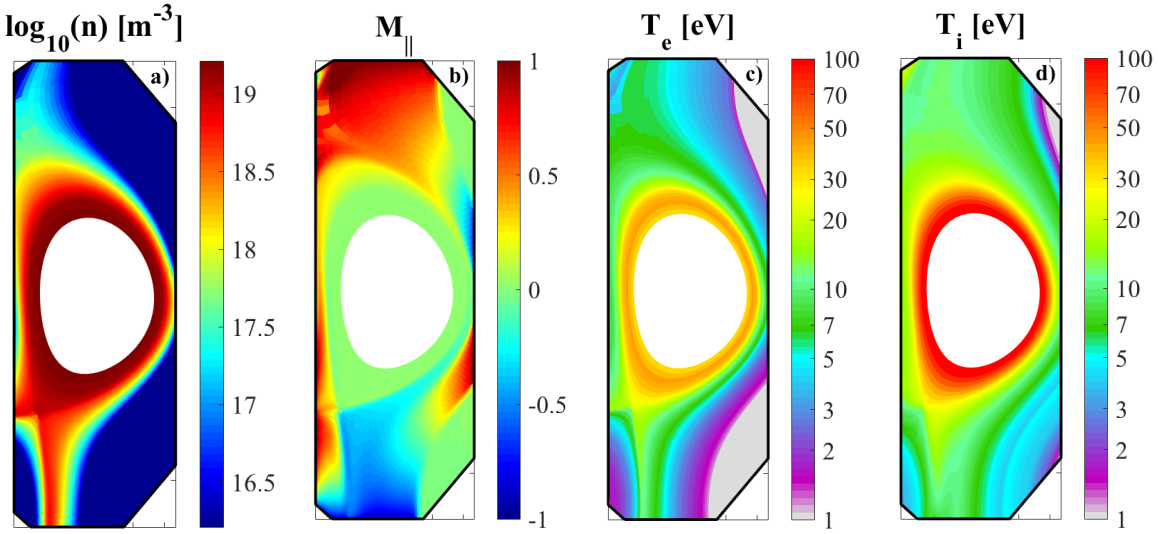

Figure 4.4: 2D maps of a) density logarithm, b) Mach number, c) electron temperature and d) ion temperature of a SolEdge2D-EIRENE simulation (TCV #51333, $t = 800$ s).

of the TCV shot #51333 at $t = 800$ s, namely 2D maps of a) $log_{10}(n)$, b) $M_\parallel = v_\parallel / c_s$, c) T_e and d) T_i. Since the core plasma is not modelled by the code, one has to set boundary condition at the inner barrier: for this simulation we impose $n_{IB} \simeq 1.68 \times 10^{19}$ m^{-3} and $T_{i,\,IB} \simeq T_{e,\,IB} = 169$ eV. As far as transport coefficients are concerned, we chose $D_\perp = 0.3$ m^2 s^{-1}, $\nu_\perp = 1$ m^2 s^{-1} and $\chi_{\perp,i} = \chi_{\perp,e} = 0.6$ m^2 s^{-1}, constant over the entire simulation domain. Results can be readily interpolated along the wall to obtain profiles such as those shown in figure 4.5: here the quantities shown in the 2D maps presented above with the addition of the total heat flux q are plotted along the wall coordinate. Here the localisation of floor, top, inner and outer wall of the machine is helped by vertical black lines and the corresponding labels. In particular, it is easy to recognise the position of the outer and inner strike points, sitting respectively on the floor and the inner wall, close to the peaking of n, T_e and q (solid lines in figure 4.5.a, b and c). On the other

hand T_i (dotted line in figure4.5.b) has on average values higher than T_e, with an overall smoother profile but broader and smaller peaks in the vicinity of the strike points. Figure 4.5.d highlights the presence of super-sonic parallel flows ($M_{\parallel} > 1$) at two the divertor targets, at the outer wall and in the vicinity of the upper, secondary, X-point at the top of the machine.

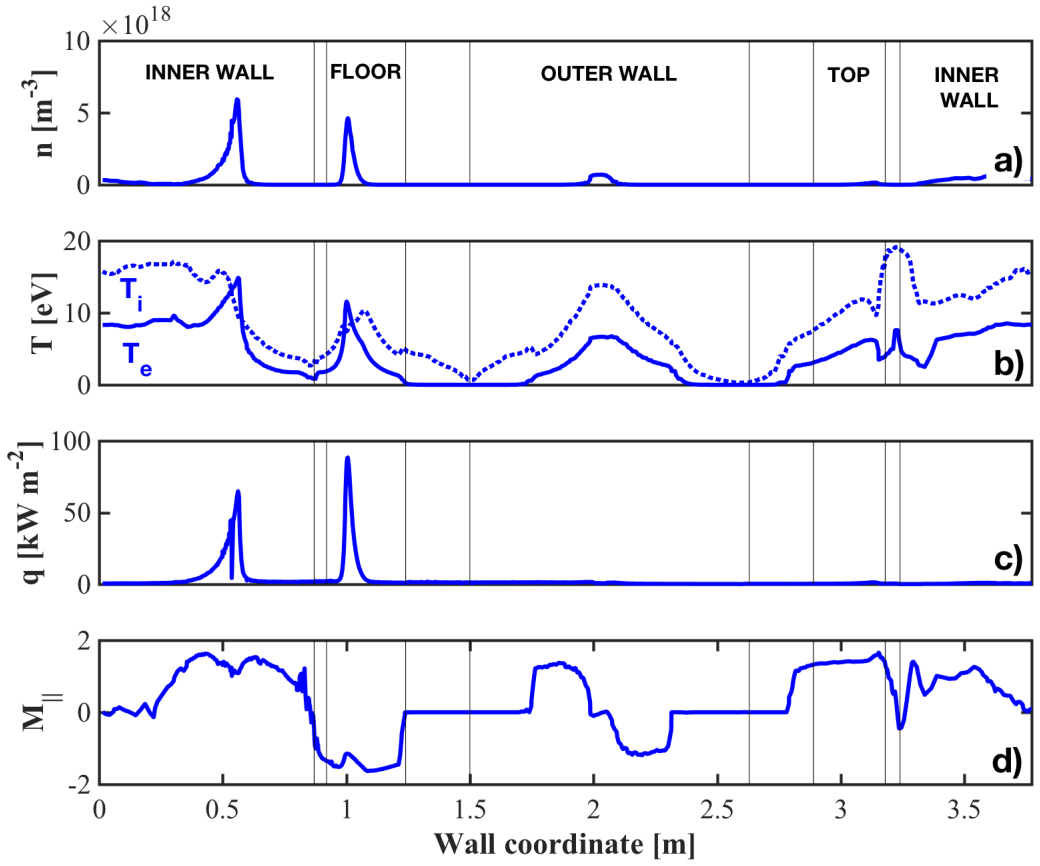

Figure 4.5: profiles of a) n, b) T_e (solid) and T_i (dotted), c) q, d) $M_{\parallel}$ along the TCV wall for a SolEdge2D-EIRENE simulations (TCV #51333, $t = 800$ s). Vertical lines and labels in a) identify different portions of the wall.

4.2.2 Radial profiles of the transport coefficients: the "auto-fit"

Instead of setting fixed values for the transport coefficients resulting in homogeneous diffusion in the entire simulations domain, as performed in section 4.2.1, one can prescribe radial profiles of $n(r)$ at $T(r)$ at a given poloidal location, which here is conveniently chosen to be the outer midplane. When operated in this fashion, which in the following will be called "auto-fit", SolEdge2D-EIRENE adopts the appropriate, radially dependent, transport coefficients in order to match the prescribed profiles of n_{omp} and T_{omp}, while

solving the rest of the domain. This method is especially interesting when one is willing to compare numerical results to experimental ones, which is one of the goals of this chapter. Let us consider as an example the main plasma measurements of the TCV shot #51333, already presented in section 3.2: in figure 4.6.a and b respectively we show experimental main plasma profiles of n_e and T_e from RCP (green diamonds) and TS (blue triangles) measurements remapped at the outer midplane. An hyperbolic tangent is then fitted to the experimental data, arbitrarily assuming $T_i > T_e$ in the SOL, in order to obtain a continuous and smooth input for the code. The corresponding transport coefficients

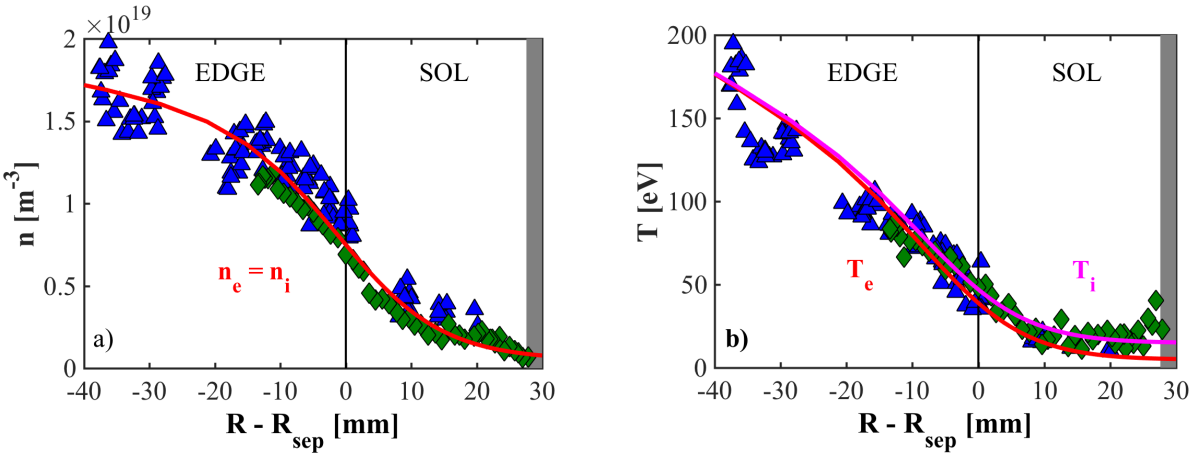

Figure 4.6: experimental main plasma profiles of a) n_e and b) T_e from RCP (green diamonds) and TS (blue triangles) measurements remapped at the outer midplane for TCV #51333. Solid lines for hyperbolic tangent fit, used as input for SolEdge2D-EIRENE auto-fit simulations.

adopted by SolEdge2D are represented by the red curves in figure 4.7 and compared with the constant ones imposed in the simulation discussed in section 4.2.1 indicated by the blue straight lines. If one considers figure 4.7.a and the value of $D_\perp$ obtained with the

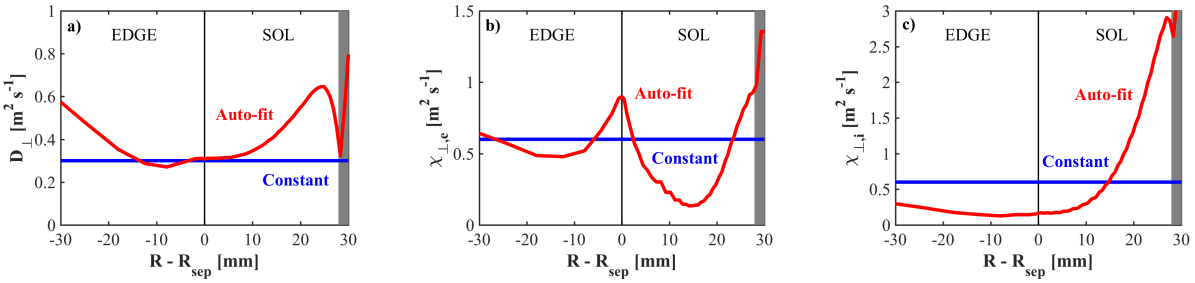

Figure 4.7: radial profiles (red lines) of perpendicular transport coefficients of a) mass, b) electron energy and c) ion energy from auto-fit to outer midplane profiles in figure 4.6. Constant coefficients (blue lines) correspond to simulations discussed in section 4.2.1.

auto-fit (red curve), one notices that it is not too dissimilar from the assumed constant

one (blue line), at least in the SOL over a $\lambda_n \simeq 10$ mm distance from the separatrix. This translates in a quite similar n profiles for the auto-fit simulation, as appears from figure 4.8.a, despite higher peak values at the strike points. Conversely, as shown by the red curve in figure 4.7.b, $\chi_{\perp,\mathrm{e}}$ has a much steeper profile when evaluated over a $\lambda_T \simeq 20$ mm distance from the separatrix and compared to the one used in the simulation with constant coefficients (blue line). As a consequence, the auto-fit T_e profile (red curve in figure 4.8.b) has ~ 2 time higher peak values at the strike points compared to the constant coefficients one (blue curve). On the other hand, despite a similar discrepancy in $\chi_{\perp,\mathrm{i}}$ between the auto-fit case (red curve in figure 4.7.c) and the constant coefficient one (blue curve), the T_i profile is only marginally impacted (red curve in figure 4.8.c) besides a higher and broader peak at the outer target. The biggest difference is observed for q profiles, shown in figure 4.8.d: here a factor of ~ 2.5 increase at the two strike points is measured for the auto-fit simulation (red curve) with respect to the constant coefficients one (blue curve).

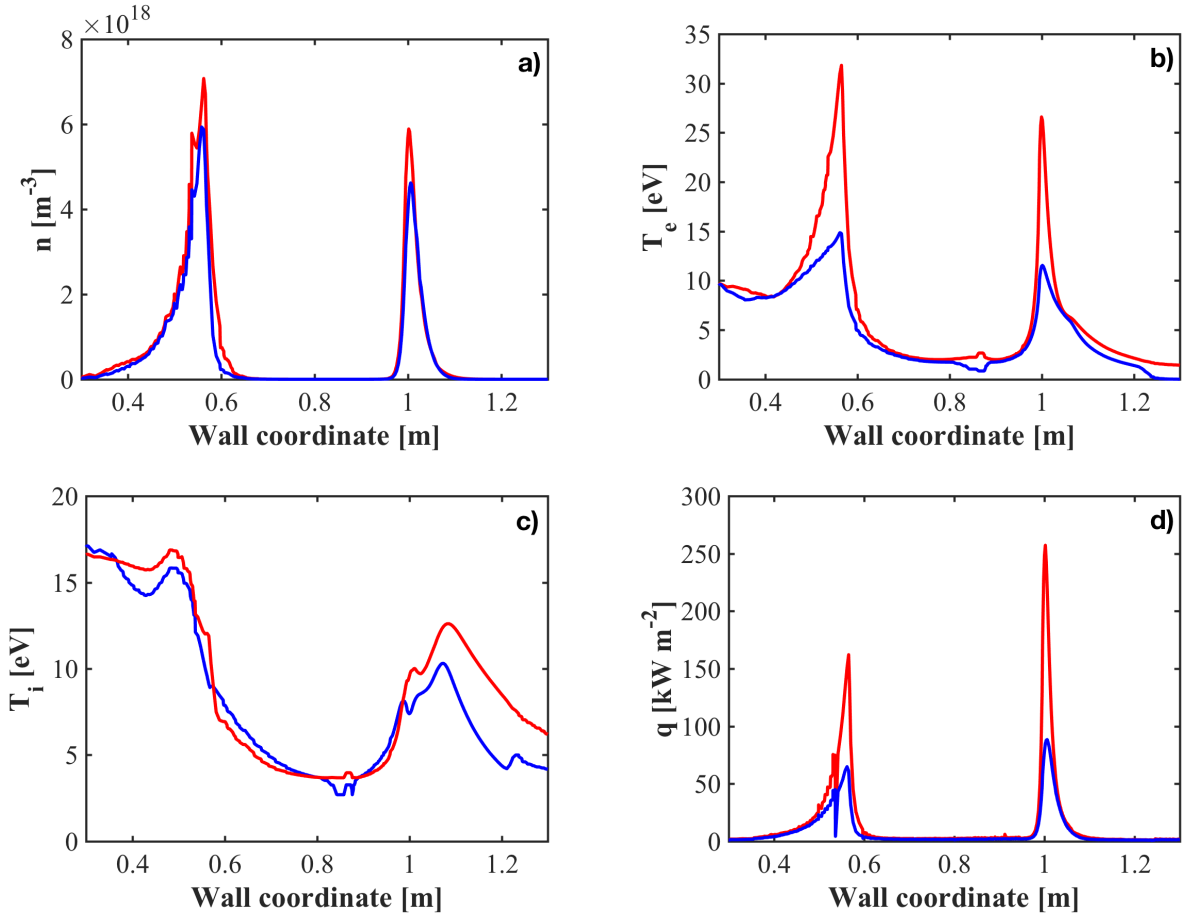

Figure 4.8: profiles of a) n, b) T_e, c) T_i, d) q at the strike points of a SolEdge2D-EIRENE simulation of TCV #51333 using transport coefficients from figure 4.7 (same color code).

It is worth comparing the results of these two methods of running SolEdge2D-EIRENE simulations with the experimental data for the corresponding TCV shot #51333. We focus here on experimental profiles measured with LP at the outer divertor target and then remapped at the outer midplane, as usual. Figure 4.9 contains profiles of a) n_e, b) T_e and c) q with the same color code for the simulations (red curves for the auto-fit simulation, blue curves for the constant coefficients one) and grey dots for LP data. Figure 4.9.a shows how the experimental n_e profile is better reproduced by the auto-fit case, with an almost quantitative match of both shape and peak value ($n_{e,max}^{a.f.} = 0.88 n_{e,max}^{LP}$) with respect to the constant coefficients one ($n_{e,max}^{c.c.} = 0.69 n_{e,max}^{LP}$). Interestingly, the far-SOL density shoulder, already discussed in section 3.3.1, is not present in the simulations, regardless the value of $D_\perp$. Conversely for T_e, as shown in figure 4.9.b, the agreement with the LP data is only qualitative for both methods: in fact the simulation with constant coefficients underestimates the experimental value ($T_{e,max}^{c.c.} = 0.65 T_{e,max}^{LP}$), while the auto-fit one overestimates it ($T_{e,max}^{a.f.} = 1.49 T_{e,max}^{LP}$). Last but not least, q profiles are presented in figure 4.9.c: as the reader can see the agreement with LP data is remarkably good for the auto-fit case ($q_{max}^{a.f.} = 0.98 q_{max}^{LP}$), while the peak heat flux is largely underestimated in the case of constant transport coefficients ($q_{max}^{c.c.} = 0.34 q_{max}^{LP}$). It has to be remembered

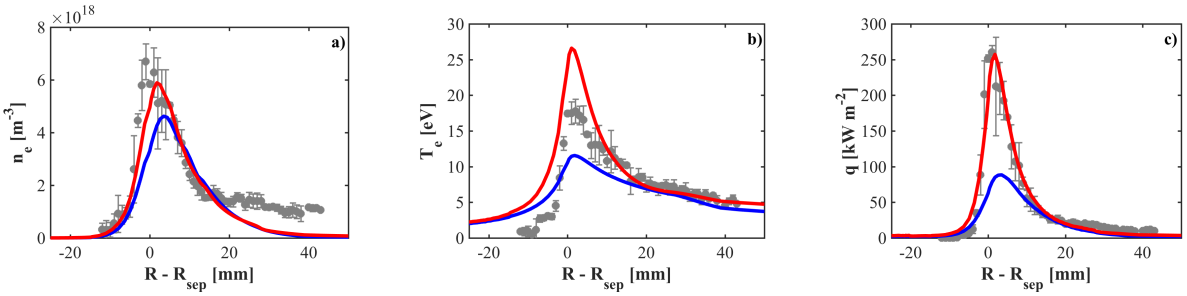

Figure 4.9: outer divertor target profiles of a) electron density, b) electron temperature and c) heat flux for the TCV shot #51333. Red lines and blue lines for the results of SolEdge2D-EIRENE simulations with auto-fit and constant transport coefficients respectively. Grey dots for experimental Langmuir probe measurements.

however that what is calculated by SolEdge2D is the total heat flux, assuming hot ions ($T_i \simeq T_e$, $\gamma = 7$) and including also a small contribution from radiation at the target ($q_{max}^{rad} \leq 0.03 q_{max}^{tot}$). Therefore it should rather be compared with the corresponding IR profile, not shown in figure 4.9.c for clarity, which has similar shape but higher peak value compared to LP (see figure 3.10). Comparison for the auto-fit case yields $q_{max}^{a.f.} = 0.61 q_{max}^{IR}$, while for the constant coefficients $q_{max}^{c.c.} = 0.21 q_{max}^{IR}$ is found. These fractions are in line with the ones of the power deposited at the outer target, for which we find $P_{tgt}^{a.f.} = 0.56 P_{tgt}^{IR}$ and $P_{tgt}^{c.c.} = 0.3 P_{tgt}^{IR}$. This discrepancy is due to a difference in the total power injected in

the system which is in fact an output of the simulations once the values of n_{IB} and T_{IB} in one case, or the profiles of n_{omp} and T_{omp} in the other, are imposed. Once the simulation reaches the steady state $P_{\mathrm{in}} = P_{\mathrm{out}}$ and therefore the power entering the domain can be estimated by integrating the total energy flux along the wall contour: by doing this one finds $P_{\mathrm{wall}}^{\mathrm{a.f.}} = 100.99$ kW and $P_{\mathrm{wall}}^{\mathrm{c.c.}} = 57.99$ kW, which corresponds to 51% and 29% of $P_{\mathrm{SOL}} = P_{\mathrm{Ohm}} - P_{\mathrm{rad}}^{\mathrm{core}} \simeq 200$ kW measured in the experiment. The lower P_{in} in the simulations compared to the experiment could have two explanations. The first one is related to the hypothesis made on T_{i}: in the auto-fit simulation the profile imposed at the outer midplane was arbitrarily chosen to be similar to the one of T_{e} and similarly for the value at the inner boundary in the simulation with constant transport coefficients. Given the lack of experimental measurements of T_{i}, it can not be excluded that the profile/value assumed here underestimates the real one. If one would impose a higher T_{i} profile, the code should inject more power in the system to sustain it and therefore a higher power would be found at the wall. On the other hand it has to be mentioned that no impurities were included in the simulations. This has consequences on the total radiated power: in the auto-fit simulation $P_{\mathrm{rad}}/P_{\mathrm{in}} = 0.17$, while in the constant coefficients simulation $P_{\mathrm{rad}}/P_{\mathrm{in}} = 0.21$. In both cases the ratio is lower than what measured experimentally for this shot, where $P_{\mathrm{rad}}/P_{\mathrm{Ohm}} = 0.31$. Accounting for impurities (Carbon being the dominant one in TCV) could induce SolEdge2D to inject more power in the system in order to handle their ionisation, leading to higher radiated power and therefore a higher P_{out}, closer to the experiment.

4.3 Self-consistent turbulent modelling: TOKAM3X

4.3.1 The TOKAM3X code

An alternative approach to the modelling of edge and SOL is to abandon the simplified diffusive picture and to take into account the turbulent nature of transport, as discussed in section 1.3.3. Turbulent plasma transport can be investigated with TOKAM3X [73, 74], a 3D fluid turbulent code solving a set of drift-reduced conservation equations for mass, parallel momentum, electric charge and energy for electrons and ions, in an electrostatic approximation. Turbulence appears naturally in TOKAM3X simulations and it's mainly due to interchange instabilities triggered when radial pressure gradients reach a threshold value. A flux-driven approach is adopted, in which a particle source is imposed in the closed field lines region, and the sink mechanism is provided by the sheath boundary conditions in the SOL. TOKAM3X gives a multi-scale description of turbulence, without separation of time nor space scales. A large spectrum of fluctuations is evaluated and the

interplay between different scales is self-consistently handled through non-linear terms. The equations in the model (see, for example, equations 1-4 in [74]) are normalized using the ion Larmor radius ρ_{L} and the inverse of the ion gyrofrequency ω_{C} as characteristic length and time scales respectively. A particle source is imposed at the inner boundary of the geometrical domain, in the closed flux surface region, in order to mimic an ionization source poloidally distributed over the plasma edge. Two important assumptions of the model are that the plasma is quasi-neutral ($n_{\mathrm{e}} = n_{\mathrm{i}}$) and isothermal ($T_{\mathrm{e}} = T_{\mathrm{i}}$). Another limitation of the model is the absence of neutral dynamics which are known to be an important player in SOL physics. A non-isothermal version of TOKAM3X, as well as the coupling with the Monte Carlo neutral code EIRENE, are currently being developed but were not employed in this analysis. For these reasons comparison with experimental results is expected to be more meaningful for for plasma in the flux-limited regime in which no strong poloidal variation of temperature is expected, the ionisation source is mainly localised in the confined region and neutral dynamics should have a weaker impact. The strong asset of TOKAM3X lies in its capability of simulating complex diverted magnetic geometries, as the ones investigated in this work, handling both closed and open field lines. This allows the study of specific features of X-point configurations, as the presence of the PFR, the non-homogeneity of f_{x} in the poloidal direction and the corresponding impact on cross-field transport. It has to be noted that TOKAM3X is run in a reduced geometry. This means that the geometry used in the code is a *homothetic* transformation (i.e. a homogeneous compression) of the reference equilibrium, which helps reducing the computational time. A physical time span corresponding to ~ 4 times the confinement time is typically simulated, in order to reach a full development of turbulence. The generic quantity calculated in a TOKAM3X simulation can be written as $X = \tilde{X} + \langle X \rangle_{\phi,t}$, where $\tilde{X}$ is the fluctuating component and $\langle X \rangle_{\phi,t}$ the mean-field one, averaged over toroidal angle ϕ and time t. The run is stopped once quantities averaged over ϕ are nearly constant in time. An example of output in a TOKAM3X simulation in TCV-like geometry, corresponding to the medium leg case of the experiment described in chapter 3, is the poloidal 2D map of the density fluctuations $\tilde{n}$ presented in figure 4.10.a: it is possible to notice how $\tilde{n}$ is strong in the main SOL, with larger radial extent and amplitude of the fluctuations at the LFS with respect to the HFS. Although being characterised by a smaller amplitude compared to the outer midplane, $\tilde{n}$ is non-negligible also all along the CFR of the outer divertor leg. This result is consistent with previous TOKAM3X simulations in COMPASS-like geometry reported by D. Galassi et al. [74], as well as with experimental observations in the MAST tokamak [75]. Another information that can be extracted from the simulations is the relative importance of the density fluc-

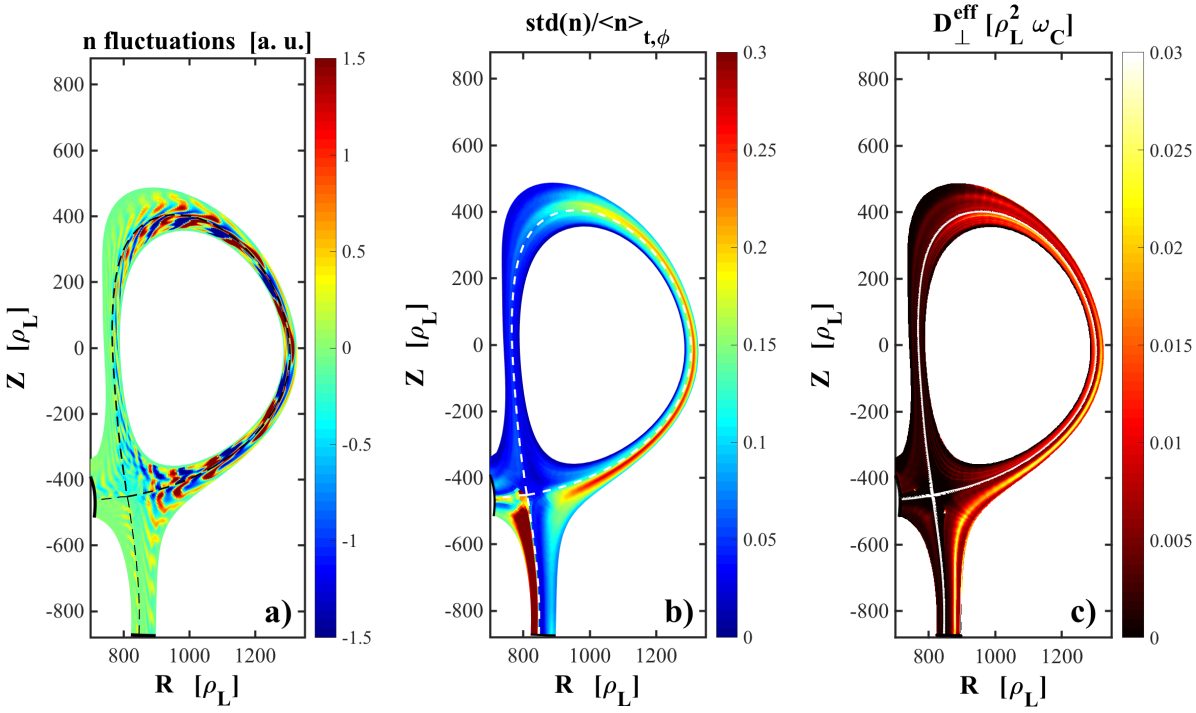

Figure 4.10: TOMAK3X 2D maps of a) density fluctuations $\tilde{n}$, b) relative intensity of fluctuations with respect to the mean density value $\tilde{n}/\langle n\rangle_{\phi,t}$ and c) effective diffusion coefficient $D_{\perp}^{\text{eff}}$, for a simulation in TCV-like reduced geometry based on shot #51333.

tuations with respect to the average density value, $\tilde{n}/\langle n\rangle_{\phi,t}$. The corresponding poloidal 2D map for the same TCV-like simulation is shown in figure 4.10.b: here it is possible to detect a region around the LFS midplane where fluctuations, which are associated to the turbulent component of the particle flux, are particularly strong with respect to the average density value, related to the mean-field transport. This feature, although reduced in amplitude, extends all along the far CFR, suggesting that turbulent transport can play an important role in the divertor. The reader might notice that the value of $\tilde{n}/\langle n\rangle_{\phi,t}$ is particularly strong in the PFR of the outer divertor leg: this is not really due to a strong absolute level of fluctuations (see figure 4.10.a), but rather to a very low mean density in this region. Therefore the total particle transport is much smaller in the PFR compared to main SOL and far CFR. An easier way to compare TOKAM3X results with those from diffusive simulations, and to visualise where radial transport is more important, consists in calculating an *effective diffusion coefficient*, representative of turbulent simulations. In analogy with diffusive models, we define this coefficient as:

$$D_{\perp}^{\text{eff}} \equiv -\Gamma_{\perp}^{\text{turb}}/\nabla_{\perp} n \tag{4.9}$$

Figure 4.10.c shows a 2D map of $D_{\perp}^{\text{eff}}$ for the same TCV-like simulation, highlighting some features: turbulent transport is indeed important at the outer midplane and it clearly extends poloidally upwards to the top of the main plasma and downwards close to the X-point, consistently with the ballooning character observed in experiments [28, 76] and mimicked in SolEdge2D-EIRENE ballooned simulations, to be presented in section 4.4.3). Importantly, $D_{\perp}^{\text{eff}}$ is strong in the far CFR of the outer divertor throughout the whole leg length. On the other hand, it is basically null at the LFS, around the X-point, along the outer divertor separatrix and in the PFR.

4.3.2 Turbulence, flux expansion and profile remapping

Recent work carried out by D. Galassi et al. [74] in characterizing the very first TOKAM3X simulations in X-point configuration in COMPASS-like geometry showed that the radial velocity of filamentary turbulent structures increases where f_{x} is higher. In other words, one might say that turbulent structures travel at constant speed in the magnetic space and, in order to do so, they accelerate in the geometrical space in order to cope with the flaring between ψ surfaces due to the flux expansion. This very interesting result instils some confidence in the remapping of SOL profiles introduced in section 2.2.2: if plasma transport takes place in the magnetic space, no loss of information is to be expected by remapping SOL profiles along iso-ψ surfaces. Conversely, it would not be rigorous to remap profiles that are the result of a transport process taking place in the geometrical space. Let us speculate about possible implications of this result on the standard parametrisation of target profiles, based on the two length scales λ_q and S_q. Suppose that λ_q is determined by the radial outward flux of filamentary turbulent structures travelling in the magnetic space and characterizing the main SOL and the far CFR, while S_q is due to collisional diffusive processes in the divertor region leading instead to a plasma transport in the geometrical space. In this scenario, remapping λ_q would make sense but remapping S_q would not. This reasoning agrees conceptually with recent findings by Maurizio et al. [39], who performed a scan of $f_{\text{x}}^{\text{tgt}}$ in TCV. The characterization of IR target q profiles highlighted a very different behaviour of the two parameters: despite an increasing λ_q^{tgt} with $f_{\text{x}}^{\text{tgt}}$, once remapped all the profiles showed basically the same λ_q; on the other hand a constant S_q^{tgt} was found, showing no impression of the strong variation of magnetic geometry on this quantity. This experiment represents one more case in which the divertor spreading factor showed to be rather insensitive to the scan of a divertor geometrical parameter, similarly to what discussed for the L_{div} and I_{P} scans. All these evidences concur suggesting that our understanding of S_q is still poor and this might also be due to the repeated conceptual mistake of upstream remapping a quantity

that is defined and has meaning only in the divertor.

4.4 Modelling of the TCV divertor leg experiment

This section concerns the modelling of the TCV divertor leg experiment described in chapter 3. The different codes presented earlier in this chapter, including different physics and based on different assumptions, have been employed. The results point out that the key to capture the different features of the effect of divertor geometry on SOL quantities, with focus on heat flux profiles, is the assumed degree of (dis)homogeneity of transport. The first attempt consists in using the diffusive models MONALISA (section 4.1) and SolEdge2D-EIRENE (section 4.2) employing uniform transport coefficients in the whole simulation domain. Then a radial dependence $D_\perp(r)$, $\chi_\perp(r)$ inferred from experimental measurements is assumed using the auto-fit method in SolEdge2D (section 4.2.2). A step further consists in modelling the so-called *ballooned* transport in which perpendicular transport is enhanced in the surroundings of the outer midplane: this can be done in SolEdge2D enforcing transport coefficients that change also in the poloidal direction: $D_\perp(r,\theta)$, $\chi_\perp(r,\theta)$. Last and more complex approach is to use the first-principle turbulent model TOKAM3X (section 4.3.1), in which particle fluxes are calculated self-consistently and therefore the corresponding *effective* perpendicular transport coefficient would differ from point to point in the simulation domain: $D_\perp^{\text{eff}}(R,Z)$.

4.4.1 Homogeneous perpendicular transport

An homogeneous perpendicular transport can be modelled through a diffusion coefficient whose value is constant in the entire simulation domain. This is one of the funding assumptions of the MONALISA code, introduced and described in section 4.1. Although the physics of transport is as simple as it can possibly get, featuring the real magnetic geometry from experimental ψ maps and the real tokamak wall contour, MONALISA can well reproduce the shape of experimental q profiles. This is demonstrated in figure 4.11, where the outer strike point numerical profile of q obtained with MONALISA (black line) superimposes nicely to experimental LP data (gray dots) for the TCV medium leg configuration ($L_{\text{div}} = 36$ cm). Nevertheless, attempts to model the divertor leg experiment with such code give mixed results: simulations with different L_{div} at constant $D_\perp = 0.5\ \text{m}^2\,\text{s}^{-1}$, $T = 40$ eV, $I_{\text{P}} = 210$ kA and $B_{\text{T}} = 1.4$ T, show no increase in λ_q (figure 4.12.a, black line) while a monotonically increasing S_q is predicted (figure 4.12.b, black line). MONALISA results fit well to IR experimental data (empty squares) for $L_{\text{div}} = 21$ and 36 cm, but the factor of 2 increase in λ_q for $L_{\text{div}} = 64$ cm, as well as the non

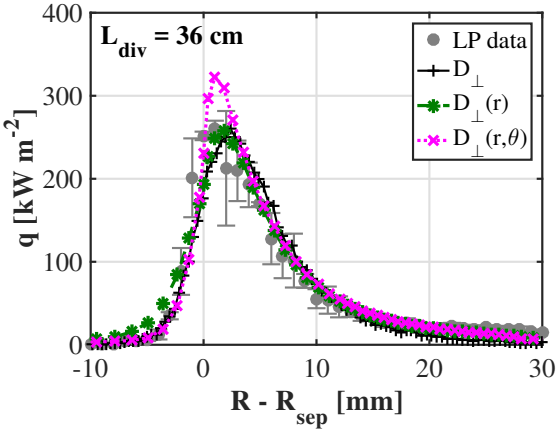

Figure 4.11: numerical heat flux profile at the outer divertor target for the medium leg configuration (L_{div} = 36 cm): constant $D_\perp$ (solid black line), $D_\perp(r)$ and $\chi_\perp(r)$ (dashed green line), $D_\perp(r,\theta)$ and $\chi_\perp(r,\theta)$ (dotted magenta line). Grey markers refer to experimental LP data shown in figure 3.10.a.

monotonic trend for S_q could not be captured. This leads, for the latter configuration, to a strong overestimation of the ratio S_q/λ_q (figure 4.12.c, black line) which is an indicator of the degree of asymmetry: when S_q/λ_q approaches 1, profiles become Gaussian-like while in experiments (S_q/λ_q = 0.3) these are much steeper on the PFR side than the CFR one. Simulations performed with the more sophisticated SolEdge2D-EIRENE code package, described in section 4.2, assuming constant transport coefficients, yield trends in qualitative agreement with MONALISA: λ_q is constant with $L_{\rm div}$ while S_q increases monotonically. Even though, in this kind of simulations, the values of the two scale lengths does not match with the experiment for the long leg case, and therefore the information about the relative importance of radial transport in the main SOL and divertor SOL could not be extracted, it is worth noting that $\lambda_{\rm int} = \lambda_q + 1.64\ S_q$ is in good agreement (figure 4.12.d, black line). This result suggests that, even for modified divertor geometries, this model can at least give a good indication about the average width of heat flux profiles.

4.4.2 Radially dependent perpendicular transport

A more sophisticated approach consists in assuming that perpendicular transport coefficients, and therefore the corresponding fluxes, can be inhomogeneous in the radial direction: e.g. for particles $\Gamma_\perp = -D_\perp(r)\nabla_\perp n$. If the variation of $D_\perp(r)$ and $\chi_\perp(r)$ is not strong, main SOL profiles can still be fit with a decaying exponential. Simulations under this assumption were performed with a more powerful modelling tool: the SolEdge2D-EIRENE code package, introduced in section 4.2. For this study, an fit to

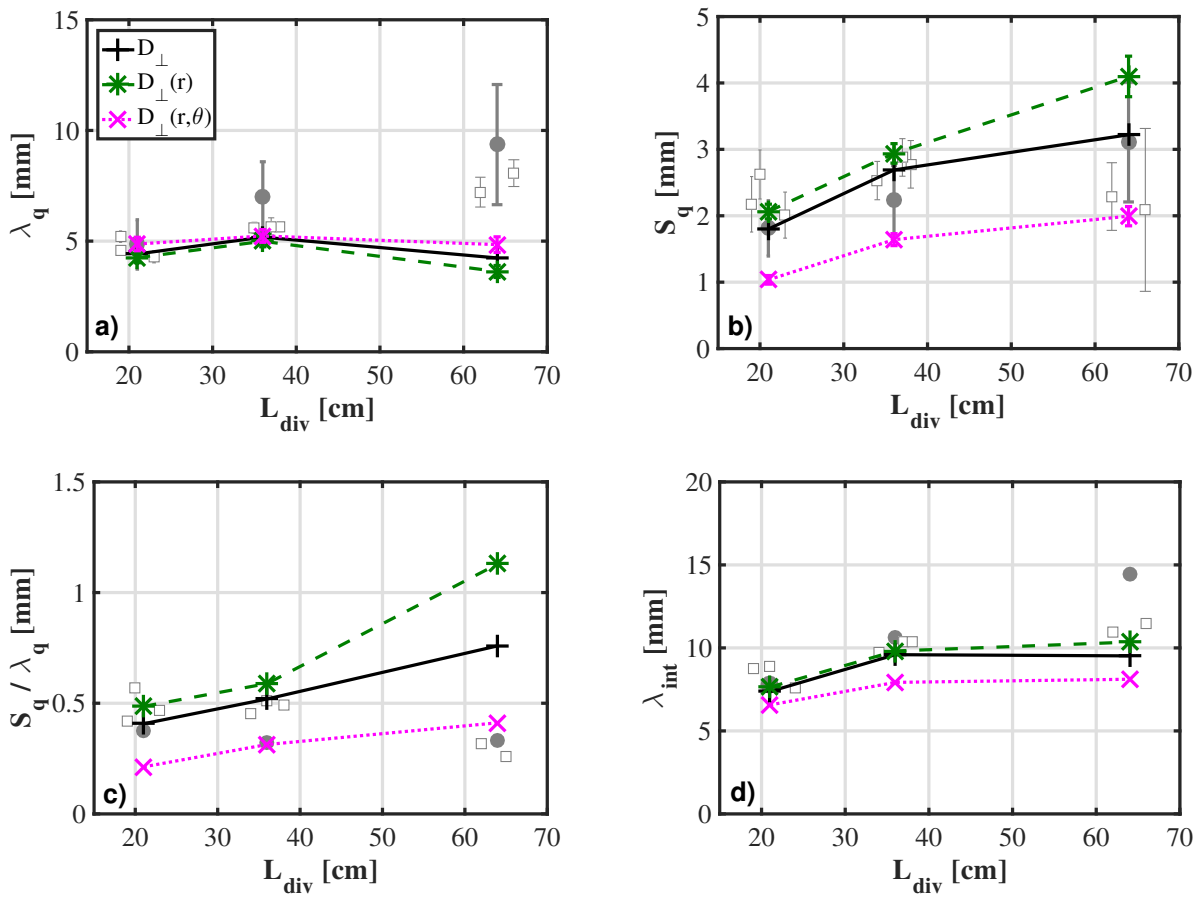

Figure 4.12: numerical results of a) λ_q, b) S_q, c) S_q/λ_q and d) λ_{int} as a function of L_{div} for constant $D_\perp$ (solid black line), $D_\perp(r)$ and $\chi_\perp(r)$ (dashed green line), $D_\perp(r,\theta)$ and $\chi_\perp(r,\theta)$ (dotted magenta line). Grey markers refer to experimental data from figure 3.10.

experimental outer midplane profiles of n_e and T_e from RCP and TS, available in the SOL region only for the configuration with $L_{\text{div}} = 36$ cm (medium leg), is used as input for all three configurations. This was done under the ansatz that outer midplane profiles would overlap in the SOL region regardless the value of L_{div} as they do for the edge and core region according to TS measurements, as shown in figure 3.4 and discussed throughout section 3.2. Radial profiles of the perpendicular transport coefficients $D_\perp(r)$ and $\chi_\perp(r)$ are therefore calculated with the auto-fit procedure, detailed in section 4.2.2. As shown by the green dashed line in figure 4.11, the simulated q profile for the medium leg configuration matches well the one obtained with MONALISA (black solid line) as well as the experimental LP data. The results in terms of profile widths, depicted by the green dashed lines in figure 4.12, are overall similar to those obtained with homogeneous perpendicular transport coefficients. These simulations, like those run with MONALISA (black lines) and SolEdge2D-EIRENE but with constant diffusivities (not shown), yield

an almost constant λ_q and an increasing S_q trend with L_{div}. For $L_{\text{div}} = 21$ cm and 36 cm, S_q basically coincides while for $L_{\text{div}} = 64$ cm SolEdge2D-EIRENE predicts a 30% higher value. Such an increase is most probably an effect of the temperature distribution along the divertor leg: a bigger drop and therefore a smaller $v_{\parallel}$ in the vicinity of the target allows a longer time for perpendicular diffusion. This translates in a ratio $S_q/\lambda_q = 1.13$ which is even further from the experimental trend. The reason of such a big divertor spreading can be visualized in figure 4.13.a where a 2D map of the perpendicular particle flux $\Gamma_{\perp}$ for the long legged plasma is shown. Here inward transport in the PFR is non-negligible along the entire divertor length and in the vicinity of the target it is as strong as the outward one in the CFR resulting in Gaussian-like profiles. Similarly to section 4.4.1, even though the λ_q trend is underestimated and the one of S_q overestimated, λ_{int} found in simulations is in good agreement with the data.

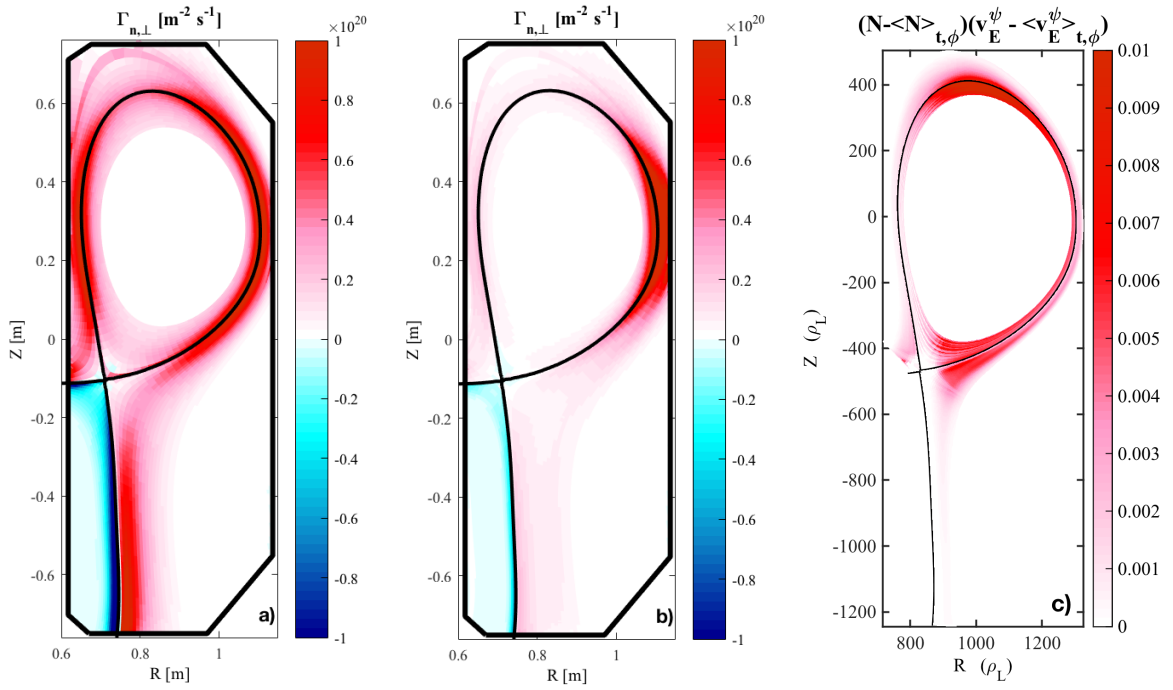

Figure 4.13: numerical 2D maps of $\Gamma_{\perp}$ for a) $D_{\perp}(r)$ and b) $D_{\perp}(r,\theta)$ from SolEdge2D-EIRENE diffusive simulations, and c) from TOKAM3X turbulent simulations (fluctuating component).

4.4.3 Ballooned perpendicular transport

One might instead suppose that perpendicular transport coefficients can vary both in the radial and poloidal direction: $D_{\perp}(r,\theta)$, $\chi_{\perp}(r,\theta)$. This hypothesis allows to mimic the so-called *ballooning*, meaning the enhanced turbulent transport localized in the vicinity

of the outer midplane observed, for instance, in limited plasmas on Tore Supra [28] and in diverted ones on Alcator C-mod [76]. Radius-dependent transport coefficients employed in the auto-fit SolEdge2D-EIRENE simulations discussed in section 4.4.2 are modified by adding a further Gaussian dependence in the poloidal direction which has the effect of reducing perpendicular transport away from the outer midplane. The corresponding target q profile (magenta dotted line in figure 4.11) is characterized by a smaller roll-over in the PFR, and therefore by a higher peak value, when compared to the one obtained with MONALISA (black line) or SolEdge2D-EIRENE with radially dependent perpendicular transport coefficients (green dashed line). The width of the profiles is therefore impacted (figure 4.12, dotted magenta lines): while λ_q is found to be basically the same as in previous simulations and therefore not to change with L_{div}, S_q is reduced by a factor of $\simeq 2$ coherently with a smaller, but still symmetric, perpendicular transport in the divertor. In fact, as shown in figure 4.13.b, in these simulations $\Gamma_\perp$ is strongly localized around the outer midplane, while it is damped everywhere else with respect to section 4.4.2 and figure 4.13.a. This translates in a stronger profile asymmetry for the long leg case ($S_q/\lambda_q = 0.4$) which gets much closer to what is found in experiments. As a consequence of the reduction of S_q, also λ_{int} gets smaller. Ballooning clearly represents an improved description of perpendicular transport but it is still however not possible to reproduce the experimental trend of λ_q with L_{div}.

4.4.4 Asymmetric divertor turbulent transport

A substantially different approach to the modelling of the TCV divertor leg experiment is the one used by the self-consistent turbulent transport code TOKAM3X, presented in section 4.3.1. It has to be kept in mind that in this kind of simulations plasma transport is inherently inhomogeneous and not governed by prescribed coefficients with radial or poloidal dependences, as instead in sections 4.4.1 to 4.4.3. Since the simulations presented here are obtained with the isothermal version of the code, the discussion will be restricted to density profiles, remembering that in such a model $\lambda_n = \lambda_q$. We start our analysis of TOKAM3X results by looking at the 2D map of the fluctuating component of the perpendicular particle flux $\Gamma_\perp^{\mathrm{turb}} = \langle \tilde{n}\, \tilde{v}_{\mathrm{E\times B}} \rangle_{t,\phi}$ for a simulation in long leg TCV-like geometry, shown in figure 4.13.c. Such map suggests the absence of radial turbulent transport in the PFR as well as in the immediate vicinity of the magnetic separatrix. This feature is in contrast with what is predicted by SolEdge2D-EIRENE simulations under the ansatz of symmetric perpendicular diffusion in the divertor (figures 4.13.a and 4.13.b). The turbulent perpendicular transport is instead strong in the main SOL, where it extends from the outer midplane up to the top of the equilibrium as well as close

to the X-point, and non-negligible in the far CFR, along the entire outer divertor leg length. We believe that the strong asymmetry in divertor radial transport highlighted by TOKAM3X simulations can be an important player in the divertor leg experiment. Let us now consider the profiles of density averaged over toroidal angle and time $\langle n \rangle_{\phi,t}$ at the outer midplane, shown in figure 4.14.a with the usual color code: red, blue and black for TCV-like equilibria with long, medium and short outer divertor leg respectively. Upstream profiles are characterized by similar absolute values and decay lengths, with $\langle n \rangle_{\phi,t}^{\text{sep}}$ and λ_n variations within 13% and 26% respectively. This result suggests that the length of the outer divertor leg has no or weak effect on the upstream plasma conditions, at least at the outer midplane, which are consistent between the three equilibria.

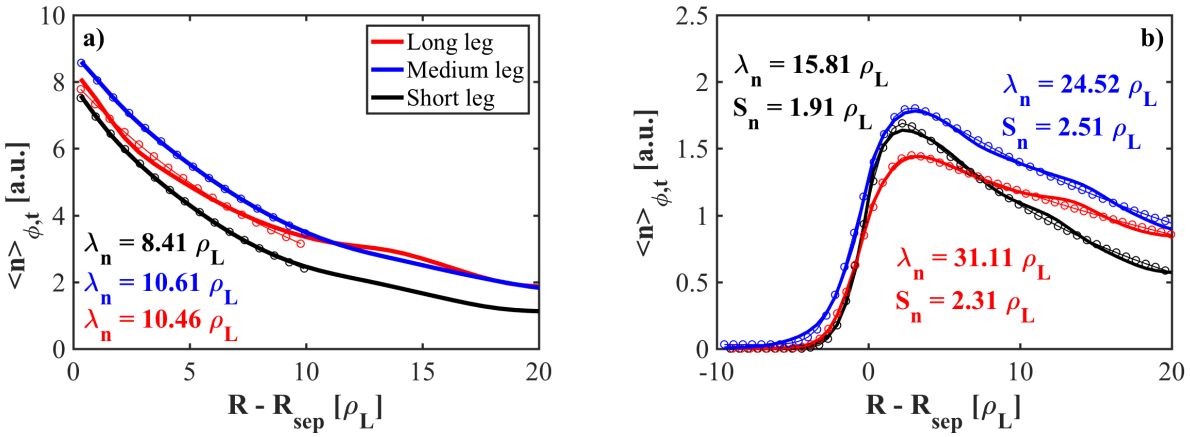

Figure 4.14: TOKAM3X profiles of density averaged over time and toroidal angle as a function of the radial distance from the outer midplane separatrix for simulations in long (red), medium (blue) and short (black) leg TCV-like geometry. Profiles are evaluated a) at outer midplane and b) at the outer divertor target (remapped). Decay lengths are obtained by fitting to eq. 2.18 in a) and to eq. 2.19 in b), indicated by the empty circles.

On the other hand, as appears from figure 4.14.b, outer divertor target profiles exhibit a clear monotonic increase of λ_n as a function of the divertor leg length, with a $\simeq 200\%$ difference between the short and long leg cases. Remarkably, this trend is in qualitative agreement with the factor-of-two increase in λ_q with L_{div} measured experimentally by both LP and IR (figure 3.10.c), which could not be captured by neither MONALISA nor SolEdge2D-EIRENE diffusive simulations. Conversely S_n, which is supposed to be the length scale of the divertor transport, has a smaller $\simeq 30\%$ variation and a non-monotonic trend with the divertor leg length. This feature is in qualitative agreement with the absence of S_q trend in IR and LP data presented in figure 3.10.d, where a similar scatter is found besides errorbars. When comparing the peak value at the outer target $\langle n \rangle_{\phi,t}^{\text{max}}$, the agreement between TOKAM3X and LP data (figure 3.8.b) is also

good, with a factor of 1.16 drop between short and long leg case. These decay lengths correspond to a profile asymmetry S_n/λ_n of 0.12, 0.10 and 0.07 for short, medium and long leg respectively. Such values are smaller than those observed experimentally (0.5, 0.4, 0.3) suggesting that, even though the effect of the divertor leg on transport in the CFR is nicely captured by TOKAM3X, the one towards the PFR is underestimated with respect to the measurements and even with respect to SolEdge2D-EIRENE ballooned simulations, in which divertor transport was strongly damped. For the three simulations we show in figure 4.15.a the evolution of λ_n as a function of the poloidal distance from the X-point along the outer divertor leg. The vertical dashed lines indicate the poloidal location of the divertor target, different in the three cases. Besides the common increasing trend and the values reached at the target, already shown in figure 4.14.b, it is interesting to see how λ_n at the poloidal location of the X-point, the divertor entrance, is already different in the three cases. This result suggests that, despite having similar values of λ_n at the outer midplane (figure 4.14.a), the effect of having a longer divertor leg is "felt" by the plasma along the path from the midplane to the X-point. Figure 4.15.b contains the

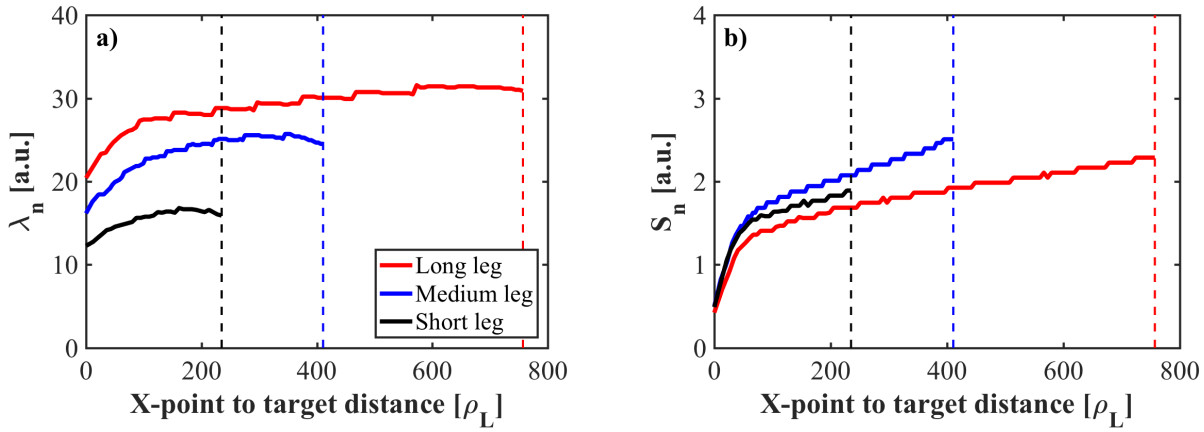

Figure 4.15: TOKAM3X profiles of a) λ_n and b) S_n as a function of the poloidal distance from the X-point along the outer divertor SOL for simulations in long (red), medium (blue) and short (black) leg TCV-like geometry. The dashed lines indicate the location of the outer divertor target.

corresponding plot for S_n: the three simulations exhibits similar trend, suggesting that most of the broadening takes place in the first 50 ρ_L below the X-point and afterwards it gently increases over the allowed divertor leg length. It should be mentioned that such an increase of both perpendicular transport scale lengths could also be related to the presence of a strong steady convective cell around the X-point in TOKAM3X simulations [74]: this causes the mean field transport in this region to be strong, despite the fact that its fluctuating component, as was shown in figure 4.13.c, is almost zero.

Conclusions

This work represents an effort to improve our understanding of the scrape-off layer width problem, possibly one of the most ill-posed and pressing issues for the next-generation fusion machines, starting with ITER. Even though this manuscript most probably represents just another small grain on top of a huge pile of sand, we believe that, by revisiting some of the currently established assumptions on the mechanisms setting the heat flux width, we contributed highlighting one more facet of the complex and possibly beneficial role played by the divertor magnetic geometry towards a safe and sustainable handling of the power exhaust in future fusion machines. We hope we captivated the reader's attention and we managed to convince her or him that the heat flux width is one of those key quantities in tokamak operations we do not fully comprehend nor control yet, but which has a crucial impact on the lifetime of PFCs with important consequences on the technological and economical feasibility of tomorrow's fusion-based power plants.

We recalled that, at present, our capabilities of predicting the heat flux width, or any SOL width really, are strongly limited by the absence of a self-consistent rigorous theoretical model able to infer it directly from physical parameters of the system (q_{95}, ρ_L/a, a/R, β, etc.). We therefore have to rely on empirical scaling laws based on engineering parameters (I_P, B_0, R_0, P_heat, $n_\mathrm{e,av}^\mathrm{core}$, etc.) obtained from experimental estimates in existing machines which certainly have a smaller size and possibly a different shape when compared to future ones. The most recent and accredited among these scaling laws [20, 40, 42] are based on the hypothesis that the width of the heat flux profile at the target of a diverted configuration is a combination of two length scales, λ_q and S_q, separately describing the competition between perpendicular and parallel transport in the main SOL and in the divertor SOL respectively [33, 34]. This picture, with the X-point acting as a frontier that sharply separates the two regions in the parallel direction, proposes that λ_q, set in the main SOL by whatever mechanism (turbulence, vertical drifts, etc.), depends mainly on $B_\mathrm{P}^\mathrm{omp}$ and is independent of the machine size and the specific divertor geometry. Vice versa S_q is supposed to be the result of diffusive collisional processes in the divertor

volume, causing a symmetric spreading of the main SOL exponential profiles in the perpendicular direction, towards both PFR and CFR.

In virtue of the results of a study of the effect of changing the length of the outer divertor leg on the power exhaust in low density, LSN, Ohmic, attached, L-mode plasmas discharges in TCV [38, 39], we conclude that this description of the problem is oversimplified, at least for the conditions explored in this thesis. In fact, experimental IR and LP measurements of the outer target heat flux profiles show a monotonic increase of λ_q with L_{div} with a factor of $\simeq 2$ difference over the explored range, despite being at constant $B_{\mathrm{P}}^{\mathrm{omp}}$. LP analysis of target profiles suggests that such broadening is driven by a strong increment in $\lambda_{n_{\mathrm{e}}}$ while $\lambda_{T_{\mathrm{e}}}$ is only slightly increasing. On the other hand, no trend of S_q with L_{div} is detected within the resolution of the two diagnostics. Such a strong effect of the divertor geometry on λ_q challenges the basic assumptions behind our current parametrisation of heat flux profiles and existing scaling laws, urging us to look at main SOL and divertor SOL as a "unique body", in which upstream and downstream transport cannot be arbitrarily disentangled. This is especially important for the interplay between main SOL and CFR which are directly connected by field lines and where, despite the possible damping effect of the X-point on turbulence coming from the core, it is hard to imagine a sharp separation of cross-field transport mechanisms. Therefore, at least in the above-mentioned experimental conditions, λ_q should be regarded as the radial transport length scale of both main SOL and CFR, while S_q is to capture the "aspiration" of the plasma in the PFR, across non-connected magnetic field lines, due to the non-infinite density gradient at the separatrix and to local collisional diffusive processes that become dominant where turbulent transport is weak.

This conclusion is supported by efforts to reproduce the trend of λ_q with L_{div} emerged in the TCV divertor leg experiment with numerical simulations. It is in fact observed that, in such modified magnetic configurations, a turbulent description is required. Modelling with TOKAM3X shows that turbulent filamentary structures, believed to be important and setting λ_q only in the main plasma, propagate instead also all along the outer divertor leg in the far CFR, while almost no transport is predicted in the vicinity of the separatrix and in the PFR. This asymmetric, outward-directed, turbulent transport in the divertor, enhanced in the case of a longer divertor leg, is a potential explanation of the broadening of λ_q with L_{div}. On the other hand, in TOKAM3X simulations, no big variation of cross-field transport is detected in the PFR while increasing L_{div}, consistently with experimental observations of a nearly constant spreading factor S_q with L_{div}. This

mechanism is most probably at play also in the more "traditional" divertor configurations, like the ones achieved on other machines and used to build scaling laws, as well as the TCV short and medium leg ones discussed in this work, although less evident because of the short X-point to target distance. For this reason a diffusive picture efficiently describes this kind of equilibria while strongly underestimates λ_q for the TCV long leg plasma.

We can therefore conclude that, for short legged plasmas, a diffusive description of cross-field transport can be a reasonable approximation. In fact, numerical simulations carried out with both a very simplified isothermal model with homogeneous diffusion like MONALISA [37] and a more complex fluid code like SolEdge2D-EIRENE [67], with radial-dependent perpendicular transport coefficients inferred from experimental measurements, are able to match reasonably well the experimental target heat flux profiles measured in TCV for short and medium values of L_{div}. The reason why these diffusive models fail capturing the impact of the divertor transport on λ_q was identified by building a large database of numerical heat flux profiles with the MONALISA code, exploiting its quick and flexible nature to scan a wide range of input parameters and a broad set of magnetic equilibria from different machines. In such framework, once target profiles are remapped at the outer midplane along ψ surfaces, the radial displacement occurred in regions as the divertor, where f_{x} is high, contributes only marginally in setting λ_q with respect to the radial displacement in the main SOL, where $f_{\mathrm{x}} \simeq 1$. This conclusion is strengthened by the good agreement between numerical values of λ_q found with MONALISA and the predictions of a simple theoretical model for a purely diffusive cylindrical plasma.

Besides the unexpected effect of a modified divertor leg length on λ_q, another important difference between TCV and the other devices included so far in divertor heat load studies has emerged. When scanning I_{P}, and therefore $B_{\mathrm{P}}^{\mathrm{omp}}$, in L-mode discharges with a standard (medium leg) divertor configuration, we found $\lambda_q^{\text{L-mode}}$ values that quantitatively match in both trend and amplitude with the multi-machine scaling law based on H-mode discharges [20]. This result suggests that, if the thumb-rule of $\lambda_q^{\text{H-mode}} \simeq 0.5\lambda_q^{\text{L-mode}}$ observed on JET and AUG [40] would be verified also on TCV, then $\lambda_q^{\text{H-mode}}$ values in TCV could fall below the prediction of the multi-machine scaling law, outside of its confidence interval. Besides generating possible speculations on the generality of the multi-machine scaling as a solid tool for the prediction of $\lambda_q^{\text{H-mode}}$ in devices that are not included in the original database and for the extrapolation to not yet existing ones, a similar result would suggest that one (or more) of the mechanisms setting λ_q in TCV, even in the case

of traditional magnetic configuration, does not feature in the scaling. This is a particularly interesting point, for which we don't have an explanation yet. In fact, the first heat load experiments in H-mode in TCV are ongoing at the time this manuscript is being written. Two among the main goals of this experimental campaign are of major interest and represent the natural continuation of this work: i) verifying whether the λ_q trend with L_{div} appears also in H-mode discharges, ii) discover whether $\lambda_q^{\text{H-mode}}$ agrees or not with the multi-machine scaling law.

The implications of this work on future machines like ITER and DEMO are non-trivial and difficult to test on other existing devices because of the limited flexibility in tuning the magnetic geometry. If what ultimately matters for the enhancement of turbulent transport in the divertor is the ratio of the divertor leg length to the total parallel connection length, then a strong effect should not be expected. ITER (and possibly DEMO) will have small $L_{\mathrm{div}}/L_{\parallel}$, similarly to most existing devices, and therefore could be satisfactorily described by diffusive codes, consistently with the short-legged TCV equilibria we investigated. If, on the other hand, the importance of turbulence in the divertor is inherently related to the absolute length of its leg, then an extra spreading of heat flux profiles could in principle occur in future bigger devices, even in the case of traditional magnetic configurations. It is worh mentioning that this enhancement of divertor cross-field transport does not seem to be compatible with other alternative divertor concepts as, for instance, the snowflake [77] or the super-X [78]. Since, according to both measurements in MAST [75] and TOKAM3X simulations [74], turbulence in the divertor is expected to be present only in the CFR far from the separatrix, the magnetic shear associated to the introduction of a second X-point (and therefore of a second separatrix) typical of a snowflake configuration could damp turbulence significantly. On the other hand, in a super-X configuration with a long but horizontal outer divertor leg, the pressure gradient and the magnetic field gradient would be orthogonal (unlike in our TCV experiment) and therefore one would not expect interchange turbulence to be triggered. If we were asked at this point to design the magnetic fusion reactor of the future, based solely on the conclusions of this work, we would then go for a scaled-up TCV with a very long, vertical, outer divertor leg and big flux expansion at the target. Moreover, one could speculate that in the case of detachment the higher resistivity of the colder plasma would further destabilize turbulence in the divertor, possibly leading to an even bigger, beneficial, heat load spreading.

Bibliography

[1] J D Lawson. Some criteria for a power producing thermonuclear reactor. *Proceedings of the Physical Society. Section B*, 70(1):6, 1957. (Cited in section 1.2.1.)

[2] J. Wesson and D.J. Campbell. *Tokamaks*. International series of monographs on physics. Clarendon Press, 2004. (Cited in sections 1.2.2 and 1.3.2.)

[3] F Wagner and U Stroth. Transport in toroidal devices-the experimentalist's view. *Plasma Physics and Controlled Fusion*, 35(10):1321, 1993. (Cited in section 1.3.3.)

[4] Paulett C. Liewer. Measurements of microturbulence in tokamaks and comparisons with theories of turbulence and anomalous transport. *Nuclear Fusion*, 25(5):543, 1985. (Cited in section 1.3.3.)

[5] A.J. Wootton. Edge turbulence. *Journal of Nuclear Materials*, 176:77 – 88, 1990. (Cited in section 1.3.3.)

[6] J. Bucalossi, M. Missirlian, P. Moreau, F. Samaille, E. Tsitrone, D. van Houtte, T. Batal, C. Bourdelle, M. Chantant, Y. Corre, X. Courtois, L. Delpech, L. Doceul, D. Douai, H. Dougnac, F. Faïsse, C. Fenzi, F. Ferlay, M. Firdaouss, L. Gargiulo, P. Garin, C. Gil, A. Grosman, D. Guilhem, J. Gunn, C. Hernandez, D. Keller, S. Larroque, F. Leroux, M. Lipa, P. Lotte, A. Martinez, O. Meyer, F. Micolon, P. Mollard, E. Nardon, R. Nouailletas, A. Pilia, M. Richou, S. Salasca, and J.-M. Travère. The west project: Testing iter divertor high heat flux component technology in a steady state tokamak environment. *Fusion Engineering and Design*, 89(7):907 – 912, 2014. Proceedings of the 11th International Symposium on Fusion Nuclear Technology-11 (ISFNT-11) Barcelona, Spain, 15-20 September, 2013. (Cited in section 1.2.)

[7] C S Pitcher and P C Stangeby. Experimental divertor physics. *Plasma Physics and Controlled Fusion*, 39(6):779, 1997. (Cited in sections 1.4.3 and 1.4.3.)

[8] P. C. Stangeby. *The Plasma Boundary of Magnetic Fusion Devices*. 2000. (Cited in sections 1.4.3, 1.4.3, 2.1, 2.1.2, 2.2.1, and 4.2.1.)

[9] A. Loarte, B. Lipschultz, A.S. Kukushkin, G.F. Matthews, P.C. Stangeby, N. Asakura, G.F. Counsell, G. Federici, A. Kallenbach, K. Krieger, A. Mahdavi, V. Philipps, D. Reiter, J. Roth, J. Strachan, D. Whyte, R. Doerner, T. Eich, W. Fundamenski, A. Herrmann, M. Fenstermacher, P. Ghendrih, M. Groth, A. Kirschner, S. Konoshima, B. LaBombard, P. Lang, A.W. Leonard, P. Monier-Garbet, R. Neu, H. Pacher, B. Pegourie, R.A. Pitts, S. Takamura, J. Terry, E. Tsitrone, the ITPA Scrape-off Layer, and Divertor Physics Topical Group. Chapter 4: Power and particle control. *Nuclear Fusion*, 47(6):S203, 2007. (Cited in sections 1.4.4 and 2.4.1.)

[10] J.P. Gunn, S. Carpentier-Chouchana, R. Dejarnac, F. Escourbiac, T. Hirai, M. Komm, A. Kukushkin, S. Panayotis, and R.A. Pitts. Ion orbit modelling of elm heat loads on iter divertor vertical targets. *Nuclear Materials and Energy*, 2016. (Cited in section 1.4.4.)

[11] J.P. Gunn, S. Carpentier-Chouchana, F. Escourbiac, T. Hirai, S. Panayotis, R.A. Pitts, Y. Corre, R. Dejarnac, M. Firdaouss, M. Kočan, M. Komm, A. Kukushkin, P. Languille, M. Missirlian, W. Zhao, and G. Zhong. Surface heat loads on the iter divertor vertical targets. *Nuclear Fusion*, 57(4):046025, 2017. (Cited in section 1.4.4.)

[12] R.A. Pitts, S. Bardin, B. Bazylev, M.A. van den Berg, P. Bunting, S. Carpentier-Chouchana, J.W. Coenen, Y. Corre, R. Dejarnac, F. Escourbiac, J. Gaspar, J.P. Gunn, T. Hirai, S-H. Hong, J. Horacek, D. Iglesias, M. Komm, K. Krieger, C. Lasnier, G.F. Matthews, T.W. Morgan, S. Panayotis, S. Pestchanyi, A. Podolnik, R.E. Nygren, D.L. Rudakov, G. De Temmerman, P. Vondracek, and J.G. Watkins. Physics conclusions in support of {ITER} w divertor monoblock shaping. *Nuclear Materials and Energy*, pages –, 2017. (Cited in section 1.4.4.)

[13] R.A. Pitts, S. Carpentier, F. Escourbiac, T. Hirai, V. Komarov, S. Lisgo, A.S. Kukushkin, A. Loarte, M. Merola, A. Sashala Naik, R. Mitteau, M. Sugihara, B. Bazylev, and P.C. Stangeby. A full tungsten divertor for iter: Physics issues and design status. *Journal of Nuclear Materials*, 438(Supplement):S48 – S56, 2013. Proceedings of the 20th International Conference on Plasma-Surface Interactions in Controlled Fusion Devices. (Cited in section 1.4.4.)

[14] A.S. Kukushkin, H.D. Pacher, G.W. Pacher, V. Kotov, R.A. Pitts, and D. Reiter. Consequences of a reduction of the upstream power sol width in iter. *Journal of Nuclear Materials*, 438(Supplement):S203 – S207, 2013. Proceedings of the 20th In-

ternational Conference on Plasma-Surface Interactions in Controlled Fusion Devices. (Cited in section 1.4.4.)

[15] S. I. Krasheninnikov, A. S. Kukushkin, and A. A. Pshenov. Divertor plasma detachment. *Physics of Plasmas*, 23(5):055602, 2016. (Cited in section 1.4.4.)

[16] C. Theiler, B. Lipschultz, J. Harrison, B. Labit, H. Reimerdes, C. Tsui, W.A.J. Vijvers, J. A. Boedo, B.P. Duval, S. Elmore, P. Innocente, U. Kruezi, T. Lunt, R. Maurizio, F. Nespoli, U. Sheikh, A.J. Thornton, S.H.M. van Limpt, K. Verhaegh, N. Vianello, the TCV team, and the EUROfusion MST1 team. Results from recent detachment experiments in alternative divertor configurations on tcv. *Nuclear Fusion*, 57(7):072008, 2017. (Cited in sections 1.4.4, 3.1.1, and 3.3.3.)

[17] F. L. Hinton and R. D. Hazeltine. Kinetic theory of plasma scrape-off in a divertor tokamak. *The Physics of Fluids*, 17(12):2236–2240, 1974. (Cited in section 2.1.2.)

[18] R.J. Goldston. Heuristic drift-based model of the power scrape-off width in low-gas-puff h-mode tokamaks. *Nuclear Fusion*, 52(1):013009, 2012. (Cited in section 2.1.2.)

[19] G. Giorgiani et al. A hybrid discontinuous galerkin method for tokamak edge plasma simulations in global realistic geometry. *submitted to Journal of Computational Physics*. (Cited in section 2.1.2.)

[20] T. Eich, A.W. Leonard, R.A. Pitts, W. Fundamenski, R.J. Goldston, T.K. Gray, A. Herrmann, A. Kirk, A. Kallenbach, O. Kardaun, A.S. Kukushkin, B. LaBombard, R. Maingi, M.A. Makowski, A. Scarabosio, B. Sieglin, J. Terry, A. Thornton, ASDEX Upgrade Team, and JET EFDA Contributors. Scaling of the tokamak near the scrape-off layer h-mode power width and implications for iter. *Nuclear Fusion*, 53(9):093031, 2013. (Cited in sections 2.1.2, 2.3.2, 2.3.3, 2.4.1, 3.4.1, 3.12, 4.1.1, and 4.4.4.)

[21] N. Fedorczak, J.P. Gunn, N. Nace, A. Gallo, C. Baudoin, H. Bufferand, G. Ciraolo, Th. Eich, Ph. Ghendrih, and P. Tamain. Width of turbulent {SOL} in circular plasmas: A theoretical model validated on experiments in tore supra tokamak. *Nuclear Materials and Energy*, pages –, 2017. (Cited in section 2.1.3.)

[22] H. M. Mott-Smith and Irving Langmuir. The theory of collectors in gaseous discharges. *Phys. Rev.*, 28:727–763, Oct 1926. (Cited in section 2.2.1.)

[23] Leonardo Patacchini and Ian H. Hutchinson. Kinetic solution to the mach probe problem in transversely flowing strongly magnetized plasmas. *Phys. Rev. E*, 80:036403, Sep 2009. (Cited in section 2.2.1.)

[24] A Herrmann, W Junker, K Gunther, S Bosch, M Kaufmann, J Neuhauser, G Pautasso, Th Richter, and R Schneider. Energy flux to the asdex-upgrade diverter plates determined by thermography and calorimetry. *Plasma Physics and Controlled Fusion*, 37(1):17, 1995. (Cited in section 2.2.1.)

[25] J. Sheffield. *Plasma scattering of electromagnetic radiation.* 1975. (Cited in section 2.2.1.)

[26] A Loarte, S Bosch, A Chankin, S Clement, A Herrmann, D Hill, K Itami, J Lingertat, B Lipschultz, K McCormick, R Monk, G.D Porter, M Shimada, and M Sugihara. Multi-machine scaling of the divertor peak heat flux and width for l-mode and h-mode discharges. *Journal of Nuclear Materials*, 266–269:587 – 592, 1999. (Cited in sections 2.2.2 and 2.3.2.)

[27] J Jacquinot and G T Hoang. Progress toward steady-state operation on tore supra. *Plasma Science and Technology*, 6(1):2101, 2004. (Cited in section 2.3.1.)

[28] J.P. Gunn, C. Boucher, M. Dionne, I. Ďuran, V. Fuchs, T. Loarer, I. Nanobashvili, R. Pánek, J.-Y. Pascal, F. Saint-Laurent, J. Stöckel, T. Van Rompuy, R. Zagórski, J. Adámek, J. Bucalossi, R. Dejarnac, P. Devynck, P. Hertout, M. Hron, G. Lebrun, P. Moreau, F. Rimini, A. Sarkissian, and G. Van Oost. Evidence for a poloidally localized enhancement of radial transport in the scrape-off layer of the tore supra tokamak. *Journal of Nuclear Materials*, 363–365:484 – 490, 2007. Plasma-Surface Interactions-17. (Cited in sections 2.3.1, 4.3.1, and 4.4.3.)

[29] M. Kočan, J.P. Gunn, J.-Y. Pascal, G. Bonhomme, P. Devynck, I. Ďuran, E. Gauthier, P. Ghendrih, Y. Marandet, B. Pegourie, and J.-C. Vallet. Measurements of scrape-off layer ion-to-electron temperature ratio in tore supra ohmic plasmas. *Journal of Nuclear Materials*, 390:1074 – 1077, 2009. Proceedings of the 18th International Conference on Plasma-Surface Interactions in Controlled Fusion Device. (Cited in section 2.3.1.)

[30] Y. Corre, J.P. Gunn, M. Firdaouss, S. Carpentier, M. Chantant, L. Colas, A. Ekedahl, J.-L. Gardarein, M. Lipa, T. Loarer, X. Courtois, D. Guilhem, and F. Saint-Laurent. Heat flux decay length during rf power operation in the tore supra tokamak. *Nuclear Fusion*, 54(1):013013, 2014. (Cited in section 2.3.1.)

[31] J Horacek, R A Pitts, J Adamek, G Arnoux, J-G Bak, S Brezinsek, M Dimitrova, R J Goldston, J P Gunn, J Havlicek, S-H Hong, F Janky, B LaBombard, S Marsen, G Maddaluno, L Nie, V Pericoli, Tsv Popov, R Panek, D Rudakov, J Seidl, D S Seo, M Shimada, C Silva, P C Stangeby, B Viola, P Vondracek, H Wang, G S Xu, Y Xu, and JET Contributors. Multi-machine scaling of the main sol parallel heat flux width in tokamak limiter plasmas. *Plasma Physics and Controlled Fusion*, 58(7):074005, 2016. (Cited in section 2.3.1.)

[32] M. Kocan, R.A. Pitts, G. Arnoux, I. Balboa, P.C. de Vries, R. Dejarnac, I. Furno, R.J. Goldston, Y. Gribov, J. Horacek, M. Komm, B. Labit, B. LaBombard, C.J. Lasnier, R. Mitteau, F. Nespoli, D. Pace, R. Panek, P.C. Stangeby, J.L. Terry, C. Tsui, and P. Vondracek. Impact of a narrow limiter sol heat flux channel on the iter first wall panel shaping. *Nuclear Fusion*, 55(3):033019, 2015. (Cited in section 2.3.1.)

[33] F. Wagner. A study of the perpendicular particle transport properties in the scrape-off layer of asdex. *Nuclear Fusion*, 25(5):525, 1985. (Cited in sections 2.3.2, 4.1.1, and 4.4.4.)

[34] T. Eich, B. Sieglin, A. Scarabosio, W. Fundamenski, R. J. Goldston, and A. Herrmann. Inter-elm power decay length for jet and asdex upgrade: Measurement and comparison with heuristic drift-based model. *Phys. Rev. Lett.*, 107:215001, Nov 2011. (Cited in sections 2.3.2, 2.3.2, 2.3.3, 2.4.1, 3.1.1, and 4.4.4.)

[35] M. A. Makowski, D. Elder, T. K. Gray, B. LaBombard, C. J. Lasnier, A. W. Leonard, R. Maingi, T. H. Osborne, P. C. Stangeby, J. L. Terry, and J. Watkins. Analysis of a multi-machine database on divertor heat fluxes. *Physics of Plasmas*, 19(5):056122, 2012. (Cited in sections 2.3.2 and 3.4.1.)

[36] D.L. Rudakov, J.A. Boedo, R.A. Pitts, G.L. Jackson, C.J. Lasnier, A.W. Leonard, R.A. Moyer, P.C. Stangeby, G.R. Tynan, and J.G. Watkins. Sol width in limited versus diverted discharges in diii-d. *Journal of Nuclear Materials*, 415(1):S387 – S390, 2011. Proceedings of the 19th International Conference on Plasma-Surface Interactions in Controlled Fusion. (Cited in section 2.3.2.)

[37] A. Gallo, N. Fedorczak, R. Maurizio, C. Theiler, S. Elmore, B. Labit, H. Reimerdes, F. Nespoli, P. Ghendrih, and T. Eich. Effect of plasma geometry on divertor heat flux spreading: Monalisa simulations and experimental results from tcv. *Nuclear Materials and Energy*, pages –, 2016. (Cited in sections 2.3.2, 4.1.1, and 4.4.4.)

[38] A. Gallo et al. Impact of the plasma geometry on divertor power exhaust: experimental evidence from tcv and simulations with soledge2d and tokam3x. *accepted for publication by Plasma Physics and Controlled Fusion*, 2017. (Cited in sections 2.3.2 and 4.4.4.)

[39] R. Maurizio, S. Elmore, N. Fedorczak, A. Gallo, H. Reimerdes, B. Labit, C. Theiler, C.K. Tsui, W.A.J. Vijvers, The TCV Team, and The MST1 Team. Divertor power load studies for attached l-mode single-null plasmas in tcv. *Nuclear Fusion*, 58(1):016052, 2018. (Cited in sections 2.3.2, 2.4.3, 3.1.1, 3.3.3, 3.4.1, 4.3.2, and 4.4.4.)

[40] A. Scarabosio, T. Eich, A. Herrmann, and B. Sieglin. Outer target heat fluxes and power decay length scaling in l-mode plasmas at jet and aug. *Journal of Nuclear Materials*, 438:S426 – S430, 2013. Proceedings of the 20th International Conference on Plasma-Surface Interactions in Controlled Fusion Devices. (Cited in sections 2.3.2, 2.4.2, 3.4.1, 3.12, and 4.4.4.)

[41] T. Eich, B. Sieglin, A. Scarabosio, A. Herrmann, A. Kallenbach, G.F. Matthews, S. Jachmich, S. Brezinsek, M. Rack, and R.J. Goldston. Empiricial scaling of inter-elm power widths in asdex upgrade and jet. *Journal of Nuclear Materials*, 438(Supplement):S72 – S77, 2013. Proceedings of the 20th International Conference on Plasma-Surface Interactions in Controlled Fusion Devices. (Cited in sections 2.3.2, 2.4.4, and 3.4.1.)

[42] B Sieglin, T Eich, A Scarabosio, G Arnoux, I Balboa, S Devaux, A Herrmann, F Hoppe, M Hölzl, A Kallenbach, P Lang, G F Matthews, S Marsen, S Pamela, M Rack, R Wenninger, the ASDEX Upgrade Team, and JET EFDA Contributors. Power load studies in jet and asdex-upgrade with full-w divertors. *Plasma Physics and Controlled Fusion*, 55(12):124039, 2013. (Cited in sections 2.3.2, 2.4.3, and 4.4.4.)

[43] H J Sun, E Wolfrum, T Eich, B Kurzan, S Potzel, U Stroth, and the ASDEX Upgrade Team. Study of near scrape-off layer (sol) temperature and density gradient lengths with thomson scattering. *Plasma Physics and Controlled Fusion*, 57(12):125011, 2015. (Cited in sections 2.3.2 and 2.4.4.)

[44] A. Scarabosio, T. Eich, F. Hoppe, I. Paradela, B. Sieglin, F. Reimold, M. Rack, M. Groth, M. Wischmeier, G. Arnoux, I. Balboa, and S. Marsen. Scaling of the divertor power spreading (s-factor) in open and closed divertor operation in jet and

asdex upgrade. *Journal of Nuclear Materials*, 463(Supplement C):49 – 54, 2015. PLASMA-SURFACE INTERACTIONS 21. (Cited in sections 2.3.2 and 2.4.3.)

[45] Robert J. Goldston. Downstream heat flux profile versus midplane t profile in tokamaks. *Physics of Plasmas*, 17(1):012503, 2010. (Cited in section 2.3.3.)

[46] B Sieglin, T Eich, M Faitsch, A Herrmann, A Scarabosio, and the ASDEX Upgrade Team. Investigation of scrape-off layer and divertor heat transport in asdex upgrade l-mode. *Plasma Physics and Controlled Fusion*, 58(5):055015, 2016. (Cited in section 2.4.3.)

[47] H. Zohm, C. Angioni, E. Fable, G. Federici, G. Gantenbein, T. Hartmann, K. Lackner, E. Poli, L. Porte, O. Sauter, G. Tardini, D. Ward, and M. Wischmeier. On the physics guidelines for a tokamak demo. *Nuclear Fusion*, 53(7):073019, 2013. (Cited in section 2.4.3.)

[48] P.C. Stangeby, J.M. Canik, and D.G. Whyte. The relation between upstream density and temperature widths in the scrape-off layer and the power width in an attached divertor. *Nuclear Fusion*, 50(12):125003, 2010. (Cited in section 2.4.4.)

[49] S. Coda, J. Ahn, R. Albanese, S. Alberti, E. Alessi, S. Allan, H. Anand, G. Anastassiou, Y. Andrèbe, C. Angioni, M. Ariola, M. Bernert, M. Beurskens, W. Bin, P. Blanchard, T.C. Blanken, J.A. Boedo, T. Bolzonella, F. Bouquey, F.H. Braunmüller, H. Bufferand, P. Buratti, G. Calabró, Y. Camenen, D. Carnevale, F. Carpanese, F. Causa, R. Cesario, I.T. Chapman, O. Chellai, D. Choi, C. Cianfarani, G. Ciraolo, J. Citrin, S. Costea, F. Crisanti, N. Cruz, A. Czarnecka, J. Decker, G. De Masi, G. De Tommasi, D. Douai, M. Dunne, B.P. Duval, T. Eich, S. Elmore, B. Esposito, M. Faitsch, A. Fasoli, N. Fedorczak, F. Felici, O. Février, O. Ficker, S. Fietz, M. Fontana, L. Frassinetti, I. Furno, S. Galeani, A. Gallo, C. Galperti, S. Garavaglia, I. Garrido, B. Geiger, E. Giovannozzi, M. Gobbin, T.P. Goodman, G. Gorini, M. Gospodarczyk, G. Granucci, J.P. Graves, R. Guirlet, A. Hakola, C. Ham, J. Harrison, J. Hawke, P. Hennequin, B. Hnat, D. Hogeweij, J.-Ph. Hogge, C. Honoré, C. Hopf, J. Horáček, Z. Huang, V. Igochine, P. Innocente, C. Ionita Schrittwieser, H. Isliker, R. Jacquier, A. Jardin, J. Kamleitner, A. Karpushov, D.L. Keeling, N. Kirneva, M. Kong, M. Koubiti, J. Kovacic, A. Krämer-Flecken, N. Krawczyk, O. Kudlacek, B. Labit, E. Lazzaro, H.B. Le, B. Lipschultz, X. Llobet, B. Lomanowski, V.P. Loschiavo, T. Lunt, P. Maget, E. Maljaars, A. Malygin, M. Maraschek, C. Marini, P. Martin, Y. Martin, S. Mastrostefano, R. Maurizio, M. Mavridis, D. Mazon, R. McAdams, R. McDermott, A. Merle, H. Meyer,

F. Militello, I.G. Miron, P.A. Molina Cabrera, J.-M. Moret, A. Moro, D. Moulton, V. Naulin, F. Nespoli, A.H. Nielsen, M. Nocente, R. Nouailletas, S. Nowak, T. Odstrčil, G. Papp, R. Papřok, A. Pau, G. Pautasso, V. Pericoli Ridolfini, P. Piovesan, C. Piron, T. Pisokas, L. Porte, M. Preynas, G. Ramogida, C. Rapson, J. Juul Rasmussen, M. Reich, H. Reimerdes, C. Reux, P. Ricci, D. Rittich, F. Riva, T. Robinson, S. Saarelma, F. Saint-Laurent, O. Sauter, R. Scannell, Ch. Schlatter, B. Schneider, P. Schneider, R. Schrittwieser, F. Sciortino, M. Sertoli, U. Sheikh, B. Sieglin, M. Silva, J. Sinha, C. Sozzi, M. Spolaore, T. Stange, T. Stoltzfus-Dueck, P. Tamain, A. Teplukhina, D. Testa, C. Theiler, A. Thornton, L. Tophøj, M.Q. Tran, C. Tsironis, C. Tsui, A. Uccello, S. Vartanian, G. Verdoolaege, K. Verhaegh, L. Vermare, N. Vianello, W.A.J. Vijvers, L. Vlahos, N.M.T. Vu, N. Walkden, T. Wauters, H. Weisen, M. Wischmeier, P. Zestanakis, M. Zuin, and the EUROfusion MST1 team. Overview of the tcv tokamak program: scientific progress and facility upgrades. *Nuclear Fusion*, 57(10):102011, 2017. (Cited in section 3.1.1.)

[50] R Behn, A Alfier, S Yu Medvedev, Ge Zhuang, R Pasqualotto, P Nielsen, Y Martin, and the TCV team. Edge profiles of electron temperature and density during elmy h-mode in ohmically heated tcv plasmas. *Plasma Physics and Controlled Fusion*, 49(8):1289, 2007. (Cited in section 3.1.1.)

[51] J.A. Boedo, N. Crocker, L. Chousal, R. Hernandez, J. Chalfant, H. Kugel, P. Roney, and J. Wertenbaker. Fast scanning probe for the nstx spherical tokamak. *Review of Scientific Instruments*, 80(12):123506, 2009. (Cited in sections 3.1.1 and 3.2.2.)

[52] R.A. Pitts, S. Alberti, P. Blanchard, J. Horacek, H. Reimerdes, and P.C. Stangeby. Elm driven divertor target currents on tcv. *Nuclear Fusion*, 43(10):1145, 2003. (Cited in sections 3.1.1 and 3.3.)

[53] Martin Greenwald. Density limits in toroidal plasmas. *Plasma Physics and Controlled Fusion*, 44(8):R27, 2002. (Cited in section 3.1.2.)

[54] U. A. Sheikh, B. P. Duval, B. Labit, and F. Nespoli. A novel carbon coating technique for foil bolometers. *Review of Scientific Instruments*, 87(11):11D431, 2016. (Cited in section 3.2.3.)

[55] James P. Gunn, Claude Boucher, Barry L. Stansfield, and Sylvio Savoie. Flush-mounted probes in the divertor plates of tokamak de varennes. *Review of Scientific Instruments*, 66(1):154–159, 1995. (Cited in section 3.3.)

[56] M. Bagatin, D. Desideri, E. Martines, G. Manduchi, G. Serianni, and V. Antoni. Automatic fast fitting of single langmuir probe characteristics on rfx. *Review of Scientific Instruments*, 68(1):365–368, 1997. (Cited in section 3.3.)

[57] G.P. Canal, T. Lunt, H. Reimerdes, B.P. Duval, B. Labit, W.A.J. Vijvers, and the TCV Team. Enhanced exb drift effects in the tcv snowflake divertor. *Nuclear Fusion*, 55(12):123023, 2015. (Cited in section 3.3.1.)

[58] D. Carralero, G. Birkenmeier, H.W. Müller, P. Manz, P. deMarne, S.H. Müller, F. Reimold, U. Stroth, M. Wischmeier, E. Wolfrum, and The ASDEX Upgrade Team. An experimental investigation of the high density transition of the scrape-off layer transport in asdex upgrade. *Nuclear Fusion*, 54(12):123005, 2014. (Cited in section 3.3.1.)

[59] R. Maurizio. Spc, private communication. 2017. (Cited in section 3.4.1.)

[60] M. Faitsch et al. Triangularity dependence of the l-mode scrape-off layer power fall-off length in tcv. *submitted to Plasma Physics and Controlled Fusion*. (Cited in sections 3.4.2, 3.13, 3.14, and 3.15.)

[61] M Faitsch, B Sieglin, T Eich, H J Sun, and A Herrmann. Change of the scrape-off layer power width with the toroidal b-field direction in asdex upgrade. *Plasma Physics and Controlled Fusion*, 57(7):075005, 2015. (Cited in section 3.4.2.)

[62] Y. Camenen, A. Pochelon, R. Behn, A. Bottino, A. Bortolon, S. Coda, A. Karpushov, O. Sauter, G. Zhuang, and the TCV team. Impact of plasma triangularity and collisionality on electron heat transport in tcv l-mode plasmas. *Nuclear Fusion*, 47(7):510, 2007. (Cited in section 3.4.2.)

[63] Antoine POCHELON, Paolo ANGELINO, Roland BEHN, Stephan BRUNNER, Stefano CODA, Nataliya KIRNEVA, Sergei Yu MEDVEDEV, Holger REIMERDES, Jonathan ROSSEL, Olivier SAUTER, Laurent VILLARD, Dávid WÁGNER, Alberto BOTTINO, Yann CAMENEN, Gustavo P. CANAL, Prabal K. CHATTOPADHYAY, Basil P. DUVAL, Ambrogio FASOLI, Timothy P. GOODMAN, Sébastien JOLLIET, Alexander KARPUSHOV, Benoît LABIT, Alessro MARINONI, Jean-Marc MORET, Andreas PITZSCHKE, Laurie PORTE, Mikael RANCIC, Victor S. UDINTSEV, and the TCV Team. Recent tcv results - innovative plasma shaping to improve plasma properties and insight. *Plasma and Fusion Research*, 7:2502148–2502148, 2012. (Cited in section 3.4.2.)

[64] A Marinoni, S Brunner, Y Camenen, S Coda, J P Graves, X Lapillonne, A Pochelon, O Sauter, and L Villard. The effect of plasma triangularity on turbulent transport: modeling tcv experiments by linear and non-linear gyrokinetic simulations. *Plasma Physics and Controlled Fusion*, 51(5):055016, 2009. (Cited in section 3.4.2.)

[65] H. Bufferand, C. Baudoin, J. Bucalossi, G. Ciraolo, J. Denis, N. Fedorczak, D. Galassi, Ph. Ghendrih, R. Leybros, Y. Marandet, N. Mellet, J. Morales, N. Nace, E. Serre, P. Tamain, and M. Valentinuzzi. Implementation of drift velocities and currents in soledge2d–eirene. *Nuclear Materials and Energy*, 2017. (Cited in section 4.1.1.)

[66] H. Bufferand, B. Bensiali, J. Bucalossi, G. Ciraolo, P. Genesio, Ph. Ghendrih, Y. Marandet, A. Paredes, F. Schwander, E. Serre, and P. Tamain. Near wall plasma simulation using penalization technique with the transport code soledge2d-eirene. *Journal of Nuclear Materials*, 438(Supplement):S445 – S448, 2013. Proceedings of the 20th International Conference on Plasma-Surface Interactions in Controlled Fusion Devices. (Cited in section 4.2.1.)

[67] H. Bufferand, G. Ciraolo, Y. Marandet, J. Bucalossi, Ph. Ghendrih, J. Gunn, N. Mellet, P. Tamain, R. Leybros, N. Fedorczak, F. Schwander, and E. Serre. Numerical modelling for divertor design of the west device with a focus on plasma–wall interactions. *Nuclear Fusion*, 55(5):053025, 2015. (Cited in sections 4.2.1 and 4.4.4.)

[68] H Reimerdes, G P Canal, B P Duval, B Labit, T Lunt, W A J Vijvers, S Coda, G De Temmerman, T W Morgan, F Nespoli, B Tal, and the TCV Team. Power distribution in the snowflake divertor in tcv. *Plasma Physics and Controlled Fusion*, 55(12):124027, 2013. (Cited in section 4.2.1.)

[69] M. Baelmans, P. Börner, W. Dekeyser, and D. Reiter. Tokamak plasma edge modelling including the main chamber wall. *Nuclear Fusion*, 51(8):083023, 2011. (Cited in section 4.2.1.)

[70] H.-J. Klingshirn, D.P. Coster, and X. Bonnin. Advanced spatial discretizations in the b2.5 plasma fluid code. *Journal of Nuclear Materials*, 438(Supplement):S856 – S860, 2013. Proceedings of the 20th International Conference on Plasma-Surface Interactions in Controlled Fusion Devices. (Cited in section 4.2.1.)

[71] L. Isoardi, G. Chiavassa, G. Ciraolo, P. Haldenwang, E. Serre, Ph. Ghendrih, Y. Sarazin, F. Schwander, and P. Tamain. Penalization modeling of a limiter in

the tokamak edge plasma. *Journal of Computational Physics*, 229(6):2220 – 2235, 2010. (Cited in section 4.2.1.)

[72] A. Paredes, H. Bufferand, G. Ciraolo, F. Schwander, E. Serre, P. Ghendrih, and P. Tamain. A penalization technique to model plasma facing components in a tokamak with temperature variations. *Journal of Computational Physics*, 274(Supplement C):283 – 298, 2014. (Cited in section 4.2.1.)

[73] P. Tamain, H. Bufferand, G. Ciraolo, C. Colin, D. Galassi, Ph. Ghendrih, F. Schwander, and E. Serre. The tokam3x code for edge turbulence fluid simulations of tokamak plasmas in versatile magnetic geometries. *Journal of Computational Physics*, 321:606 – 623, 2016. (Cited in section 4.3.1.)

[74] D. Galassi, P. Tamain, H. Bufferand, G. Ciraolo, Ph. Ghendrih, C. Baudoin, C. Colin, N. Fedorczak, N. Nace, and E. Serre. Drive of parallel flows by turbulence and large-scale e x b transverse transport in divertor geometry. *Nuclear Fusion*, 57(3):036029, 2017. (Cited in sections 4.3.1, 4.3.2, 4.4.4, and 4.4.4.)

[75] J.R. Harrison, G.M. Fishpool, and B.D. Dudson. Filamentary transport in the private flux region in mast. *Journal of Nuclear Materials*, 463(Supplement C):757 – 760, 2015. PLASMA-SURFACE INTERACTIONS 21. (Cited in sections 4.3.1 and 4.4.4.)

[76] B. LaBombard, J.E. Rice, A.E. Hubbard, J.W. Hughes, M. Greenwald, J. Irby, Y. Lin, B. Lipschultz, E.S. Marmar, C.S. Pitcher, N. Smick, S.M. Wolfe, S.J. Wukitch, and the Alcator Group. Transport-driven scrape-off-layer flows and the boundary conditions imposed at the magnetic separatrix in a tokamak plasma. *Nuclear Fusion*, 44(10):1047, 2004. (Cited in sections 4.3.1 and 4.4.3.)

[77] D. D. Ryutov. Geometrical properties of a "snowflake" divertor. *Physics of Plasmas*, 14(6):064502, 2007. (Cited in section 4.4.4.)

[78] P. M. Valanju, M. Kotschenreuther, S. M. Mahajan, and J. Canik. Super-x divertors and high power density fusion devices. *Physics of Plasmas*, 16(5):056110, 2009. (Cited in section 4.4.4.)